IPP-Report

Max-Planck-Institut für Plasmaphysik

Marcin Rasinski

The structural degradation of the tungsten and/or carbon fusion tokamak divertor

IPP 17/36
November, 2012

WARSAW UNIVERSITY
OF TECHNOLOGY

Faculty of Materials Science and Engineering

Ph.D. THESIS

Marcin Rasiński, M.Sc.

The structural degradation of the tungsten and/or carbon fusion tokamak divertor

Supervisor
Professor Małgorzata Lewandowska, Ph. D., D. Sc

Warsaw, 2012

I would like to express special appreciation and thanks to my supervisor Prof. Małgorzata Lewandowska for generously sharing her time and knowledge. She has given me great support throughout the period of study and her encouragement made this thesis possible.

I am most grateful to Dr Martin Balden and Dr Hans Maier from Max-Planck-Institut für Plasmaphysik in Garching for their valuable contributions and sharing their knowledge and experience. This has had significant influence on the work and has resulted in exceptionally close cooperation.

I also wish to thank all my colleagues and associates in the Faculty of Materials Science and Engineering at Warsaw University of Technology and the Max-Planck-Institut für Plasmaphysik whose support, encouragement and assistance has contributed to this thesis."

Moim rodzicom

Streszczenie

Materiały stosowane do budowy reaktora syntezy termojądrowej muszą spełnić szereg kryteriów w celu zapewnienia bezawaryjnej pracy w trakcie całego okresu eksploatacji. Ze względu na ekstremalne warunki panujące wewnątrz reaktora szczególne wymagania stawia się materiałom tzw. pierwszej ściany, w tym stasowanym do budowy divertora. Divertor odpowiedzialny jest m.in. za usuwanie cząsteczek helu oraz innych zanieczyszczeń z plazmy. Jest on narażony na działanie najwyższej temperatury pracy, największych szoków termicznych jak również erozji. Wymagania te najlepiej spełniają wolfram oraz węgiel, nie mniej jednak także one podlegają w tych warunkach procesom degradacji.

Celem pracy jest określenie zmian mikrostruktury materiałów stosowanych do budowy divertora w symulowanych i rzeczywistych warunkach pracy reaktora syntezy termojądrowej.

W pracy badano degradację, pod wpływem wysokiej temperatury systemu powłok Mo/W nakładanych na podłoże węglowe. Elementy tego typu stosowane są obecnie do budowy divertora w reaktorze JET. W celu określenia procesów zachodzących na granicach międzyfazowych podłoże/Mo/W i ich kinetyki, systemy powłok, identyczne z instalowanymi w reaktorze, poddano obróbce cieplnej w różnych temperaturach oraz w różnym czasie. Obrazowanie przy użyciu mikroskopii elektronowej (skaningowej oraz transmisyjnej) w połączeniu z technikami dyfrakcyjnymi pozwoliły na zidentyfikowanie typu powstających węglików (m.in. analizę fazową) oraz ustalenie kinetyki degradacji tych warstw. Otrzymane wyniki pozwoliły na oszacowanie maksymalnej temperatury pracy reaktora.

W drugim wątku pracy badano powstawanie warstw depozytów w reaktorze syntezy termojądrowej w wyniku procesów erozji i osadzania materiałów, z których zbudowany jest divertor. Stwierdzono, że powstające warstwy składające się głównie z węgla i wolframu są niejednorodne na swojej grubości, co sugeruje różne warunki ich powstawania. W celu ustalenia tych warunków wytworzono cieknie warstwy amorficznego węgla domieszkowanego różną ilością wolframu, które następnie wygrzewano w różnych warunkach. W warstwach modelowych zaobserwowano, przy użyciu technik wysokorozdzielczej mikroskopii elektronowej oraz nano-dyfrakcji, powstawanie różnego typu węglików wolframu (WC, W_2C, WC_{1-x}) w proporcjach zależnych zarówno od temperatury wygrzewania jak i ilości domieszkowanego wolframu. Porównanie wyników

laboratoryjnych z realnymi depozytami pozwoliło zidentyfikować lokalne warunki tworzenia depozytu w reaktorze.

Abstract

The materials and components used in fusion reactors must comply with the specific criteria required to guarantee safe and reliable operation throughout the whole working life of the equipment. The extreme working environment inside a fusion reactor requires that the materials and components used for the first wall, which are in direct contact with plasma, must be resistant to high temperature, thermal shock as well as possess low chemical and physical erosion yields. The most heavily loaded part of a fusion device is the divertor, which is responsible for the removal of helium and other impurities together with the dissipation of power.

The main objective of the work was to determine the microstructural changes occurring in the materials employed in the divertor first wall when subjected to real and simulated working condition encountered in a fusion reactor.

In this work, the degradation of the Mo/W coatings on carbon substrate when subjected to high temperatures were studied. These coatings are currently being used for divertor plates in the JET reactor in Culham UK. The high temperature occurring in the divertor region can be expected to induce diffusion of carbon from the substrate to the coatings which would lead to the formation of brittle carbides. A set of samples identical to those installed in the JET reactor were subjected to heat treatment for different periods and temperatures to determine the degree of carbon diffusion and the conditions for carbide formation. Scanning and transmission electron microscopy together with electron diffraction enabled identification of the formed carbides and the level of degradation of the coatings to be established. The results are helpful in determining, based on the JET operating conditions, the safe working lifetime of the element.

The second major problem investigated was the analysis of the material deposits originating from the erosion of the first wall material during the operation of a fusion tokamak. The analysis revealed that the deposited layers consisting of carbon and tungsten possessed a non homogeneous cross-section which suggests that varying conditions occurred during the growth of the layers. To determine the creation conditions a set of thin amorphous carbon films, doped with different concentrations of tungsten (a:C-W), were produced and subjected to annealing at different temperatures. In these layers, which acted as model systems for forming the deposits, different forms of tungsten carbide crystallites (WC, W_2C, WC_{1-x}) of various sizes were observed by means of high resolution electron microscopy and nano-diffraction. The sizes and phase composition diversity were a function of the creation

conditions – tungsten concentration and annealing temperature. The comparison between the model a:C-W film and the re-deposited layers enabled to identify the local conditions during their formation in the fusion reactor.

Contents

1 Introduction

According to the Executive Summary of the 2010 World Energy Outlook published by the International Energy Agency (IAE), the world's primary energy demand will increase from the 2008 level of 12 300 million tones of oil equivalent (Mtoe) to over 16 700 Mtoe in 2035. This implies an average steady growth of 1.2% per year [1]. However, in different Policies Scenarios, the growth was estimated at various annual rates between 0.7% to over 1.4%. Energy production is still based mainly on the non-renewable resources (coal, oil and natural gas and its contribution to total energy production has decreased only very slightly - from 86.6% in 1973 to 80.1% in 2009 [2]. The limited and ever shrinking world reserves of fossil and the increasing concern about the cleanliness of the systems of energy supply demands the development of new sustainable power sources. One of the interesting options is fusion energy as it offers almost unlimited availability, provides technological safety and relative cleanliness.

Nuclear fusion is, in simple terms, a process in which two or more atomic nuclei unite to form a heavier nucleus which is accompanied with a huge release of energy. The most efficient fusion reaction with greatest probability of its occurrence at relatively moderate temperatures is the reaction between two hydrogen isotopes – deuterium (D) and tritium (T), as given by equation 1.1.

$$D + T \longrightarrow {}^{4}He\ (3.5MeV) + n\ (14.1MeV) \tag{1.1}$$

This reaction can occur on Earth only under specific conditions, the most vital requirements being a temperature of at least 100 million K. At such temperatures, the electrons are separated from the nuclei and gaseous hydrogen becomes a plasma. Since the plasma is electrically charged, it can be confined in an electromagnetic field. The earliest attempts to control a magnetically confined plasma started in the 1950's and since then the knowledge and experience of heating and controlling plasma for possible fusion application has been constantly increasing. Several experimental fusion devices of different type and scale have been built in recent years [3-8]. These devices have enabled further understanding of the underlying physics and material-related issues, which are of prime importance for a working reactor, to be obtained. The latest step on the road to the development of a commercial fusion power plant is the International Thermonuclear Experimental Reactor

(ITER) project. The project was launched in 2006 and the main scientific goal is to reduce ten times the power it consumes [9] – and is assumed to be the first of the various fusion experiments to produce a net gain of energy.

Although the hot plasma is isolated from the material used for the inner wall by the magnetic field, the working environment for the structural components of reactor are still extremely demanding. It follows that one of the most critical issues for any fusion device is the availability of materials able to meet the extreme environmental conditions and operate for the designed life whilst ensuring complete safety. The most exposed part of a fusion device, which has to endure the highest power and resist the impact of particles is the divertor located at the bottom of the reactor. The role of the divertor is to extract heat and helium ash, which are products of the fusion reaction, as well as other impurities from the plasma. The divertor is also expected to provide neutron shielding for the nearby parts of the toroidal vacuum vessel and the coils of the superconducting magnets. The divertor system is required to withstand intense static and dynamic forces such as thermal loads, structural loads and electro-magnetic loads. At present, these criteria are best fulfilled by employing tungsten and carbon base materials, which are currently used in the majority of devices, however they do suffer from structural degradation in the operational condition.

In order to assure long term and safe operation of the future reactor components, in particular divertor, the occurring degradation processes need to be modelled in laboratory experiments and confirmed in the working conditions of the actually operated fusion devices. In the present work, such an investigation has been done taking into account various material systems, as the optimum one is not defined as of yet. The main purpose is to provide useful data regarding mechanism and kinetics of structural degradation as well as operational life and strategies to prevent rapid degradation in the severe working environment. Advanced electron microscopy techniques are expected to be a vital tool for investigations in this field.

2 Divertor and materials concepts for divertor

A nuclear fusion reactor consists of two main components which directly face the plasma – the so called first wall and the divertor, referred to as the limiter in previous systems. The first wall is the surface surrounding the bulk region of the plasma. The plasma shape has to be restrained to protect the vessel wall and more fragile components which cannot withstand excessive heat loads. The border of the confined plasma region is called the Last Closed Flux Surface (LCFS) or separatrix, creating the boundary between open and closed field lines in

the plasma. That border separates the confined plasma region from the region where field lines come into contact with the material surfaces. A narrow region, usually only a few centimetres wide, outside that border is known as the Scrape-Off Layer (SOL) where the plasma is effectively scraped off from the core plasma. The magnetic lines are open there and the plasma exhaust is directed into a defined region where the exhaust particles collide with the wall [10] (Figure 2.1).

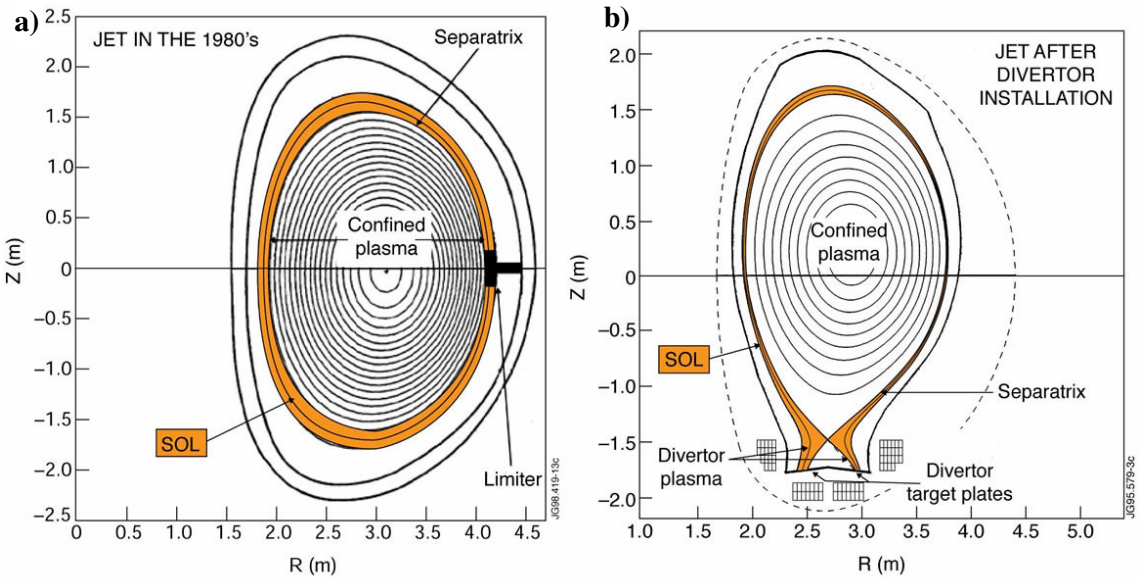

Figure 2.1. Schematic of the confined plasma configuration with the (a) the limiter and (b) the divertor - based on the JET tokamak [11]

From the historical point of view, there are two methods for delimiting the last closed field lines. The simpler choice was to insert a physical barrier penetrating a few centimetres into the plasma, thereby "limiting" the confined plasma region (Figure 2.1a). This concept to install a limiter, was successful to some extent, however, it had a major disadvantages. The material released by the plasma impacting on the limiter could penetrate right into the plasma core and so degrade the properties of the plasma. In addition, the concept does not allow to the fusion ash to be adequately pumped away.

To solve the problems arising from the drawbacks to the limiter, a more sophisticated concept for a divertor was implemented about 20 years ago. The magnetic field lines were modified at the edge of the plasma so that the field lines of the SOL are diverted to a dedicated region. (Figure 2.1b). The region where the plasma exhaust ends in a collision is called the divertor. The distance between colliding region on the divertor and the confined plasma is much greater than exists with the limiter configuration. It is much simpler to

maintain a low level of impurities in the plasma core since the probability of penetration of material eroded from the divertor is significantly lower. Whereas a limiter is a material object used to physically limit the shape of the plasma, the divertor is rather a device to modify the form of the magnetic field. The path of the exhaust particles from the point at which they enter the SOL plasma to the divertor targets can be sufficiently large for the plasma to undergo significant cooling. When the plasma cools down, the plasma electrons and ions recombine to form neutral atoms before colliding with the solid surfaces. These neutral particles create a "cloud" of gas in the divertor region, which can be efficiently pumped away.

The construction of a divertor will be different for the various fusion devices and will be dependent on the particular plasma configuration. All divertor concepts, however, consist of two main parts – the plasma-facing components (PFCs) and the divertor cassette body. The PFCs are responsible for heat extraction from the plasma and the cassette body acts as the support for the PFCs. PFCs normally consist of a dome together with inner and outer vertical targets, as illustrated in Figure 2.2b at the cross section of the ITERs divertor. The lower parts of the vertical targets interact directly with the SOL plasma. This area is therefore most exposed to high power and heat loads. The upper part of each vertical target act as a baffle for the neutrals. The dome, placed below the separatrix, has no connection to the main plasma and therefore is subjected mainly to radiation and charge exchange neutrals. The dome, additionally, baffles neutral particles preventing them from reaching and penetrating the main plasma across the separatrix and thereby prevent an increase in the impurity level in the main plasma.

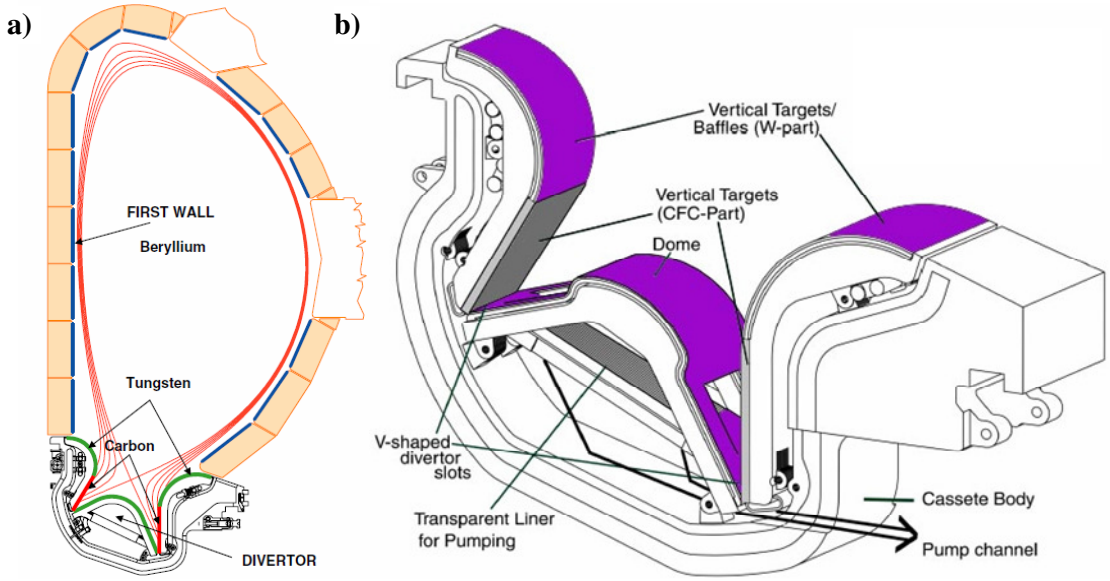

Figure 2.2. (a) ITER cross-section ([12] (b) the divertor scheme [13]

Precise position along the divertor is given by the s-coordinate which is a poloidal coordinate defined along the divertor surface. The s-coordinate value is given by the distance from the innermost point on the divertor through all divertor up to outermost point.

When selecting the **material for plasma-facing components** for the divertor, the safe working life of the components is one of the most critical issues. The divertor PFCs lifetime is dependent primarily on its working conditions and the selected materials resistance to operational environment. The erosion by ions and neutrals escaping from the plasma together with high heat loads and other negative effects cause degradation of the divertor PFCs. Details are given in Section 4. Because of the extremely aggressive working environment, the materials selected for the divertor PFCs is restricted to tungsten and carbon [14]. Each of these materials has inherent advantages and disadvantages and their application depends on the specific operation requirements.

Carbon, especially in the form of carbon fibre reinforced carbon composites (CFC), is a good candidate material for current application as divertor PFCs because of its beneficial thermo-physical properties, particularly excellent thermal shock resistance [15]. Carbon as a low-Z material also possesses parameters to give good plasma performance, as it can be fully ionized and, therefore, will not cause significant pollution of the plasma. These are the main reasons for the use of carbon base materials in most fusion devices throughout recent decades. An additional advantage of carbon is that it will undergo sublimation rather than melting during the even more extreme working conditions that may arise from the disruption of normal operation. Despite possessing these advantages, carbon exhibits specific drawback, especially if it is being considered for use in future reactor devices. Its main disadvantage is that it suffers a high rate of erosion even at the lower temperatures and bombardment by low energy ions [16]. This has a limitation on the lifetime of carbon PFCs. Additionally, carbon erosion is related to the subsequent accumulation of hydrogen (tritium) in the vessel by its re-deposition in the form of hydrocarbon films [17]. The hydrocarbon re-deposits become mechanically unstable and are likely to produce hazardous dust. Moreover carbon undergo its properties degradation due to neutron irradiation [18]. Unfortunately, these negative aspects related to the behaviour of carbon are serious disadvantages to it being seriously considered as a material for use as a divertor PFCs in future fusion reactors.

Tungsten is considered as a promising alternative material to carbon because of its high sputtering threshold under hydrogen bombardment, its good thermal conductivity, high temperature strength and high melting point [19]. In addition, tungsten offers the advantage of

good resistance to erosion compared with the low-Z materials, like carbon. Moreover, tritium accumulation in tungsten by re-deposition is not expected to be a problem. However, its high atomic number means that its maximum tolerable concentration of sputtered tungsten in the plasma is much smaller than that of the light elements. The potential effect of significant plasma poisoning and, as a consequence, plasma cooling is considerably greater. It follows that the allowable level of tungsten permitted within the plasma is significantly lower, than is permitted for low-Z materials. An addition disadvantage of tungsten is its brittle behaviour at low operating temperatures which leads to surface cracking [20]. However, despite the disadvantages, tungsten is currently considered to be a promising material for divertor PFC applications.

As presented, both candidate materials – carbon and tungsten – have disadvantages, but they are to date the best possible material for use as divertor PFCs. Currently, they are both being used in different combinations in different tokamak facilities. In the initial stage of ITER operation, according to present assumptions, CFC are foreseen for the vertical targets and bulk tungsten tiles for the remaining divertor PFCs. The CFC parts are predicted to be the armour for the region of highest heat flux where the scrape-off layer of the plasma interacts with the vertical targets. Thanks to relatively long experience with carbon PFCs e.g. in JT-60U (Ibaraki Prefecture, Japan) [21] or Tore Supra (Cadarache, France) [22], the CFC production technology is currently quite well developed. The main issue, however, is the CFC connection to the heat sink component. High-quality bonding of the armour to the heat sink is essential to ensure an adequate lifetime of the components as most failures of this component, particularly cracking or delamination are associated with the bonding [23].

In the second period of ITER operation, in the tritium usage phase, divertor plasma-facing components are expected to be made entirely of tungsten [24]. All major design studies of future fusion research and reactor devices also currently relying only on tungsten for the plasma-facing component in the divertor region. Tungsten in the bulk form will be used as the ITERs divertor, but so far only a transient solution is studied. In current tokamaks, tungsten is used in the form of a coating on a graphite or CFC substrate.

Considerable experience in selection and subsequent testing **tungsten coatings** gained in the ASDEX Upgrade (Axially Symmetric Divertor EXperiment) tokamak, which was commissioned at the Max-Planck-Institut für Plasmaphysik, Garching in 1991. In the programme launched in 1999, the ASEDX Upgrade was steadily converted from a complete carbon device to one with a full tungsten coverage by 2007 [25][26]. Two types of tungsten coating were selected to progressive installation - PVD (physical vapour deposition) with a

thickness up to 10 μm and 200 μm VPS (vacuum plasma spraying) coatings on graphite and CFC tiles. The thickness and coating technique was selected based on the divertor's working environment in the different position on the PFCs [27]. A 4 μm thick PVD coating, because of its high-power load capability, was deposited on most of the divertor. Only the outer divertor region, where the highest erosion rates occurs, exceeding 1 μm per campaign (one operation period), the 200 μm thick VPS coating on the CFC substrate were employed. The thin PVD coatings withstood power loads of more than 15 MW/m^2 up to melting and exhibited very good adhesion to the surface [28]. The same PVD coatings were also used for CFC substrates. However, due to the inhomogeneous CFC surface characteristics and different coefficients of thermal expansion resulting from the CFCs fibre orientation, the reliability of this coating was worse than the coatings on graphite substrate. The thick VPS coatings showed different levels of damage during the in-vessel inspection. Surface layer melting with droplets was observed together with a significant number of cracks which penetrated through the coating. Significant delamination of the tungsten flakes from the coating causing limitations of the plasma operation was evident [29][30].

Further stages in the development of tungsten coatings, especially related to those on the CFC substrate, were made during the ITER-like Wall Project [31] launched at the JET (Joint European Torus) tokamak. JET, situated near Culham in the UK, is currently the world's largest magnetic confinement plasma physics experiment in operation. One of the main purposes of the ITER-like Wall Project is to test the materials combination foreseen for installation in ITER using the most ITER-relevant parameters accessible today. In the current ITER-like wall project, tungsten lamellae stacks are installed in the load-bearing septum replacement plate, the dome region, and tungsten coatings are applied to CFC substrates in the other areas of the divertor [32].

Because of the known problems of anisotropic coefficients of thermal expansion between CFC and tungsten which causes cracking, delamination and partial losses of the coating, an extensive R&D program has been launched in 2005 to develop the optimum type of coating for the Project [33]. Ten different PVD and CVD coating with 4 μm and 10 μm thicknesses together with four 200 μm VPS coating types were selected for testing. The investigation included establishing the characteristics of coating adhesion, impurity levels in the coating and internal stresses, together with high heat flux tests. Power load tests included power increases from 4 MW/m^2 in 6 s up to 22MW/m^2 in 1.5 s. Nine of fourteen coatings which survived the test were subsequently subjected to a cycling high heat flux pulsing test. The best

results were obtained for the 200 μm VPS coating and a thin 10 μm ion assisted magnetron sputtered coating [34]. Because of problems involved in up-scaling the VPS coatings technology from small samples to real tiles, the so called CMSII (combined magnetron sputtering and ion implantation) technique has been approved. The application of 10-15 μm tungsten coating with an additional 2-4 μm molybdenum interlayer produced by CMSII technology has been selected for the JET divertor [35]. The enhanced performance of this type of coating is related mainly to stress relief induced into the coating by the high energy ion bombardment and the molybdenum interlayer between the tungsten and CFC substrate, which reduces the mismatch of the coefficients of thermal expansion.

The continuing problem is carbide formation at the coating-substrate boundary caused by carbon diffusion as there is no active barrier to prevent it. This aspect was not important in the case of the ASDEX Upgrade, but is likely to be a concern in the JET tokamak due to the higher operation temperatures. The first results of the high heat flux test with a power density of 16.5 MW/m^{2,} performed on pre-carbidised samples, have had a strong influence on coating quality. The creation of a brittle tungsten carbide layer has caused significant delamination, as illustrated in Figure 2.3 [36] [37]. Sample with highest tungsten carbide layer has lost 25% of the of the coating during the high heat flux test.

Table 2.1 Observed delaminated surface area fractions for the respective dwell times after vacuum heat treatment at 1620 K

Dwell time	2 h	5 h	20 h
Delaminated fraction	0.02%	Up to 5%	Up to 25%

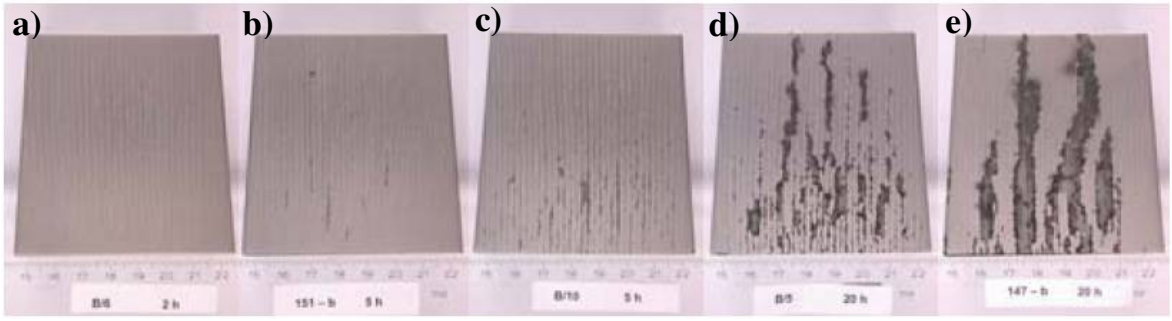

Figure 2.3 The coatings delamination of pre-carbidised samples after 2 h (a), 5 h (b. c) and 20 (d, e) annealing at 1670 K subjected to high heat flux test [37]

The kinetics of carbide formation in the CMSII coating is therefore a very important consideration when determining the working lifetime of the divertor PFCs. This was a starting point for designing research programme carried out within this thesis, in which tungsten

coated CFC samples were annealed at various conditions in order to determine the mechanism and kinetics of its structural degradation.

3 Tungsten carbides

Since the divertor target is made mostly of carbon, tungsten, or a mixture of both, the formation of tungsten carbide can be anticipated principally because of the very high temperature in the vicinity of the divertor. Tungsten carbides belongs to the group of interstitial carbides, also referred to as the refractory metal-carbides, and are characterized by extremely high melting points, high hardness, excellent thermal and electrochemical stability, but they are extremely brittle [38]. The transition metal carbides often have simple crystal structures, face-centered cubic (fcc), body-centered cubic (bcc), or hexagonal (hcp), with the carbon atoms located in the interstitial spaces between metal atoms.

The W-C system includes two carbide phases – **monocarbide** (WC) and **subcarbide** (W_2C), each of which has several polymorphs, being stable in certain temperature ranges and carbon concentration ranges (Figure 3.1).

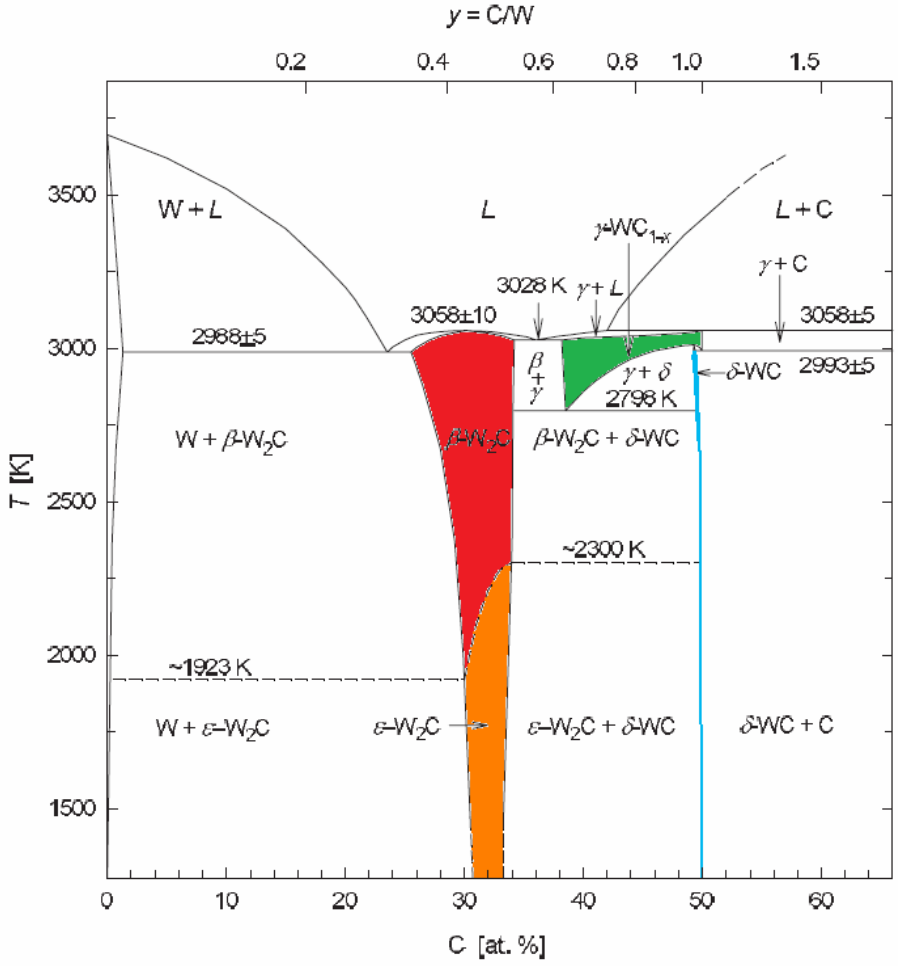

Figure 3.1. Phase diagram of the W-C system [43]

The WC monocarbide has two structural modifications – a low temperature hexagonal structure, denoted as δ-WC or simply **WC** (space group $P\bar{6}m2 = D_{3h}^{1}$) and a metastable, high-temperature cubic form, designated as α-WC, γ-WC_{1-x} or simply **WC_{1-x}** (space group $Fm\bar{3}m = O_h^5$). The stoichiometric monocarbide WC is the only thermodynamically stable phase and can exist from temperatures below room temperature up to 3049 K. Over the hole temperature range the WC carbide does not have a homogeneity range, which means that the WC phase only exists at a precise carbon concentration equal to 50 at. % [39]. The WC carbide has a hexagonal structure with lattice parameters $a = 2.906$ Å and $c = 2.837$ Å with an *Ab Ab* stacking sequence with layers entirely of tungsten atoms (*A*) and layers entirely of carbon atoms (*b*) alternately interspaced (Figure 3.2). The carbon atoms are located in the centre position of the trigonal-prismatic interstices in the tungsten sublattice. The cubic WC_{1-x} carbide is stable at temperatures above 2790-2810 K. The highest homogeneity range 37 – 50

at. % of carbon at temperatures 3030-3055 K is dropping with temperature. The WC_{1-x} carbide is face-centered cubic with an *AcBaCb AcBaCb* stacking structure for which the lattice parameter increases with carbon content from $a = 4.22$ *Å* reaching $a = 4.26$ *Å* for the maximum carbon concentration of $WC_{1.0}$ [40].

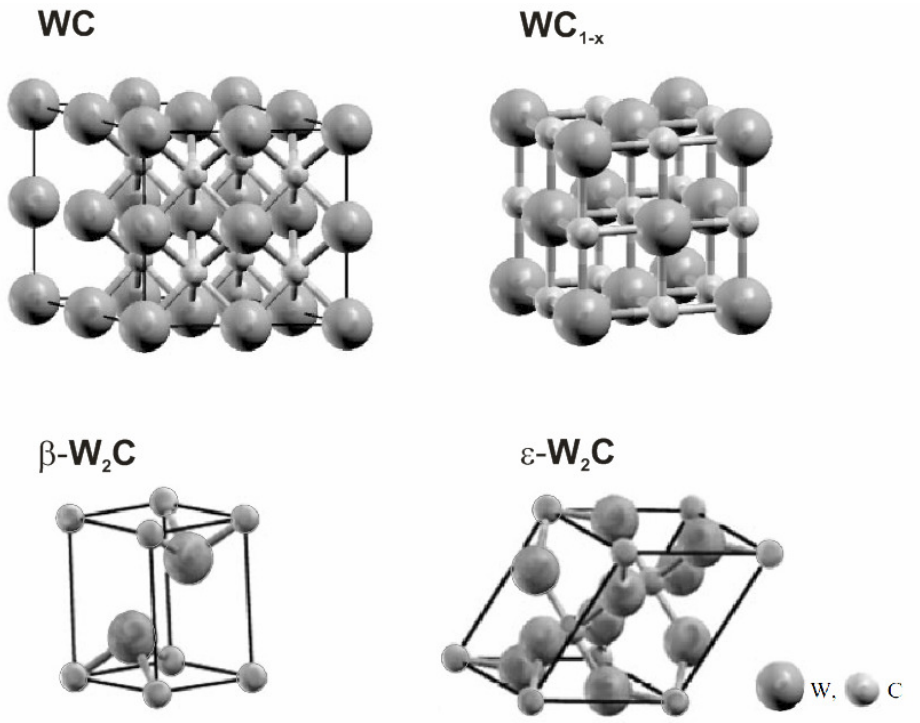

Figure 3.2. Crystal structures of WC,WC_{1-x}, β-W_2C and ε-W_2C carbides [44]

The tungsten subcarbide (**W_2C**) according to [41] exists in four allotropic forms – a high-temperature close-packed hexagonal β-W_2C phase (space group $P6_3/mmc = D_{6h}^4$) and three low temperature forms: orthorhombic β'-W_2C (space group Pbcn = D_{2h}^{14}), ordered rhombohedra β''-W_2C (space group $P\bar{3}m1 = D_{3d}^3$) and trigonal ε-W_2C (space group $P\bar{3}1m = D_{3d}^1$). The high temperature, disordered β-W_2C phase with lattice parameters $a = 2.996$ *Å* and $c = 4.724$ *Å* is stable at temperatures between 2750 and 3050 K with carbon concentration in the range 25-34 at. %, which reduces with decreasing temperature. New data from neutron diffraction studies by Kurlov and Gusev [42] has revealed of the three low-temperature W_2C carbide phases (β'-W_2C, β''-W_2C and ε-W_2C) the only stable ordered phase it the trigonal ε-W_2C form. The ε-W_2C phase is formed, most likely, by a second-order phase transition at temperatures between 1923-2300 K. The lattice parameters of ε-W_2C phase are – $a = 5.253$ *Å* and $c = 4.772$ *Å*.

The structure of each tungsten subcarbide, W_2C, consist of a hexagonal close package tungsten sublattice in which 35%-50% of carbon atoms occupy octahedral interstices, while other interstices are vacant. In the case of the β-W_2C phase the distribution of carbon atoms and vacancies is random, whereas in the case of ε-W_2C phase there is some degree of ordering. There are alternating planes of a non-metallic sublattice in which each vacancy is surrounded by six carbon atoms or each carbon atom is surrounded by six vacancies.

The non-stoichiometric cubic WC_{1-x} is stable above 2790K and both W_2C phases are stable above 1370 K. At room temperature, both phase are thermodynamically unstable, but may be present by virtue of concentration-driven and temperature-driven nonequilibrium transformations [45]. The presence of W_2C and WC_{1-x} phases was attributed to decarburization of WC at high temperatures [46][47]. However, Demetrious et al. [48] demonstrated that under non-equilibrium conditions local metastability is the limiting factor of the microstructural evolution.

The working conditions of a fusion tokamak divertor are such that there are two possible causes for the formation of tungsten carbide. The first results from the diffusion of carbon from graphite or a CFC substrate into tungsten coating induced by the high temperature and the second is carbide creation in the re-deposited layers caused by erosion and mixing mechanisms.

In the initial phase of carbon diffusion W_2C carbide appears at the boundary of the coating and substrate. This may be explained by the lower equilibrium carbon concentration required, 3 wt. %, than the 6.13 wt. % required for the formation of WC. However, different experimental groups give different temperatures for the formation of the W_2C phase. Luthin and Linsmeier [49] together with Hildebrandt et al. [50] report that W_2C carbide formation commencing starting from 770 K , whereas Yeh et al. [51] and Leroy et al. [52] show the W_2C type carbide forming at higher temperatures, up to 1200-1240 K.

The reported differences in temperatures may be attributed to the different investigation technique employed. XPS (X-ray photoelectron spectroscopy) as used by Luthin and Hildebrandt is a very surface sensitive technique of for the analysis of the chemical state in which even a very small amount of created carbide can be detected. However, XRD (X-ray Diffraction) used by Yeh and Leroy requires a larger volume of the phase (both volume fraction and size of the phase) before it can be detected. It is possible that the less sensitive technique employed by Yeh and Leroy could be the reason why they reported a higher temperature for the formation of W_2C.

At higher annealing temperatures, the metal-rich carbide W_2C phase starts to transform into the hexagonal monocarbide WC. Different temperatures at which first WC starts to appear have been reported and these vary between 970 K [49], below 1170 K [51] or in the range 1320-1370 K [52]. However, in all cases during annealing at above the reported temperatures both phases (W_2C and WC) coexist. Prolonged heat treatment above these temperatures changes the W_2C to WC ratio – the amount of W_2C decreases as the WC is increases. This is easily explained as the W_2C phase is metastable and the bonding enthalpy ΔG^f of WC is lower than W_2C [53]. With increased carbon diffusion the WC phase becomes predominant. The W_2C/WC ratio is reduces more rapidly the higher the temperature of isothermal treatment e.g. at the temperature 1223 K the ratio W_2C/WC drops below 1 after 8 h of isothermal holding, whereas at temperature 1323 K, the ratio drops below 1 in less than 2 h [53]. It has been also confirmed that the formation of W_2C is controlled by carbon diffusion through the W_2C phase, but the data reported about the activation energy of carbon diffusion in W_2C varies from 167 to 469 kJ/mol (1.73 to 4.86 eV) [54]. The data spread shows the necessity to undertake individual experiments to obtain a precise assessment of carbide creation in selected tungsten coating on CFC substrates for divertor PFCs.

The second situation leading to carbide formation in the divertor working conditions is related to erosion of material, its mixing and re-deposition which can be reasonably simplified as the simultaneous deposition of tungsten and carbon. There are various deposition processes, of which reactive magnetron sputtering is the most popular. Magnetron sputtering can be undertaken using tungsten [55] or tungsten carbide [56] targets. The supply of carbon can be achieved by graphite target sputtering [55] or in a gaseous form, for example by using benzene [57], acetylene [58] or methane [59] vapour. In all cases, however, the most important factor determining the film structure is the tungsten to carbon ratio in the film or simply the tungsten amount addition, mostly determinate in W at. %.

Abad et al. [56] have studied the phase composition in magnetron deposited carbon films with a concentration of tungsten range of 27 to 63 at. %. In all investigated samples, the presence of a mixture of hexagonal W_2C and cubic WC_{1-x} carbide was identified by means of XRD - Figure 3.3a.

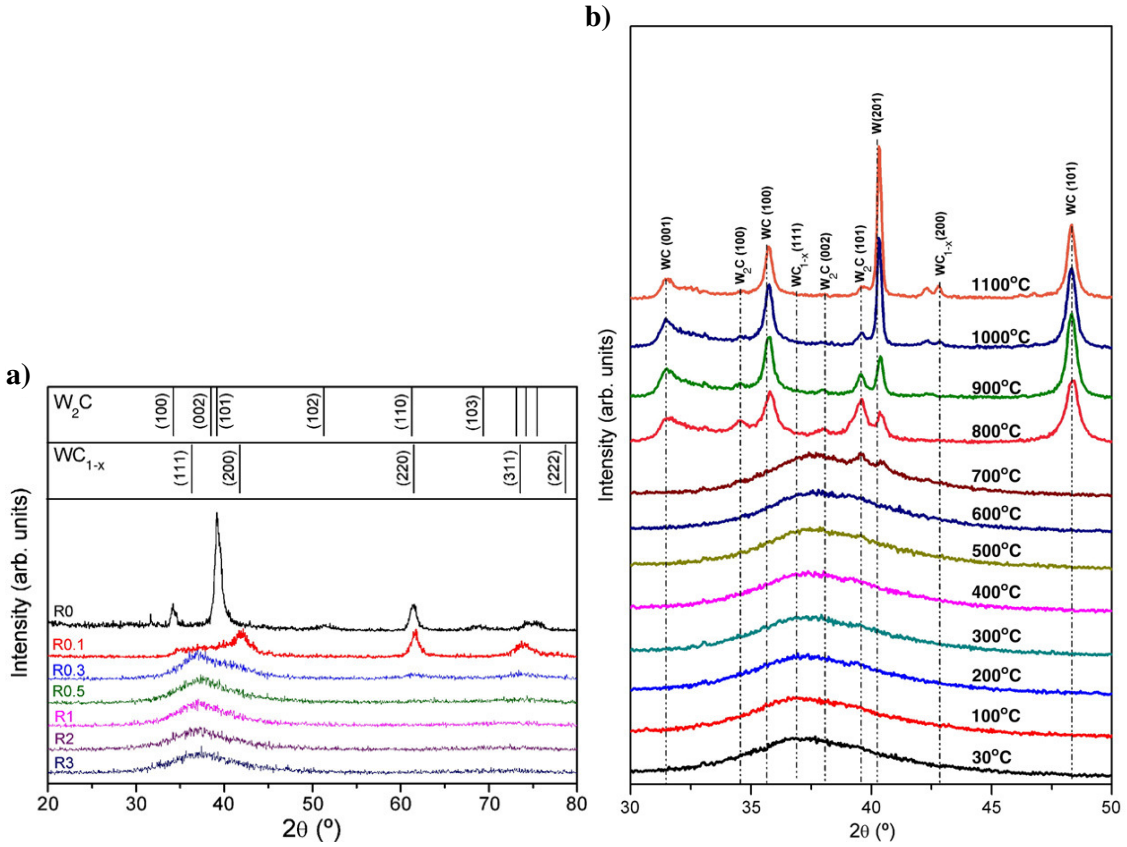

Figure 3.3. XRD spectra of as-deposited WC/a-C films as a function of tungsten concentration: (a) R0–63 at. %, R0.1–58 at. %, R0.3–47 at. %, R0.5–40 at. %, R1 – 32 at. %, R2 – 28 at. %, R3 –27at. % (b) high temperature XRD data of 32 at. % tungsten film. The lines and symbols indicate the positions of the diffraction peaks for WC_{1-x} and W_2C patterns [56]

The XRD results, especially when considering samples with a tungsten concentration below 58 at. % are quite unclear because of the broadening of the diffraction peaks caused by a nanocrystalline or even an amorphous structure. No trace of WC carbide was being reported, despite using a WC target.

From the Scherrer's formula, based on the diffraction peaks, the estimation of the crystallite size was undertaken. Crystallites with an average size of 9 nm were detected in the film with the highest tungsten concentration. In the sample with 58 at. % of tungsten, the crystallite sizes were determined for each phase. The average crystallite size of W_2C was estimated as 7 nm whereas that of WC_{1-x} was 5 nm. In the sample containing 47 at. % tungsten, the broad peak around 37° was attributed as a representation of crystallites of 2-3 nm in size. All remaining XRD results for lower concentrations of tungsten did not indicate an measurable crystallinity.

Heat treatment at up to 1070 K of the sample with 32 at. % of tungsten (Figure 3.3b) [56] revealed almost no change in the sample structure. With annealing above 1070 K authors claim to have observed the WC_{1-x} phase transformation into WC and W_2C carbides. That statement, however, is quite difficult to verify as the XRD results give no opportunity to qualitatively determine the real phase composition of a film annealed below 1070 K. The broad diffraction peak can easily be caused by a mixture of all phases with different ratios between them. The determination which phase (if any) is being transformed into W_2C and WC is equivocal. There is also the possibility that both phases,W_2C and WC, were deposited and existed in the film, but in amorphous form, or in a crystalline form but of a size not possible to be clearly determined by means of XRD. The situation above 1070 K is much clearer – after annealing in the temperature range form 1070 K to 1270 K there is definite evidence of the WC phase with some traces of W_2C. At temperatures above 1270 K, the W_2C carbide decomposes as confirmed by the intensity of the W_2C peak decreasing and the metallic tungsten peak increasing.

El Mrabet et al. [60] carried out experiments on the thermal stability of carbon films with samples containing 63 at. %, 58 at. % and 40 at. % of tungsten and reported the initial presence of WC_{1-x}. Annealing at temperatures above 870-970 K resulted in the transformation of the WC_{1-x} phase into W_2C and WC. Higher annealing temperatures led to a carbide decomposition which was confirmed by the presence of metallic tungsten. However, the initial phase composition, especially with a tungsten concentration below 50 at. % is again questionable due to broadening of the XRD diffraction peaks.

When using samples with much lower tungsten concentration, the XRD and selected area electron diffraction (SED) gave even less clear results. Samples containing 1.9 at. %, 2.8 at. %, 3.6 at. %, 6.0 at. % and 8.6 at. % deposited by combined magnetron sputtering under a benzene atmosphere were analysed by Wand et at. [61]. The authors claimed to observe tungsten atoms dissolved in an amorphous carbon matrix at a tungsten concentration below 2.8 at. %. Above 2.8 at. % tungsten concentration, it was reported that tungsten atoms began to form an amorphous WC_{1-x} phase which at higher tungsten concentration start to evolve into nanocrystalline W_2C carbide. However, the included electron diffraction patterns together with XRD spectra did not support the statement. Other similar misleading information can be found elsewhere [57][62][63].

The EXAFS and XANES results presented by Adelhelm et al. [64] show no significant carbide clustering in samples with 6.5 and 9.5 at. % of tungsten in, either the deposited state,

or, after annealing at up to 900 K. The XRD data however shows a broad diffraction peak, previously attributed to nanocrystalline carbides.

In general, it can be concluded that with lower tungsten concentrations in deposited films the crystallite size decreases down to the nanometer range or is in an amorphous state. Additionally, a commonly used characterisation technique such as XRD does not provide sufficient unequivocal information about the real phase composition especially in the as-deposited state, or after low temperature annealing, where the crystallites size is around few nanometers. Summarizing, it should be noted that erosion and re-deposition taking place in a fusion reactor may lead to the formation of complex structures, of nanometric sized tungsten carbides. It is thus necessary to model the processes occurring in a fusion reactor at a laboratory scale using model samples with deposited tungsten doped carbon films. By establishing the nature of the phase compositions in annealed laboratory deposited films a better understanding of the processes occurring in the re-deposited layers in the divertor is likely to be achieved.

4 Structural degradation of divertor components

Plasma facing components used for divertor elements need to fulfil several requirements to guarantee the safe and reliable operation for an acceptable period of operation. There are a number of operational aspects which can limit the life-time of divertors PFCs as they cause structural degradation of the divertor elements. The most important are described in this section.

4.1 Erosion

The major factor limiting the lifetime of divertor PFCs is erosion of the materials. The erosion in general can be divided into three categories:

- sputtering (physical erosion)
- chemical erosion
- melting or sublimation

Physical erosion, or sputtering, is simply the ejection of the atoms on the surface due to its bombardment by the incident energetic plasma ions or particles. The energy of the incoming plasma ion is elastically transferred to the target atoms via collisions. The incident ions themselves can be, either reflected or trapped depending on the collision conditions, for example the incident energy or the ion trajectory, etc. The energy transferred from the

incident ion or particle to the surface atom needs to be greater than a particular energy threshold (E_{th}) for it to cause sputtering. The required energy threshold is directly proportional to the mass ratio between the impacting ions and the target atoms. The higher the mass of the impacting ion and the lower the mass of surface atoms the lower is the energy required for sputtering to occur – e.g. the sputtering of carbon by deuterium ions requires E_{th} of 35eV whereas the sputtering of tungsten by deuterium and helium atoms requires E_{th} of 220eV and 110eV, respectively (D→C E_{th} = 35eV, D→W E_{th} = 220eV, He→W E_{th} = 110eV) [65].

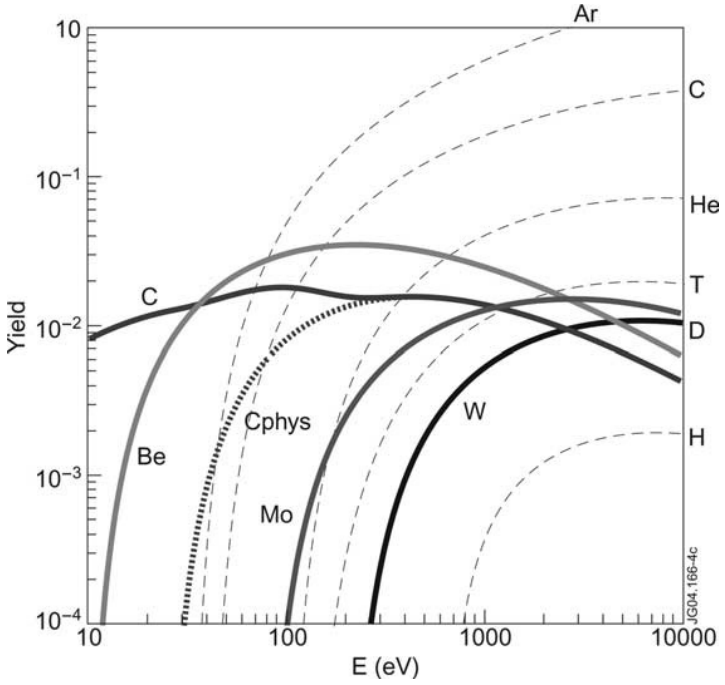

Figure 4.1. Sputtering curves for various materials bombarded by deuterium ions (solid lines). Dashed lines represents tungsten physical sputtering for a range of incident ions [65]

The average number of sputtered particles per incident ion is called the sputtering yield, Y_{phys}. Figure 4.1 illustrates the sputtering yield of several fusion related materials carbon, beryllium, molybdenum and tungsten by deuterium ions - solid lines. It should be noted that with an increase in the impact energy, the sputtering yield is increased, reaching different maximum values depending on the mass of the substrate atom - the lower the mass the greater is the sputtering yield.

The sputtering of carbon sputtered by deuterium is somewhat different in comparison to the situation with other substrate atoms. The carbon sputtering yield represented by the solid line in Figure 4.1 is actually a sum of two separate erosion mechanisms – physical sputtering and chemical erosion. The theoretical physical sputtering curve of carbon is represented by the dashed line. It can be seen that chemical erosion (at room temperature) is

the predominant mechanism at a low level of ion energy, whereas at higher levels of ion energy physical sputtering becomes the main sputtering mechanism.

Additionally, the sputtering of tungsten cause by bombardment with ions: argon, carbon, helium, tritium, deuterium and hydrogen is presented by dashed lines. The tungsten sputtering yield increases with an increase mass of incident ion. Physical sputtering is in general independent of temperature.

The second erosion mechanism, enhancing the physical sputtering yield, is **chemical erosion**. Chemical erosion occurs when the plasma particles impact on the substrate atoms and react to form chemical compounds. This type of erosion, in the case of divertor PFCs, is particularly relevant for carbon base materials interacting with hydrogen isotopes. The mechanism of carbon chemical erosion is complex and temperature dependant compared to physical sputtering. A simplified mechanism of carbon erosion by deuterium ions bombardment is presented in Figure 4.2.

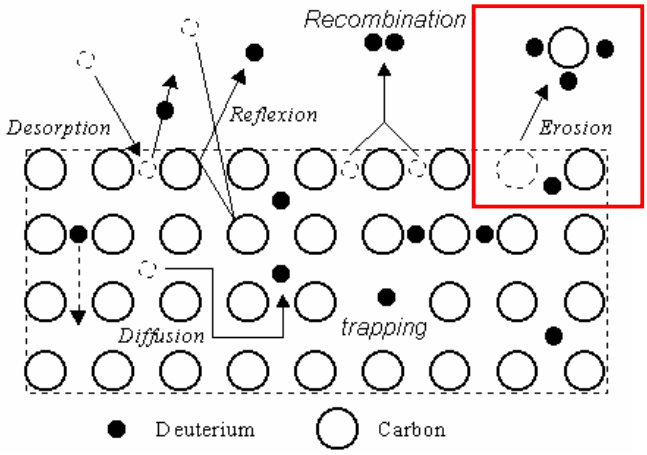

Figure 4.2. Schematic of the chemical erosion of carbon induced by deuterium bombardment [66]

There are several factors which determine the mode of carbon erosion under hydrogen bombardment [67]. At high temperatures, hydrogenation of carbon atoms to CH_3–C complexes occurs. The CH_3 radicals can be increasingly released from the substrate at temperatures above 400 K. The erosion yield, Y_{chem}, has a maximum in the temperature range 500-800 K , but is partially dependent on the energy of the incident ions – see Figure 4.3. At higher temperatures, chemical erosion becomes increasing suppressed because of the recombination of hydrogen ions and the consequent H_2 release.

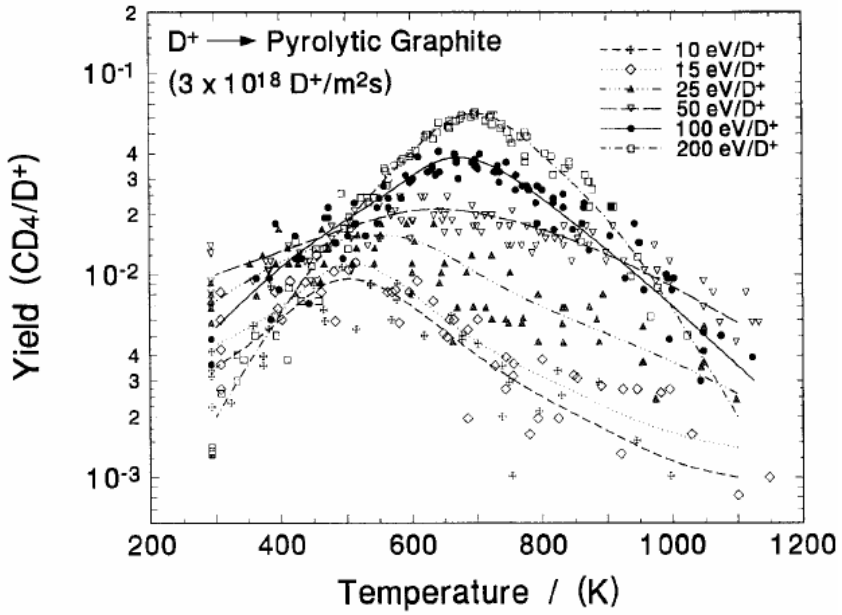

Figure 4.3. Temperature dependence of methane yield for low energy D^+ impact on pyrolytic graphite [69]

The hydrogenation reaction is enhanced by transfer of the kinetic energy in such a way that open carbon bonds are created to facilitate the attachment of hydrogen atoms. The effectiveness of this process in strongly dependent on the carbon crystallinity – the maximum erosion yields vary from 10^{-3} for well annealed pyrolytic graphite to 10^{-1} for amorphous carbon films [68].

At low temperatures there is no thermal release of hydrocarbons even though all broken bonds are hydrated. The hydrocarbon radicals, however, are bonded to the surface with a much smaller binding energy (~1 eV) than carbon atoms located in the lattice (7.4 eV). This leads to ion-induced desorption of hydrocarbon radicals.

The yield by chemical erosion is strongly dependent on the temperature and the ion energy, as illustrated in Figure 4.3. The higher the ion energy, the higher is the maximum erosion yield, which would be attained at higher temperatures with a lower ion energy. For the D^+ ions with an energy of 10 eV, the maximum chemical erosion yield at a given ion flux reaches 2×10^{-2} at 500 K whereas for the 200 eV ions energy, the maximum yield is close to 3×10^{-1} reached at 700 K. The chemical erosion is the predominant erosion mechanism for a carbon substrate bombarded with incident ions with energy levels below 100 eV. At higher energy levels physical sputtering becomes the major erosion process at room temperature.

The third erosion mechanism occurring during the divertor operation is melting in the case of tungsten, or sublimation in the case of carbon. The mechanism operates when the heat

flux exceed a particular limit, the limit being a characteristic of the individual material. Melting will seriously decrease the lifetime of PFCs. Melting, motion of the melt-layer and ejection of the molten material into the plasma causes significant plasma contamination. The melting point of tungsten is 3695 K, and the sublimation temperature for carbon is 3915 K. The conditions for melting or evaporation are unlikely to occur during normal operation, but could be reached if transient events occur, such as disruptions or edge localized modes (ELMs) . During such abnormal events, the divertor material is exposed to hot plasma streams and the localized impacts of runaway electrons. Energy densities occurring during ELMs are much less than would occur with serious disruptions, but still can reach 0.5–4 MJ m^{-2} [70].

Melting of the edges of tungsten samples starts above energy levels of 0.4 MJ m^{-2} while CFC erosion due to evaporation occurs above 0.5 MJ m^{-2} [71]. Therefore the ELMs density needs to be maintained at levels below 0.5 MJ m^{-2} otherwise strong erosion of both the CFC and the tungsten can be expected. During disruption events, the expected power load on the ITER PFCs can easily reach even 10–20 MJ m^{-2} [72][71]. Even single abnormal event with such a power load can lead to melting of tungsten to a depth of several hundreds of μm or evaporation of few μm of carbon [71], as presented in Figure 4.4.

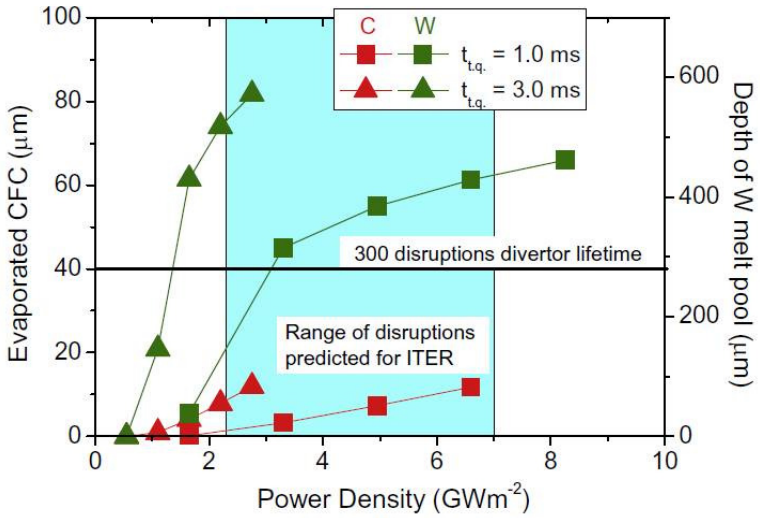

Figure 4.4. Erosion of CFC and tungsten per disruption as function of the transient heat load for transients of 1 and 3 ms [71]

In the figure, erosion per disruption as a function of power density for tungsten and CFC is presented. It's worth noting that with the given range of disruption conditions predicted for ITER, the evaporation of carbon does not appear to cause an unacceptable

working life (red points). For tungsten (green points), the erosion of material cause by the disruptions is too high to sustain the present assumption of 300 disruptions to ITERs operation during 20000 discharges [71]. Therefore, mitigation techniques need to be developed to guarantee minimization of the frequency of disruption. Appropriate techniques including the injection of high-pressure noble gas are currently under development [73].

4.2 Re-deposition

Release of material from the wall by the various erosion mechanisms and it's transportation in the plasma is followed by its **re-deposition** on different parts of the wall surfaces, including on the divertor PFCs. When quantifying the erosion and deposition rates two values are often determined – the net and gross rates. The net erosion or net re-deposition is defined as the difference between the amount of tungsten/carbon before and after exposure. The net erosion occurs when the amount of tungsten/carbon after the exposure is smaller than before. When the total amount of tungsten or carbon increases after the exposure, than the net re-deposition is present.

The gross erosion takes into account the erosion of in-between re-deposited material. The gross erosion, in this way, indicates the total value of the erosion occurring in the particular divertor position.

To determine the rate of erosion/re-deposition in the divertor region, special tiles with different types of markers are often used during one or more campaigns. The marker tiles are regular tiles with additional tungsten or carbon coatings of specified thickness, which can be post-mortem analyzed to determine the erosion or re-deposition rate at a particular divertor location. Additionally, analysis of the re-deposition, specifically the thickness, composition etc, may be performed on regular tiles removed from the divertor after a campaign.

The erosion and re-deposition processes have been extensively studied in different tokamaks [74][75][76][77][78].

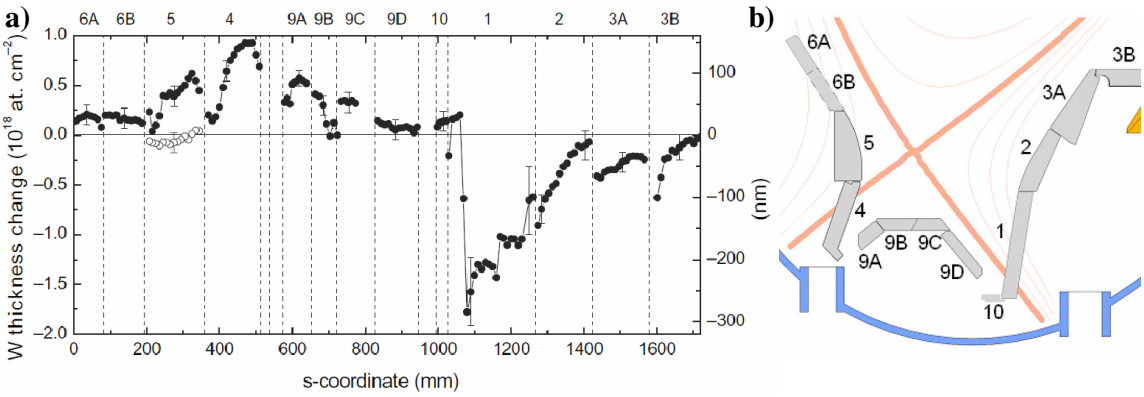

Figure 4.5. Erosion/re-deposition of tungsten from the marker tiles given in 10^{18} atoms cm^{-2} (lest axis) or nanometers (right axis) after the 2007 ASDEX Upgrade campaign. Negative values indicate net erosion, positive – net re-deposition. Top axis indicate the tile number whereas the bottom axis specifies the s-coordinate of the divertor (a). Additionally cross-sectional view of ASDES Upgrade divertor with strike-points is presented (b) [74]

Figure 4.5a presents an example of erosion/re-deposition studies performed in the ASDEX Upgrade tokamak after one full campaign in 2007. The change in tungsten thickness (given in atoms per cm^{-2} or in nm) is plotted as a function of divertor position. Negative values indicate net erosion, positive values indicate net re-deposition. The divertor position is determined by the s-coordinate (bottom axis) and indicated by tile number (top axis). Divertors cross-section with tiles numbers indication and strike-points positions is additionally presented in Figure 4.5b. All parts of the outer region of the divertor is an area of net erosion. The largest erosion occurs on tile 1, reaching a maximum value of around 0.1 nm s^{-1} close to the strike-point area which corresponds to the removal of near 300 nm of the tungsten layer during 3000 s standard discharge. During the whole campaign it was estimated that a total of 12.8 g of tungsten had been eroded of which 3.4 g was found to re-deposit in the inner divertor and about 2 g on the roof baffle. Both the inner divertor and the roof baffle are net deposition areas, but as indicated only about 40% of the eroded tungsten is being re-deposited there, whereas the rest of tungsten is either in the main chamber or as dust.

During the previous studies of erosion/re-deposition issues in the ASDEX Upgrade similar results were obtained. During the 2004-2005 campaign, the maximum tungsten erosion observed near the strike-point on the tile 1 was estimated at about 0.06 nm s^{-1}. The erosion of carbon was estimated as about 10-20 times greater than the erosion of tungsten. Furthermore, the erosion of carbon occurred in places where tungsten erosion was close to zero, indicating the presence of particles with energy below the physical sputtering threshold

for tungsten, which however were sufficient to cause carbon chemical erosion of the carbon [79].

Similar phenomena of net erosion in the outer divertor area was observed in the JT-60U [80] and JET [81] tokamaks. In both cases the highest erosion rates were found near the strike-point position, reaching 0.03 nm s^{-1} in the case of JET. Locally, however, dependent on the surface morphology, the erosion rates can be much higher. Surfaces inclined towards the incident particle fluxes exhibit a higher erosion rate compared to the bottom parts of recessions and pores which are screened from the incident fluxes. It follows that locally significant erosion can occur, markedly exceeding the mean values obtained from global investigations.

Compared to the outer divertor, the inner divertor region is a net re-deposition area for both carbon and tungsten in the current used divertor tokamaks [65][74][77][82]. The structure of a re-deposited layer varies between the tokamaks, depending strongly on the material used for the divertor PFCs and the operational conditions, specifically the surface temperature, different heat loads and particle fluxes etc.

With an entirely carbon device, the re-deposited layer consists mainly of carbon, but because of a high yield of carbon erosion, the thickness can reach relatively high values. Re-deposited layers with a thickness up to 60 μm were found on graphite tiles in the inner JT-60U divertor operated with all-carbon divertor following the June 1997–October 1998 working period [83]. The chemical composition of the re-deposited layer was 95 at. % of carbon with 3-4 at. % of boron (due to performed boronizations) and residual impurities of oxygen, iron, nickel and chromium. TEM studies showed that the films consisted of alternate regions of lamellar and columnar structures, as presented in Figure 4.6.

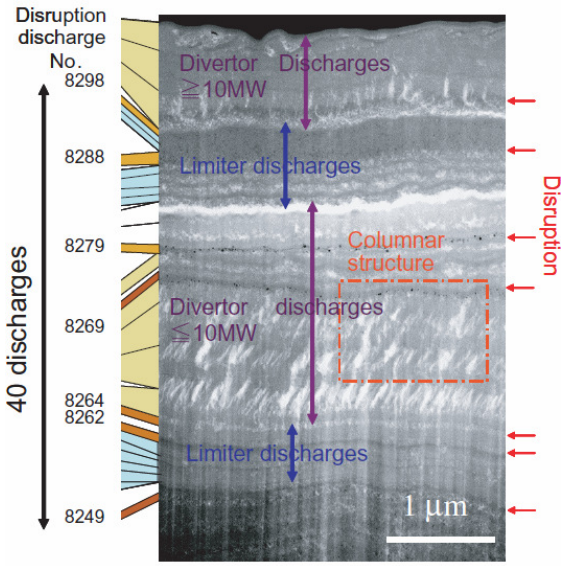

Figure 4.6. Cross-sectional TEM image of part of re-deposited layers on the inner divertor in JT-60U tokamak. Single discharge produce one sub-layer in the film and a disruption shot can be distinguished [84]

However, films formed during the 2001–2004 JET campaigns operated with carbon PFCs [77] had a maximum thickness up to 30 μm on the baffle region and up to 60 μm near the area exposed to the plasma. The structure of the re-deposited layer was different from those observed in the JT-60U as the JET films have a layer structure consisting mainly of globules. No columnar structure was observed. The reason for different film structure at JT-60U and JET is still unclear, but could be caused by the different vacuum vessel temperature and the different heat and particle loads experienced by the inner divertor [77].

A similar lamellar structure in the re-deposited layer was observed after a campaign at the ASDEX Upgrade in 2007. The divertor PFCs were made entirely of tungsten, nevertheless residual carbon from previous operations were still present in the machine. The lower erosion yield of tungsten resulted in a much thinner film compared to the full carbon devices. Locally, the thickness of the re-deposited layers was up 2 μm. SIMS (second ion mass spectroscopy) investigation revealed that the film contained a mixture of tungsten, carbon, boron and deuterium [74].

In general it can be concluded that the global erosion and re-deposition processes have been well studied in different tokamaks. The main features of the re-deposited layers have been investigated, however detailed studies of the morphology and phase composition are yet to be undertaken. The morphology of the re-deposited films containing a mixture of carbon and tungsten is very important because of its influence on the divertor operation for example

on the erosion yields. The phase compositions of re-deposited layers formed on a TEXTOR limiter were investigated by Psoda et al using XRD [85]. It was established that the layers were rich in carbon and tungsten and the mains phase detected were WC with traces of the W_2C phase. However, the morphology and space distribution of both phases remain still unknown.

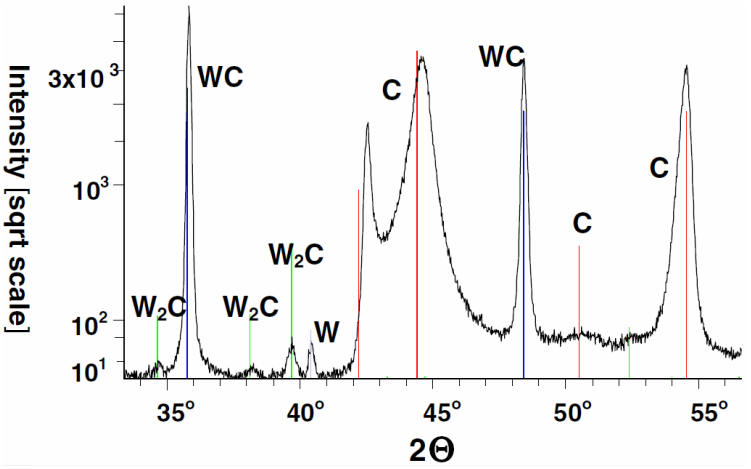

Figure 4.7. XRD spectrum showing major and trace phases in re-deposited layer created on TEXTOR tokamak limiter [85]

The morphology and phase composition of re-deposited films have a significant influence on their properties during the divertor operation. The laboratory studies of tungsten doped carbon films imitating a real structure of re-deposited film are performed, mostly with regard to erosion. Complex studies on the influence of a tungsten dopant on the erosion yield changes compared to pure carbon films has been performed by Balden et al. [86][87]. Figure 4.8 shows the total erosion yield of pure carbon and tungsten doped carbon films implanted with 200 eV deuterium ions. The influence of the tungsten concentration (Figure 4.8a) and the implantation temperature (Figure 4.8b) is presented [88].

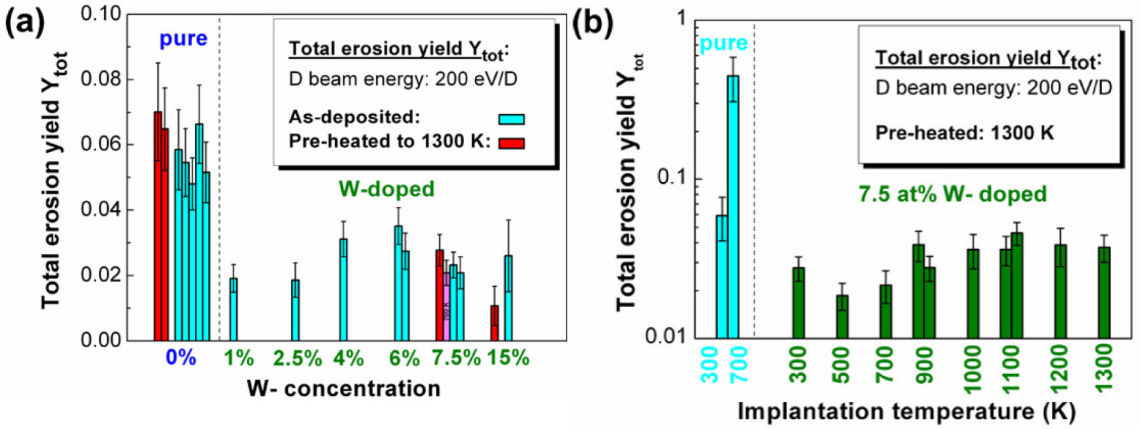

Figure 4.8. Total erosion yield of pure carbon and tungsten doped carbon films implanted with a D beam of 200 eV/D. (a) Implantation temperature: 300 K. (b) Implantation temperatures: 300–1300 K. The pre-heating temperature (a) and the tungsten concentration (b) were fixed at 1300 K and 7.5 at. %, respectively [88]

The addition of a tungsten dopant reduced the total erosion yield to between 50 – 66 % of that which occurred with pure carbon films. The maximum erosion yield occurred on a sample with 6 at. % of tungsten is unexpected and needs to be verified. Pre-annealing at 1300 K does not change significantly the total erosion yield in the case of a sample with 7.5 at. % of tungsten. The sample with 15 at. % of tungsten pre-annealed at 1300 K reduced the erosion yield to half that of the as-deposited sample and by almost 90% when compared to pure carbon films. The reduction of the erosion yield is most likely related to structural modification of the deposited films (e.g. carbide creation). At deuterium implantation temperatures (300 to 700 K) no significant modification of the erosion yield was observed for a sample doped with 7.5 at. % of tungsten (Figure 4.8b). During the implantation at 700 K the total erosion yield of tungsten doped sample is reduced by a factor of 20 compared to a pure carbon film. By increasing the implantation temperature from 700 K to 900 K the total erosion yield increased by a factor of two and did not change significantly at higher implantation temperatures.

Since the laboratory experiments involving the investigation of erosion mechanism of tungsten doped carbon films show quite different film properties compared to pure carbon films, there is a crucial need to fully identify their structure. In particular, detailed phase identification in the re-deposited layers is relevant. A study of tungsten doped carbon films will provide a better understanding of the formation conditions of re-deposited layers which have been shown to contain a mixture of carbon and tungsten.

4.3 Ion implantation and neutron irradiation

Tungsten and carbon, as a fusion plasma facing materials are also exposed to intense fluxes of energetic hydrogen and helium ions and neutrals. In the case of carbon, impact by ions which already possess relatively low energy ions, causes surface erosion, principally by chemical erosion (in the case of hydrogen ions). Where tungsten is employed, the impacting ions and particles possess energy levels below the threshold required for physical sputtering and therefore erosion does not occur. Nevertheless, tungsten implantation with hydrogen or helium ions (both present during the fusion reaction) leads to other structural degradation mechanisms other than erosion.

A variety of surface degradation, such as bubble and void formation, vacancy swelling, blistering and surface porosity have been detected after irradiation with helium or hydrogen [89][90][91][92]. Figure 4.9 presents the SEM cross-section images of tungsten implanted with low energy (38 eV/D) high-flux (10^{22} D/m^2 s) deuterium ions at different temperatures.

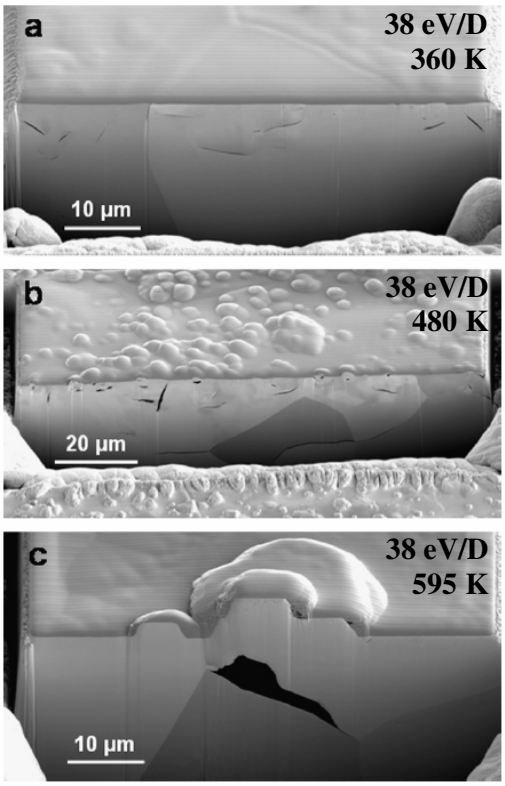

Figure 4.9. Cross sectional images of recrystallized W exposed to low-energy (38 eV/D), high-flux (10^{22} D/m^2 s) D plasma with an ion fluence of 10^{27} D/m^2 at 360 K (a), 480 K (b), and 595 K (c) [93]

A characteristic feature of a post-implanted structure is the so called blister structure. With an increase in the temperature of implantation, blisters are formed at the tungsten surface having a size larger than 0.5 – 2 μm at 320-400 K and 10–30 μm in the temperature range 460–570 K. At implantation temperatures, above 700 K, no blistering effect is observed. However, a specific three-dimensional sub-surface defect appears in the form of fine intragranular crack-like defects with a width of 0.1 μm and length of 5 μm at 360 K (Figure 4.9a) or large cavities with a volume of hundreds of cubic microns at 595 K (Figure 4.9c) [93].

The creation of blister-like structures is explained by large deuterium concentration, which exceed the solubility limit and causes internal stresses in the lattice of the tungsten matrix. To alleviate the stress, deformation occurs, which is assumed to be responsible for the generation of vacancies, vacancy complexes and microscopic cavities at a depth of several micrometers and the concurrent accumulation of diffusing deuterium [93]. As recently confirmed, a part of the spherical blisters are fully elastic deformations. The experiments involving opening individual blisters with a focused ion beam (FIB) and in situ observation of their complete relaxation by scanning electron microscopy has also been performed. The release of the D_2 gas filling each blister was confirmed [94].

Irradiation with pure helium, as opposed to pure hydrogen irradiation, leads to bubble formation with sizes from nanometers up to few micrometers, near the tungsten surface. The sizes of the bubbles depend on exposure conditions such as the energy of implanted ions, substrate temperature, etc.. Helium ions impinging on the tungsten surface are trapped at vacancies, grain boundaries, dislocations, and other defects but at much more shallow surface region because of the very low solubility of helium in tungsten. As the amount of helium in the tungsten is increased, the helium atoms are trapped at helium-vacancies complex and form bubbles [95].

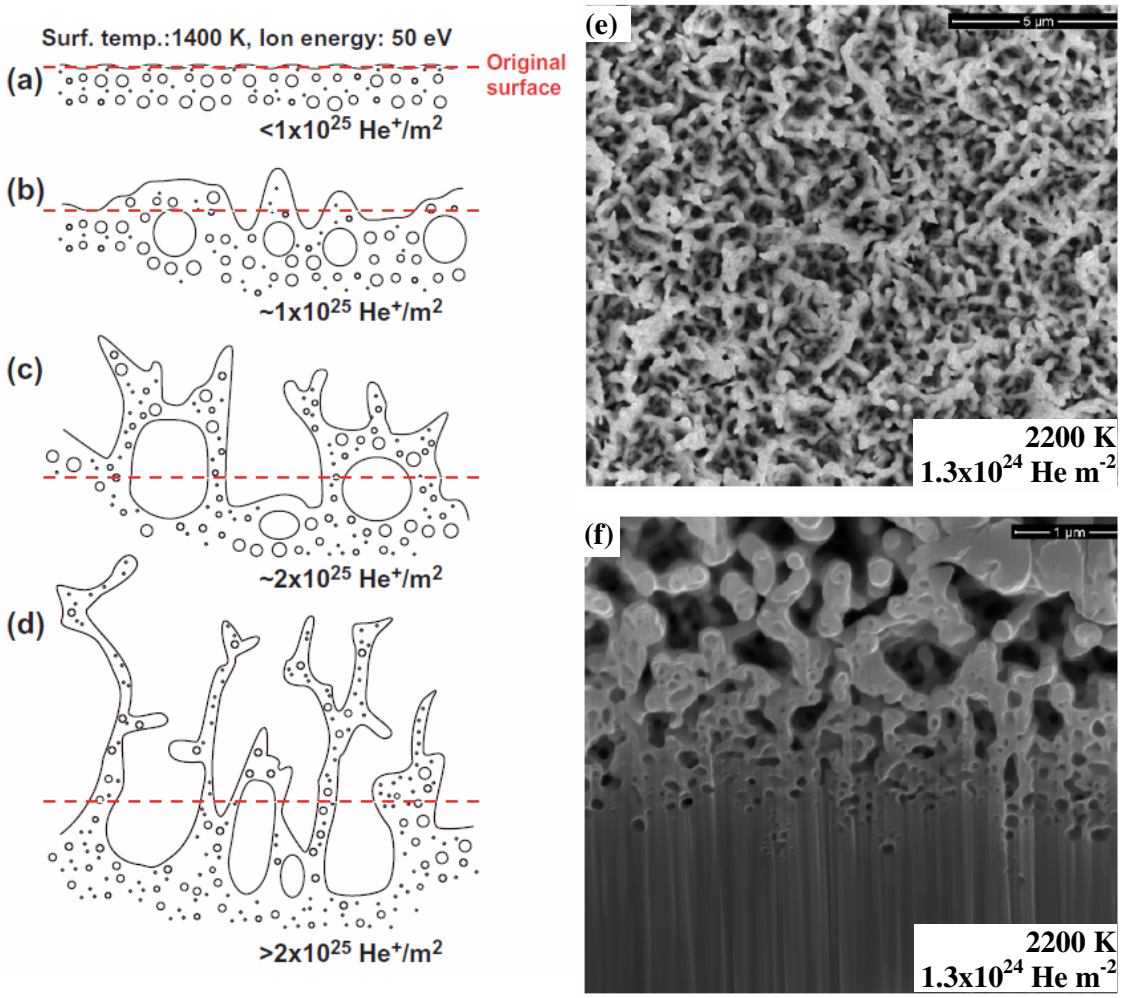

Figure 4.10. A schematic representation of the coral-like nanostructure formation process (a-d) [96]. On the right hand side a SEM image of top view (e) and FIB cross section (f) of the sample irradiated with pure helium showing the coral-like surface structure together with bubble agglomeration [92]

Exposure to helium at higher temperatures leads to the growth of a coral-like surface structures [92], as presented schematically in Figure 4.10a-d and in the SEM image of the top view (Figure 4.10e) and FIB cross-section (Figure 4.10f). In the first stage, nanometer size bubbles start to form in the near surface layers, the thickness of which depends mostly on the surface temperature. Growing bubbles can thermally migrate and coalescence. Enlarged bubbles, with the help of active surface diffusion, migrate to break the surface. Additionally, large bubbles push up the surface to form blisters. Further irradiation makes the blisters burst, which causes the formation of protrusions on the surface [96].

It should be noted that, the helium bubble formation has the effect of suppressing the formation of hydrogen blisters on tungsten when exposed to helium-seeded deuterium

implantation. An example of the effect of deuterium plasma with a helium addition on a tungsten surface is presented in Figure 4.11 [97].

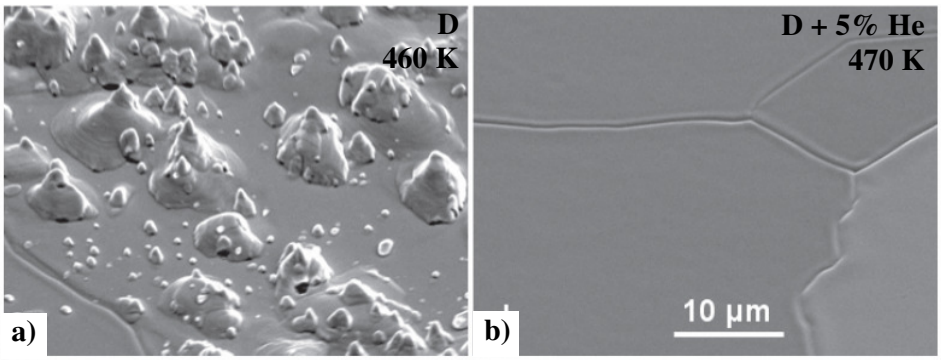

Figure 4.11. SEM images of re-crystallized W exposed to a pure D plasma (38 eVD^{-1}) at 460 K (a) and a helium-seeded D plasma (38 eVD^{-1} + 76 eV He^{-1}, 5% of He ions) at 470 K (b). In both cases D ion fluence of 10^{27} Dm^{-2} [97]

The concentration of helium ions of 0.1% at an exposure temperature of 335 K does not change the morphology of the tungsten surface, whereas implantation at 495 K leads to blisters suppression. Implantation at temperatures above 600 K with a mixture of hydrogen and helium leads to no blister formation. An increase in the concentration of helium ions to 5% at implantation temperatures between 340–430 K reduces the tendency to form blisters (Figure 4.11b). Exposure to the helium-seeded deuterium plasma at temperatures of 460–530 K prevents from blister formation. The presence of helium ions in the deuterium plasma reduces the retention of deuterium in tungsten at elevated temperatures and in this way prevents blister formation [97]. Most of the deuterium is quickly desorbed and leaves the tungsten at low temperatures [98].

The creation of blisters structures due to hydrogen and helium irradiation does not seem to be an issue when considering the tokamak plasma conditions. The blister formation has been reported on polished tungsten, but no or only a few blisters occur on technically machined, unpolished surfaces [19].

In addition to ion and particle irradiation, fusion plasma facing components will be subjected to intense **irradiation by neutrons**, which will cause modifications of material's structure and a degradation of the mechanical properties and thermal conductivity. Neutron irradiation can cause displacement of the substrate lattice to form vacancy-interstitial pairs, expressed as the displacement per atom, dpa. The dpa is a measure of the 'displacement

energy' deposited by an irradiating particle, in terms of the number of atoms that could possibly be permanently displaced from their lattice sites to stable interstitial positions.

Neutron irradiation leads to tungsten hardening and embrittlement. The production of defects and their subsequent diffusion, recombination and agglomeration due to neutron irradiation causes a loss of strength at grain boundaries. The ductile-to-brittle transition temperature (DBTT) is raised by neutron irradiation and causes an increase in brittleness and an increased creep rate at elevated temperatures. This effect is dependent on the irradiation temperature and the magnitude of the irradiation dose. For a low irradiation temperatures, hardening and embrittlement was observed as the DBTT was raised from around 470 K to 770 – 970 K after irradiation at a temperatures of about 770 K with a dose of tens of dpa [100]. Tungsten specimens exhibited brittle fracture at stress levels 5 to 10 times lower than specimens tested in the un-irradiated conditions. That fact reduce the temperature operation window at lower range and can cause brittle cracking at lower working temperatures. Besides the increase of the DBTT, evidence of tungsten swelling causes by neutron irradiation was reported. The maximum degree of the swelling was 1.7% obtained for 9.7 dpa at 1070 K [101]. Additionally, a microstructural change involving the formation of superlattice voids with a diameter up to 20 nm was observed after neutron irradiation at 820 K of 7 dpa [100].

Neutron radiation of carbon leads to change in the thermal conductivity which is induced by the formation of radiation defects, which act as obstacles for phonon propagation. The size and concentration of the radiation defects depend on the applied irradiation conditions. An increase in the irradiation temperature leads to a decrease in the degradation of the thermal conductivity, and the effect in negligible if the irradiation temperature is greater than about 1770 K [100]. However, the thermal conductivity of irradiated CFC can be partially restored by annealing. Neutron irradiation leads to the displacement of carbon atoms, which may form dislocation loops or graphite planes leading to dimensional changes. Irradiation at temperatures between 570 – 1470 K and damage close to 0.1 dpa caused the CFC composite to shrink by about 0.1-0.2%. Higher damage doses, close to 1 dpa, increased the dimensional changes to nearer 0.5%. Additionally, an increased irradiation temperature led to greater dimension changes [101]. The main issue, however, concerning the neutron irradiation of carbon, is the increased erosion of irradiated carbon base material.

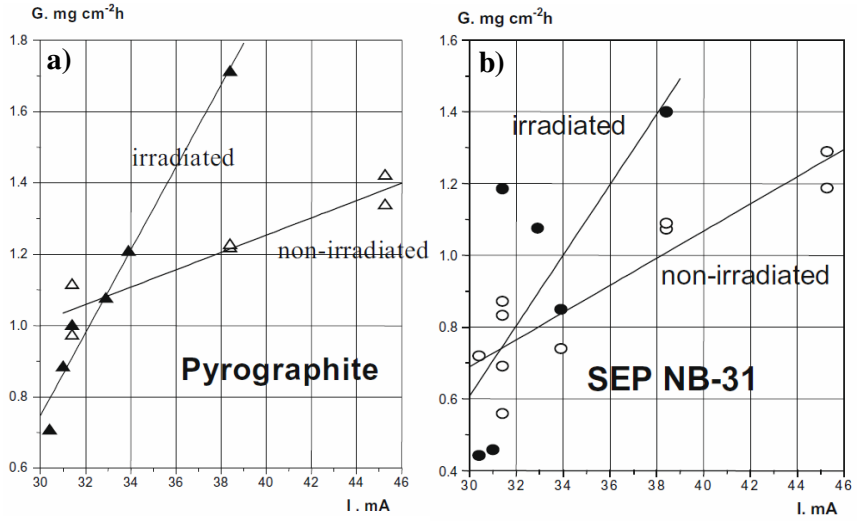

Figure 4.12. Erosion rate of neutron irradiated and non-irradiated pyrolytic graphite (a) and CFC (b) versus plasma ion flux [102]

Figure 4.12 presents the erosion rate of carbon due to irradiation causing accumulated radiation damage close to 10 dpa. The irradiated and non-irradiated graphite and CFC composite were subsequently exposed to steady-state deuterium plasma. An increased erosion yield in both irradiated carbon materials is evident. Inevitably the irradiated materials exhibited greater evidence of surface modifications, caused by erosion, than the non-irradiated materials. The modification of the surface due to erosion becomes more pronounced on irradiated materials [102].

In the case of ITER the predicted radiation damage is at a level of 0.6 dpa [71] to 0.7 dpa [19] in the divertor region. Such neutron fluxes will not cause significant structural degradation of the materials. Nevertheless, in the case of DEMO, the future planed fusion power plant, and for commercial fusion reactors, the problems of the effect of neutron irradiation on materials will become more crucial and will have a significant effect on the design and selection of the materials selected for the armour.

4.4 High temperature

In addition to consideration of the structural degradation mechanisms occurring because of the operating conditions of the divertor, it is necessary to take into account the structural changes in PFCs, induced by the high operation temperature. During the steady state operation of ITER's divertor surface temperatures in the range of 800-1200 K are

expected. However, much higher temperatures, even well above 3000 K, may be reached during the abnormal events, such as disruptions.

At very high temperatures tungsten may exhibit various negative changes. Firstly, at a temperature close to 3700 K tungsten begins to melt, as has already been described in the previous section on erosion. At lower temperatures, typically above 1500 K [103] tungsten may recrystallize. After recrystallization, tungsten will possess a different microstructure and exhibit different mechanical properties which can influence its performance under the loads imposed by thermal shock. According to Uytdenhouwen et al. [104] tungsten recrystallisation reduces its resistance to thermal shocks. When subjected to thermal shock the recrystallised tungsten showed more pronounced cracking surrounding the loaded area, compared to the as-received tungsten. When considering low temperatures, there is a negative effect know as ductile-to-brittle transition causing tungsten to become brittle below a certain temperature. Hirai et al. [105] reported on crack generation under single pulse thermal shock tests at different temperatures studied in an electron beam facility. Major cracks appeared only after loading at 470 K and did not occur with tests carried our at higher temperatures. That crack generation was considered to be directly linked to the brittleness of tungsten at that temperature.

A high operation temperature also has a negative effect on tungsten coatings deposited on carbons substrates. At elevated temperatures, carbon diffusion takes place leading to the formation of brittle carbide at the interface region. Brittle carbides cause significant deterioration of the thermo-mechanical properties of the tungsten coating. Although there is evidence of the negative effect of brittle carbide formation, the data on kinetics of carbide formation for specific coating is not currently available.

5 Research objective

A critical concern for the design and construction of a fusion reactor having a magnetically confined plasma is the effect of the interaction of the plasma with the material components of the reactor device. The vessel's components exposed to the plasma have to act as a heat sink for the energy and be resistant to the particles released from the plasma. However, the bombardment of the materials by the particles combined with the extremely high temperature may lead to atoms being released from the wall materials. In addition the particle bombardment and the high energy flux may induce changes in the microstructure of the material which may significantly limit the lifetime of the plasma facing components.

The main objective of the research was to determine the mechanism and the kinetics of the structural degradation of the divertor materials, in both experimental and the operating environment of a real fusion device, by the use of advanced electron microscopy. The major factors which limit the working lifetime of the plasma facing components are erosion and the subsequent re-deposition of the material and, when tungsten coatings are applied to carbon substrates, the formation of carbides caused by the diffusion of carbon into the tungsten. These aspects have led to two issues being investigated in the research programme for which the following hypotheses were proposed.

1. *The degradation of divertor components with a Mo/W coating system on a carbon substrate is controlled by carbon diffusion which results in the formation of brittle carbide phases.*

2. *The re-deposited layer on the carbon and tungsten divertor elements possesses a nanocrystalline structure having a complex phase composition which is dependant on the conditions during its gradual growth during the operational life.*

6 Experimental

6.1 Material preparation

6.1.1 Mo/W coated CFC on the JET divertor tile (Culham, United Kingdom)

A comprehensive research program has been undertaken in the present study to determine the kinetics and degradation mechanism of Mo/W coatings systems on CFC substrates. The samples were prepared in the same manner as the divertor tiles installed in the JET reactor. Bi-directional carbon-fibre reinforced carbon (CFC) substrate were coated with a 2-4 μm molybdenum interlayer and an outer coating of 10-15 μm of tungsten. The deposition process performed by combined magnetron sputtering and ion implantation technology (CMSII) was carried out at the National Institute for Laser, Plasma and Radiation Physics (NILPR) in Bucharest [35]. The deposition technique consisted of magnetron sputtering together with high energy ion bombardment. During the deposition magnetron discharge, DC bias discharge and high voltage pulse discharge were combined sequentially. The plasma ions from the magnetron discharge were accelerated by a high voltage discharge. Typical parameters of the high voltage discharge were – U = 30-50 kV, τ = 20 μs, f = 25 Hz. Between the high voltage pulses, DC bias up to -900 V was applied. Both the Mo and W deposition was undertaken in one cycle, since both Mo and W magnetron targets are installed. The coated tiles were firstly rotated in front of the Mo targets, and then in front of the W targets. The deposition rate was in the range of 4-8 μm/h and the deposition temperature was ~673K.

In order to determine the rate of degradation, the samples with the dimensions 10 mm x 10 mm x 3 mm were annealed at different temperatures for various times:

- **1370 K** – 0.5 h, 1 h, 2 h, 5 h, 20 h
- **1470 K** – 0.5 h, 1 h, 2 h, 5 h, 20 h
- **1620 K** – 0.5 h, 1 h, 2 h, 5 h, 20 h

The heat treatment was performed in a high temperature furnace operated with an Ar atmosphere. The furnace chamber containing the sample was purged with Ar three times at room temperature and three times at 670 K to remove air and avoid oxidation of the tungsten during annealing. Since the inert part of the furnace was graphite, each sample was covered with a tungsten “envelope” of thin tungsten foil to exclude the possibility of the sample

surface coming into contact with the surrounding carbon, a situation which could invalidate the subsequent measurements.

The kinetics of the carbon diffusion was determined by the thickness measurement of the thickness of tungsten carbodes using the SEM images of FIB prepared cross-section. The tungsten and molybdenum carbide phases were identified by using STEM and nano-diffraction methods.

6.1.2 W doped amorphous C films

The other phenomenon, which has to be considered with regard to degradation processes taking place in the divertor, is the re-deposition of the material previously eroded from plasma facing components. In order to have an insight into the these processes, a set of amorphous carbon films doped with different concentrations of tungsten (a:C-W) were produced as a model system to analyse the creation conditions of the re-deposited layers. The films were deposited on pyrolytic graphite and a single crystal (100) silicon wafer by a dual source Leybold Unnex 450 C magnetron sputtering device using argon as the sputtering gas. Both graphite and tungsten cathodes were supplied using a DC generator, with a fixed 600W power on graphite, and variable power in the range 6W to 20W on tungsten. The variable DC power on the tungsten cathode enabled different tungsten concentration in the deposited film to be obtained.

Samples with tungsten concentrations of 9, 18 and 22 at. % in the deposited films were produced. The average film thickness was 2.5 – 3.5 μm. In addition a multilayered sample consisting of 7 sublayers, each with different tungsten concentrations: 25, 13.5, 16, 18.7, 20.7, 22.3 and 24 at. % of tungsten respectively, with a total thickness of 4.5 μm was produced. Before the deposition, all substrates were etched with an argon plasma to remove the oxide layer. During the deposition, the temperature of the samples did not exceed 350K, and the deposition rate was ~ 100 – 140 nm/h, depending on the DC power applied to the tungsten cathode. The samples were mounted on a rotating tables during the deposition process to guarantee a uniform composition and film thickness. The specimen holder was not biased for all depositions.

The elemental composition of each film was determined with the use Rutherford backscattering spectroscopy (RBS) using ^{4}He at 4 MeV in the tandem accelerator facility with a 165° scattering angle. Both, the deposition process and atomic elemental composition identification by RBS, were undertaken at the Max-Planck-Institut für Plasmaphysik (IPP) in Garching.

Table 6.1. Performed annealing of a:C-W films with different W concentration at different temperatures, together STEM investigation information

	1100 K	1450 K	2200 K	2500 K	2800 K
9% W		S	S	S	S
18% W	S	S	S		S
22% W	S	S			
multilayer			S		

Where **S** stand for STEM investigation.

Tungsten doped carbon films prepared in this way were annealed for one hour (as presented in Table 6.1) to achieve different crystallites sizes and phase compositions of tungsten carbide. Annealing was carried out in a high temperature graphite furnace with an Ar or He atmosphere. The furnace chamber containing the samples was purged with Ar or He three times at room temperature and three times at 670 K to ensure the absence of air and avoid tungsten oxidation during annealing.

Preliminary phase identification was performed by XRD. STEM nano-diffraction was used to accurately analyse the carbide phases and composition. Determination of the average crystallite size was based on the STEM bright field and Z-contrast images.

6.1.3 Re-deposited layer from ASDEX Upgrade (Garching, Germany)

In order to confirm the reliability of the model studies, the structure and phase composition of re-deposition layer was carried out on the material at the divertor inner strike point on tile 04/1 installed in ASDEX Upgrade during the 2007 campaign. The tile was located at the position indicated on the diagram of the ASDEX Upgrade divertor cross section (Figure 6.1).

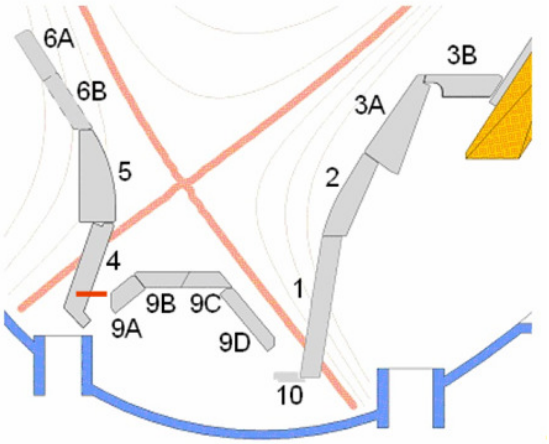

Figure 6.1. Scheme of the ASDES Upgrade divertor cross-section with marked position of re-deposit analysis with the s-coordinate of ~ 510 mm [74]

The precise location in the divertor can be described by poloidal s-coordinates which is the length through the divertor starting from 6A to the 3B part. The position of detailed examination s ~ 510 mm, was selected based on previous investigation on erosion and re-deposition inside the reactor [74]. The location with greatest amount of re-deposition was chosen. The total discharge time was 2620 s and no boronizations were performed during the campaign.

All the tiles used during the operation were composed of fine grained graphite coated with tungsten by physical vapour deposition (PVD). During the 7 year period before the 2007 campaign all carbon facing components were exchanged for tungsten components and the interior of the reactor was cleaned to remove all residual carbon after the whole exchange period. This procedure provided the opportunity to monitor and gain a better understand of the re-deposition of eroded carbon onto the tungsten wall material, knowledge which will be extremely important when considering processes that will occur during the operation of ITER.

The preliminary identification of phases in the re-deposited layer was performed by XRD. The thickness of the layer, its morphology and detailed phase identification of the materials in the re-deposited layer was undertaken with STEM microscopy and electron nano-diffraction.

6.2 Characterization techniques

6.2.1 Focused Ion Beam (FIB) (Scanning Ion Microscopy)

The Focused Ion Beam (FIB) technique, also referred to as Scanning Ion Microscopy, has been employed primarily as a method for specimen preparation to facilitate further electron microscopy investigation. The principle of the technique, like Scanning Electron Microscopy (SEM), is based on scanning the sample with a fine probe and detecting the resulting signal. In contrast to SEM, FIB uses Ga^+ ions which have a much larger mass than electrons. Accelerated Ga^+ ions possess sufficient energy to cause sputtering of the investigated material. This combined with proper control and a small scanning probe makes it a useful tool for small scale accurate machining of material to prepare the required specimens for subsequent studies.

There are two types of FIB devices - so called single beam devices, consisting of a single FIB column only, or dual beam system as a combination of two - FIB and SEM - columns (normally at a 50-60° angle to each other).

In the reported work, three FIB devices were used:

- a single beam Hitachi FB2100, with 40 kV Ga^+ ion source and a maximum beam current of 45 nA,
- a dual beam system – FEI Helios NanoLab 600 equipped with 30 kV Ga^+ ion source and a maximum probe current 20 nA,
- a dual beam system - Hitachi NB5000 with 40 kV Ga^+ ion source and maximum beam current of 80 nA.

The FIB technique was used for two purposes:

- preparation of thin lamella
- producing cross-sections

Thin lamella machining was carried out on all types of FIB devices to obtain electron transparent sample for subsequent STEM investigation. Since STEM investigation requires samples that no greater than 100 nm thick, the FIB is a very convenient tool for machining thin flat samples. The preparation consisted of cutting out the required section of the material, removing it and mounting it on a special STEM grid for final thinning to the required sample thickness, as indicated in Figure 6.2. The final thinning was always performed using 40 kV (using Hitachi NB5000 or FB2100) and beam current of 20 pA, obtained by selecting a 15 μm

aperture. Sample tilting during final thinning varied over the range of 1-1.5°, depending on the prepared material. In general, for a:C-W films and ASDEX Upgrede re-deposited layers the angle was close to 1° and for Mo/W coatings systems on CFC the angle was 1.5°.

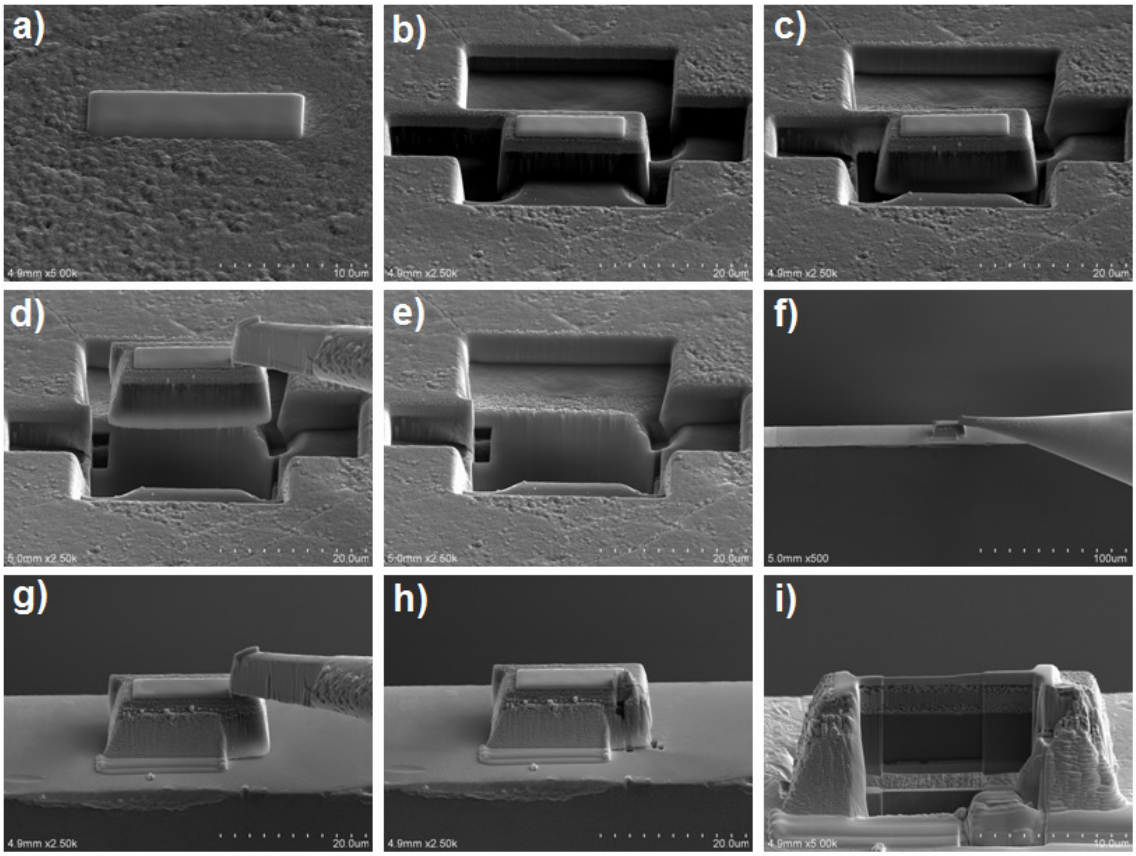

Figure 6.2. Scheme representation thin lamella preparation lift-out technique in FIB – tungsten protection coating deposited on the interesting feature (a); sputtering of the material around the interesting area for further lift-out (b); bottom cut-of (c); mounting to the transporting tungsten needle, cutting of the connection bridge and lifting-out (d); empty space left after the lift-out (e); fixing the lifted-out material to the copper mounting grid (f, g); removing the tungsten needle connection– the material is now free on the copper grid (h), thinning down to achieve the electron transparency – normally to 100 nm thickness and below (i)

Cross sections were prepared using only the dual beam systems to obtain the possibility of simultaneous observation using SEM. The method of FIB cross sectioning combined the removal of material from the sample, to expose features not visible on the surface, together with SEM observation of the revealed sample details. The cross section face was a plane perpendicular to and below the surface of the sample, as presented in Figure 6.3. Final surface cleaning was always performed with a 0.92 nA beam current if using the FEI Helios, and with 0.96 nA by selecting 80 μm dimension aperture with the Hitachi NB5000.

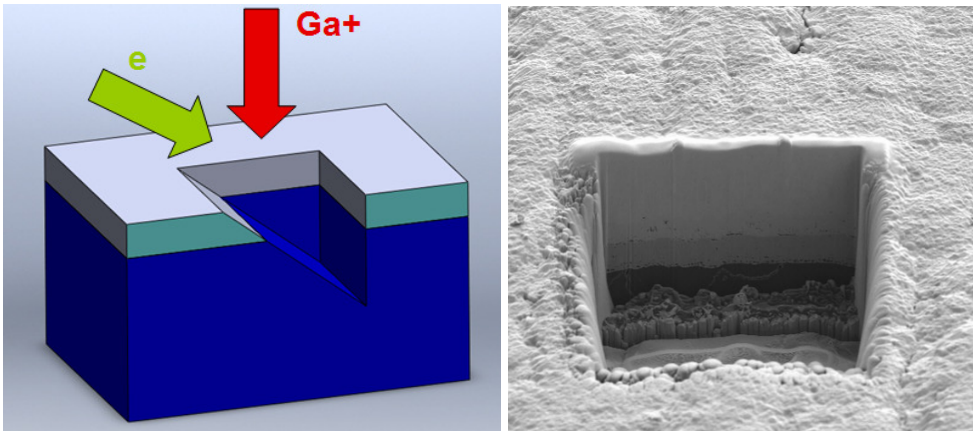

Figure 6.3. Scheme of cross-section preparation (a), example of SEM image of the FIB prepared cross-section (b)

Because the dual beam device the FIB and SEM column are at a specific angle to one another and the FIB sputtering direction is perpendicular to the surface, whereas SEM observation is at an angle, all measurements based on the SEM images need to be corrected. The actual thickness was determined by dividing the distance measured on an SEM image by sin(α), as presented in Figure 6.4. This method was used wherever the thickness based on FIB/SEM cross-sectioning has been presented.

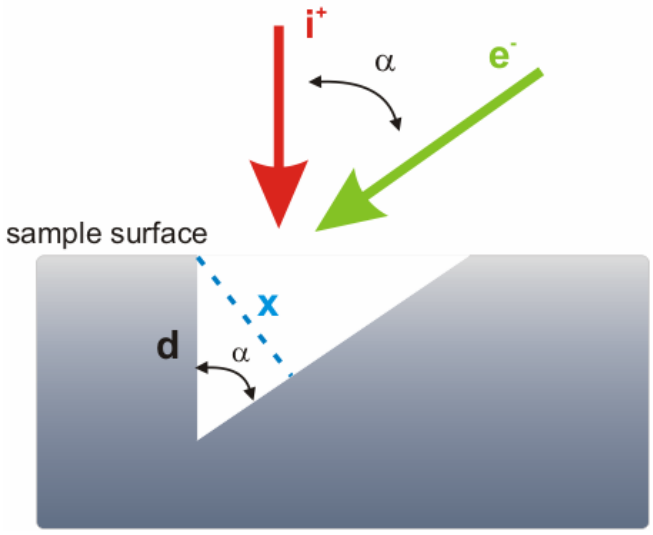

d – real thickness,
x – thickness measured on the SEM image,
α – angle between FIB and SEM column:
FEI Helios - 52°,
Hitachi NB - 58°,

$$d = \frac{x}{\sin\alpha} \qquad (6.1)$$

Figure 6.4. Scheme of SEM cross-section thickness measurement correction, where d – real thickness, x – thickness measured on SEM image, α – angle between FIB and SEM column

Additionally, the dual beam FIB devices were also used to obtain SEM images of the microstructures (employing the SEM column). All observation were carried out at 5 kV or 10 kV with a beam current of 86 pA on the FEI Helios and in a high current mode with the Hitachi NB5000. These observation setting gave the optimum conditions for revealing the orientation and mass contrast enabling to distinguish the different phases on SEM image.

6.2.2 Scanning Transmission Electron Microscopy (STEM)

High resolution observations of the microstructures were made using a dedicated STEM equipped with a 200 kV Schottky field emission electron source with a beam current of ~100 nA and a Cs spherical aberration corrected Hitachi HD2700. The point resolution in that device is down to 1.4 Å. The microscope was equipped with EELS (electron energy loss spectrometry) and EDS (energy dispersive spectrometry) detectors for chemical analysis and a CCD camera for recording diffraction images. Atomic resolution observations were performed in the bright field (BF) mode and high angle annular dark field (HAADF) mode, also called Z-contrast in which contrast is generated by electrons which are not Bragg scattered and their intensity is proportional to Z^2. The carbide sizes were determined of the basis of the STEM Z-contrast and BF images.

Together with the imaging, phase analysis was undertaken by diffraction methods. Diffraction analyses were carried out by the so called nano-diffraction mode which is a novel and elegant technique employed in a STEM and is similar to convergent beam electron diffraction (CBED) carried out in classical TEM, however the convergence angle is much smaller. It provides the possibility of obtaining diffraction images from nanometer scale objects by virtue of the use of very small probe diameter (2 nm and less), which makes it possible to obtain single crystal diffraction images of very small objects having a size of less than 5 nm.

6.2.3 X-Ray diffraction (XRD)

The initial phase identification together with estimates of crystallite sizes were carried out by X-ray diffraction (XRD) using a Seifert XRD 3003 PTS diffractometer operated with Cu Kα (0.154 nm) radiation. The spectra were acquired using theta-scans at an incident angle of 5° in the range between 2theta of 30-90°. Phase determination was done by comparison with the JCPDS ICDD database [107]. The estimates of crystallite size was based on Scherrer's formula with a pre-factor of 1 [108], assuming that XRD peak broadening is only

related to a reduction in crystallite size. However, some of the recorded XRD peak broadening was due to phase overlapping, making the identification of the carbide difficult or impossible. Sherrer's formula was employed for crystallites size determination up to 100 nm.

6.2.4 Micro-scratch test

To determine the mechanical properties degradation of the Mo/W coated CFC mechanical properties due to brittle carbide formation, a micro scratch test was performed using REVETEST Scratch Testing instrument equipped with 200 μm diamond ball as an indenter. Applied load was linearly increasing from 1 N to 6 N with the indenter sliding rate 0.05 mm/s. A critical load to coatings failure was measured. In all cases, after the micro-scratch test a FIB cross-sections were prepared near the failure area and a SEM observations were performed.

7 Results and discussion

7.1 Mechanism and kinetics of the degradation of CFC/Mo/W coating system

Figure 7.1 presents SEM images of the Mo/W coated CFC before and after annealing at 1370 K for various periods. In the initial state, the average thickness of the tungsten coating was 12.7 ± 1.2 μm and that of molybdenum interlayer 4.0 ± 0.9 μm.

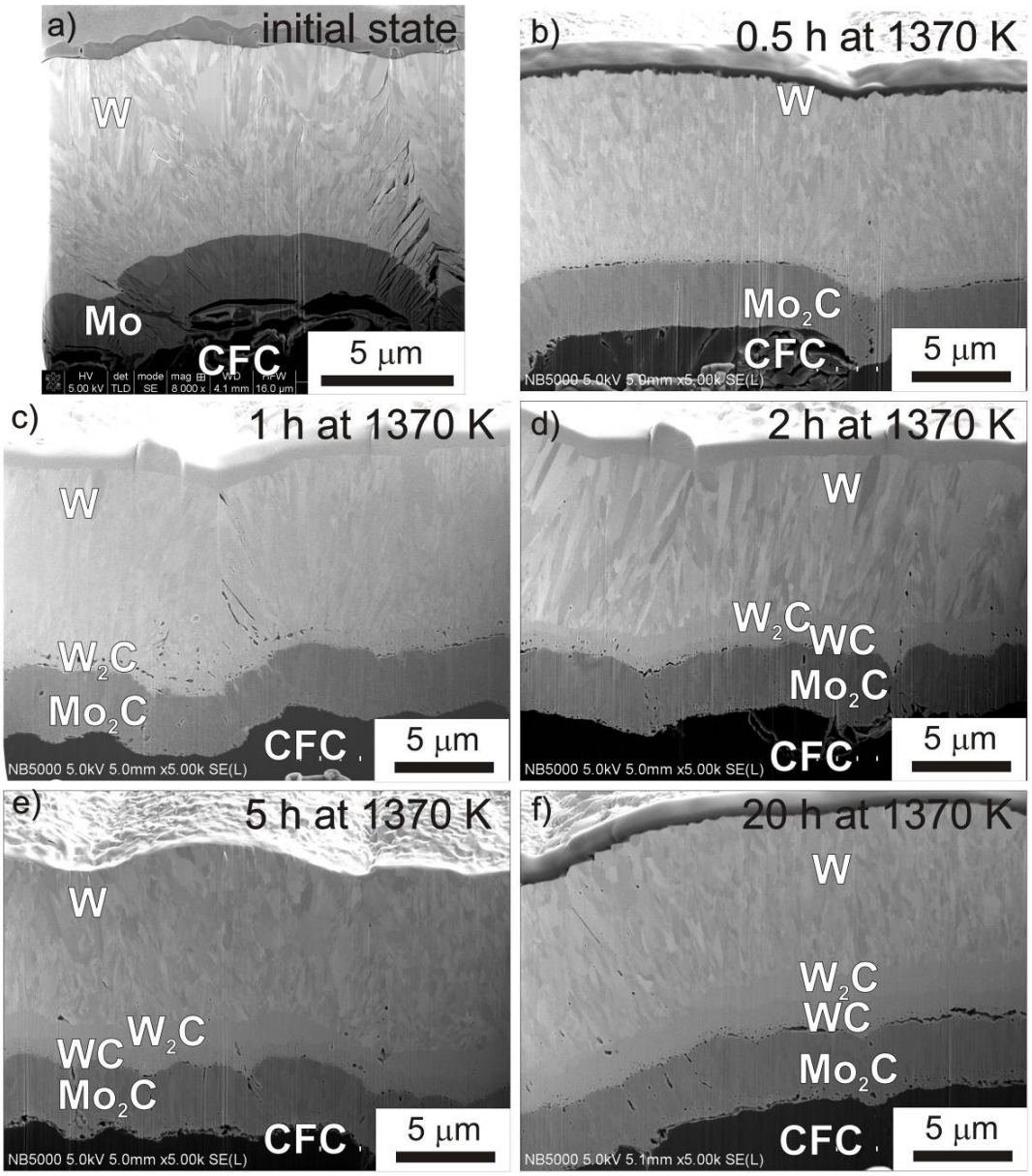

Figure 7.1. SEM cross-section image of Mo/W coatings on CFC substrate in the initial state (a) and after heat treatment at 1370 K for 0.5 h (b), 1 h (c), 2 h (d), 5 h (e) and 20 h (f)

Annealing at 1370 K for 0.5 h led to a full transformation of the initial molybdenum interlayer to Mo_2C carbide. However, this was too short a period for any carbide phase to be formed in the tungsten coating, as confirmed by the electron diffraction given in Figure 7.2.

Annealing at 1370 K for 1 h led to the formation of a continuous layer of tungsten carbide at the Mo_2C/W phase boundary - Figure 7.1c. The average thickness of the carbide layer, identified as the W_2C phase, was about 0.9 μm. There is no trace of the WC carbide phase, which appeared only after annealing for 2 h. Thickness of the total tungsten carbide (WC + W_2C) layer created after 2 h of annealing is 1.9 μm and consisted of a 0.5 μm layer of the WC phase at the Mo_2C/W_2C phase boundary and 1.4 μm of W_2C type carbide at the WC/W phase boundary, as illustrated in Figure 7.1d. Longer annealing caused the thickness of both total tungsten carbide layers to increase. After annealing for 5 h the thickness of total tungsten carbide phase is about to 2.2 μm, which was increased to 2.4 μm after annealing for 20 h. The identification of the two tungsten carbide phases was achieved using electron diffraction analysis, the results being shown in Figure 7.2. The diffraction patterns obtained for the sample annealed at 1370 K for 20 h confirm the total transformation of the initial molybdenum layer into the Mo_2C carbide phase and further carbon diffusion leading to W_2C and subsequent WC carbides formation.

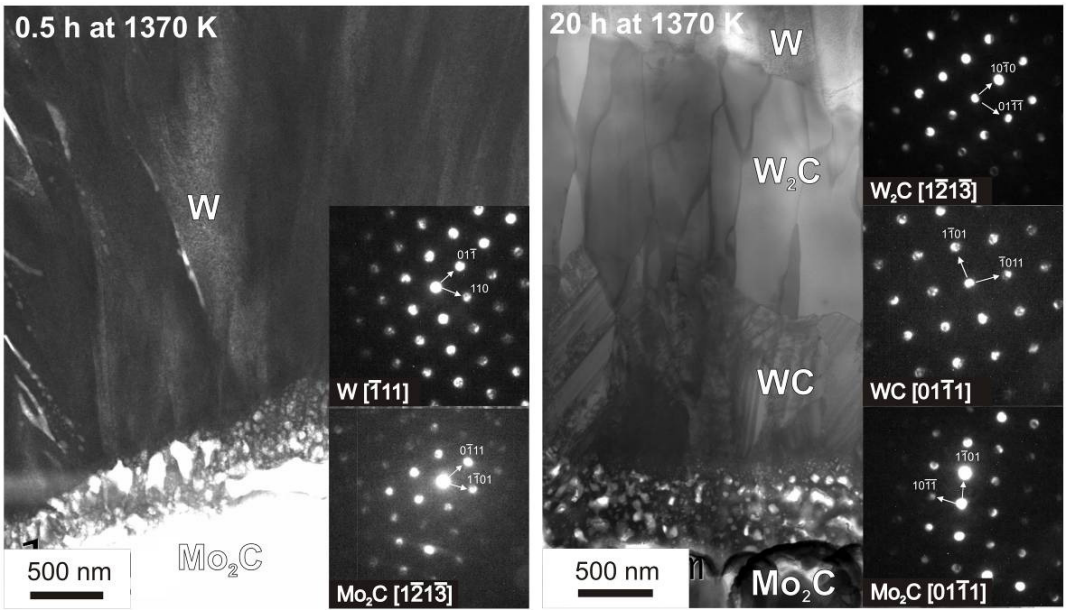

Figure 7.2. Bright field STEM images of samples annealed at 1370 K for 0.5 h and 20 h, together with the relevant electron diffraction phase analysis

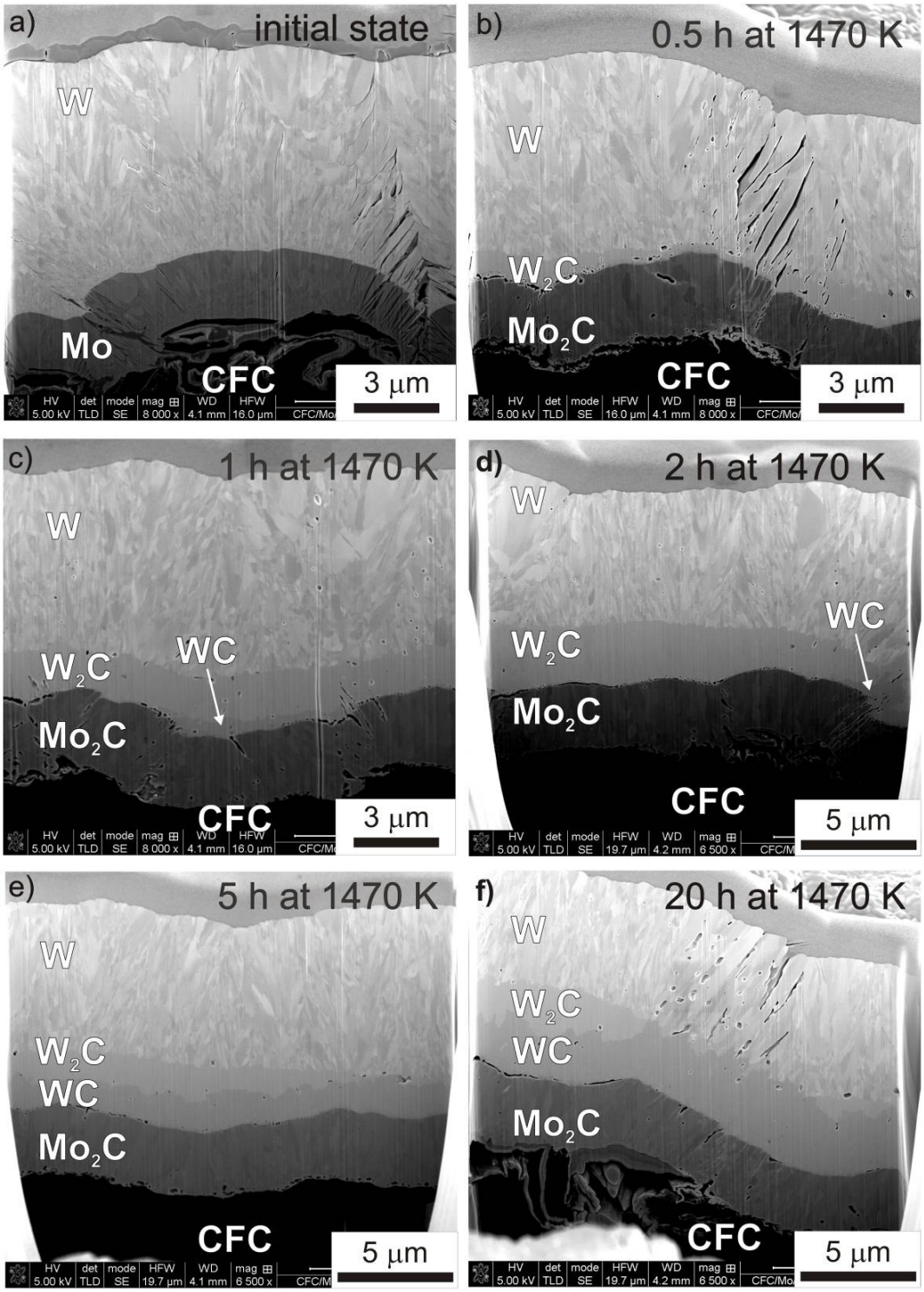

Figure 7.3. SEM cross-section image of Mo/W coatings on CFC substrate in initial state (a) and after heat treatment at 1470 K for 0.5 h (b), 1 h (c), 2 h (d), 5 h (e) and 20 h (f)

At the higher annealing temperature of 1470 K, similar processes to those shown earlier take place. Annealing for 0.5 h led to full transformation of the molybdenum layer into

Mo_2C carbide and the W_2C carbide phase was formed at the Mo_2C/W interface (Figure 7.3b). The average thickness of the W_2C layer was circa 1 μm. The Mo_2C and W_2C phases were identified by electron diffraction analysis as shown in Figure 7.4. No evidence of the WC phase was found.

Annealing at 1470 K for 1 h and 2 h resulted in an increase of the total tungsten carbide thickness (WC + W_2C) to 2.3 μm and 3.1 μm, respectively (Figure 7.3c, d). In both cases, the local presence of the WC carbide was observed at the Mo_2C/W_2C phase boundary.

Annealing for 5 h at 1470 K brought about the formation of a continuous WC carbide layer with an average thickness of 1.8 μm. The thickness of the total tungsten carbide after annealing for 5 h is almost 3.4 μm (Figure 7.3e). Annealing for 20 h led to an increase of both the WC layer and the total tungsten carbide layer to 3.3 μm and 4.4 μm, respectively. After annealing for 20 h the tungsten carbide had developed through almost 40% of the initial tungsten coating. The existence of both tungsten carbide phases – WC and W_2C was confirmed by electron diffraction analysis, for which the results are illustrated in Figure 7.4.

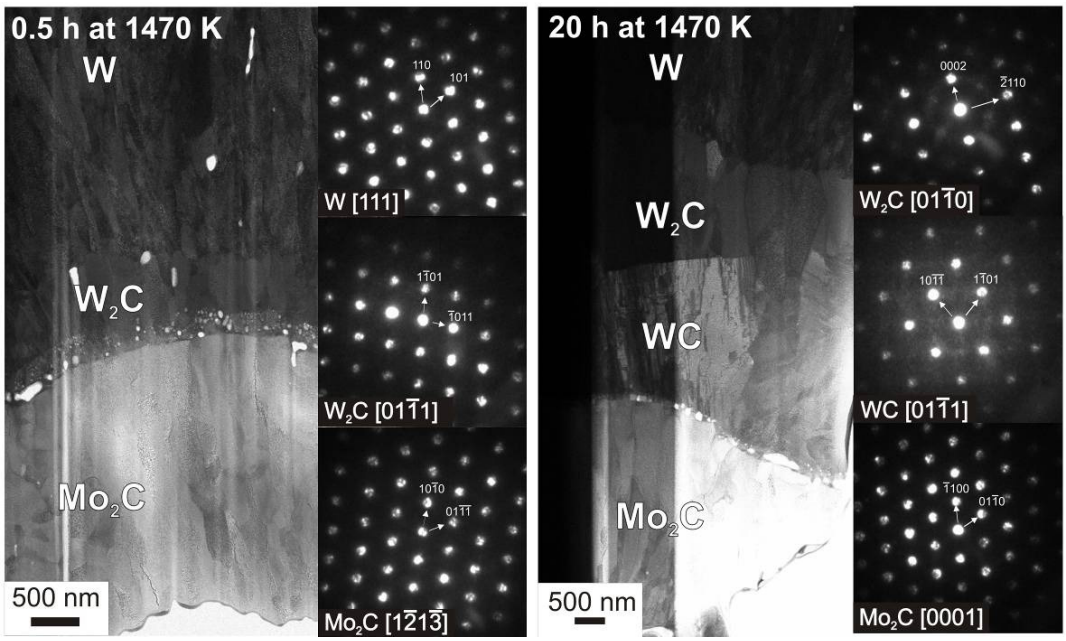

Figure 7.4. Bright field STEM images of samples annealed at 1470 K for 0.5 h and 20 h, together with the relevant electron diffraction phase analysis

Figure 7.5 shows the effect of heat treatment at 1620 K on the Mo/W coating. As anticipated annealing for 0.5 h fully transforms the Mo layer into Mo_2C and two tungsten carbide sub layers were formed at the original Mo_2C/W interface. The electron diffraction

analysis illustrated in Figure 7.6 confirms the presence of the two carbide phases – WC on the Mo_2C side and W_2C on the W side. Average thickness of WC and W_2C carbide layers are 2.3 μm and 1.5 μm, respectively.

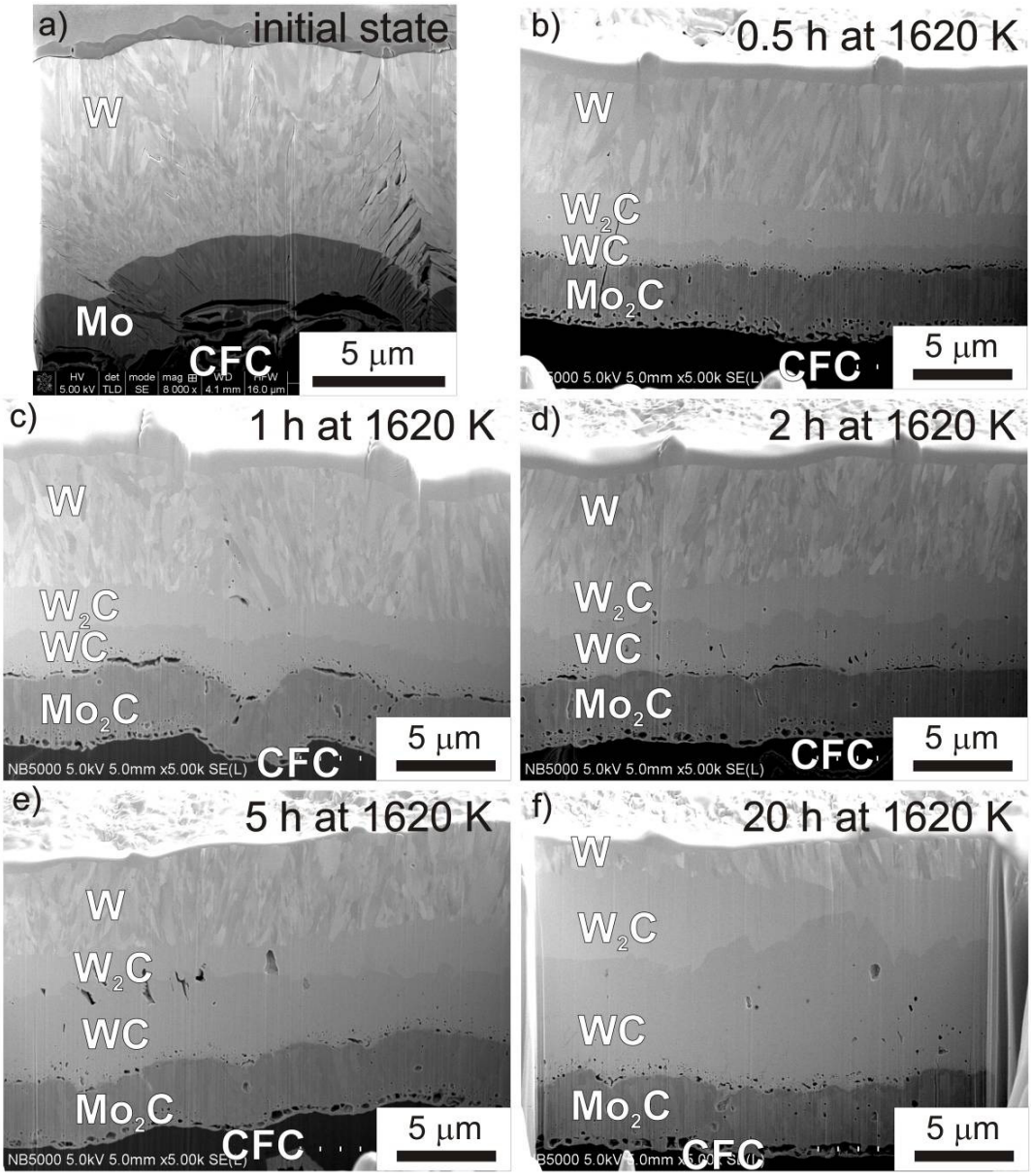

Figure 7.5. SEM cross-section image of Mo/W coatings on CFC substrate in initial state (a) and after heat treatment at 1620 K for 0.5 h (b), 1 h (c), 2 h (d), 5 h (e) and 20 h (f)

Samples subjected to annealing for 1 and 2 h have much thicker W_2C+WC layer, having a depth of 4.9 μm and 5.8 μm, respectively (see Figure 7.5c and d). An increased annealing time of 5 h caused further growth of the WC layer to 5 μm and an increase of the

total tungsten carbide layer to above 7.1 μm. Annealing at 1620 K for 20 h produces a tungsten carbide layer of total thickness above 12 μm, which is almost 90% of initial thickness of the tungsten coating (Figure 7.5f).

The electron diffraction analysis illustrated in Figure 7.6 confirmed the transformation of the entire molybdenum interlayer into Mo_2C and the presence of WC and W_2C.

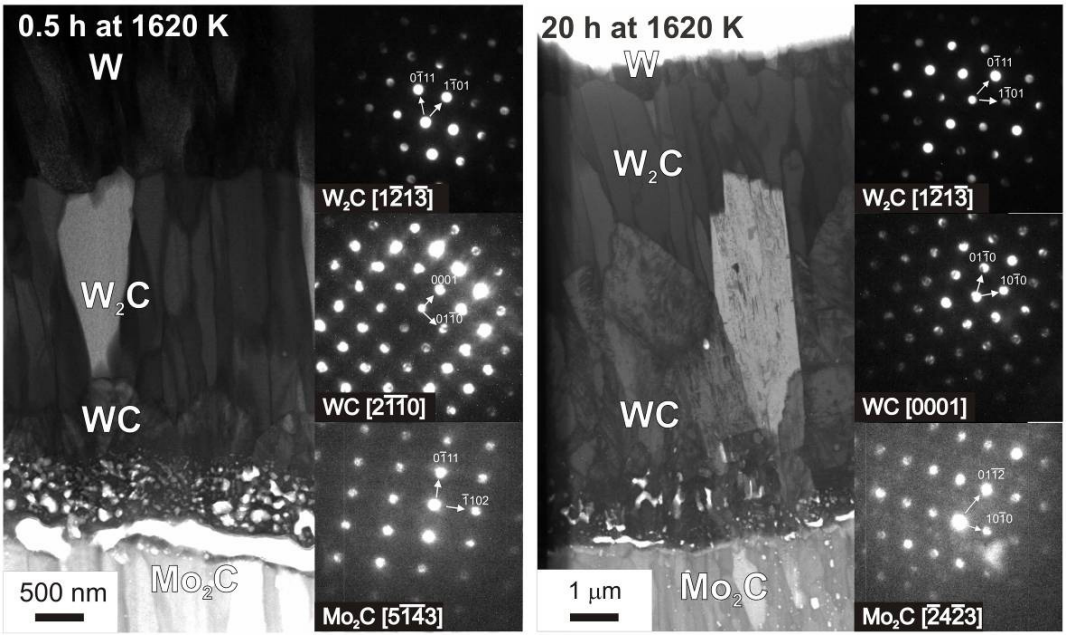

Figure 7.6. Bright field STEM images of samples annealed at 1620 K for 0.5 h and 20 h together with electron diffraction phase analysis

The results presented show that the CFC/Mo/W coating system is not stable if subjected to heating in the temperature range of 1470 – 1620 K. Carbon diffusion from the substrate initially transforms the Mo interlayer into Mo_2C and subsequently combines with the tungsten to form tungsten carbides. For short annealing times the metastable W_2C carbide phase is formed, which then transforms into the thermodynamically stable WC phase. The formation of the metastable W_2C phase precedes the formation of WC because of the lower equilibrium concentration of C, 3 wt. % compared to 6.12 wt. % for WC [109]. For longer annealing times, the increased C concentration in the W_2C causes the WC phase to form. The lower enthalpy of formation - ΔG^f makes the WC phase the thermodynamically preferable [53].

The SEM, STEM investigations and the diffraction phase analysis enabled the two forms of tungsten carbide to be identified. They are both characterized by high hardness,

extreme brittleness and very low ductility. It may therefore be assumed that their presence will cause deterioration of the thermo-mechanical properties of divertor coatings. As the growth of tungsten carbide will be the main factor influencing the service life of the coating it is essential to determine the kinetics of the growth of the tungsten carbide.

Figure 7.7 illustrates the total tungsten carbide thickness (WC + W_2C) as a function of annealing time.

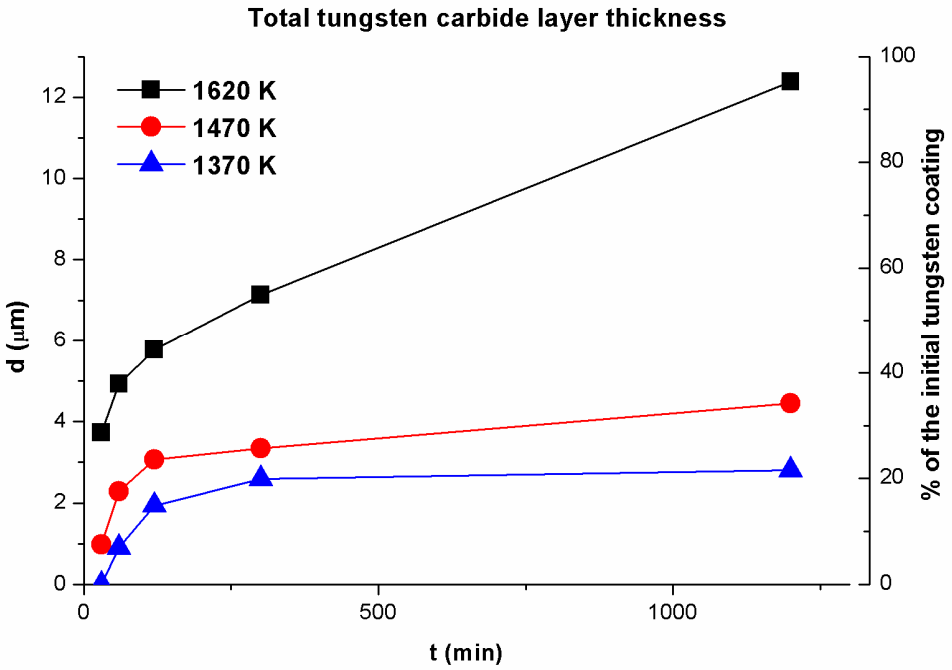

Figure 7.7. Total tungsten carbide thickness versus annealing time plotted for each temperature

At all three annealing temperatures, the total tungsten carbide layer increased in a parabolic manner, which could indicate that the process is controlled by the volume diffusion of carbon to the reaction front - the carbide/tungsten interface. It was determined that after annealing at 1370 K, the lowest temperature employed, for 20 h total of the tungsten carbide layer occupied around 20% of the initial tungsten coating thickness. Annealing for 20 h at 1470 K for 20 h led to transformation of less than 40% of the initial tungsten coating, whilst annealing at 1620 K, converted almost all the initial W coating to the carbide phases.

Based on these findings and a simple relation between the carbide phase thickness, *d*, and the annealing time, *t,* some useful information about the growth mechanism can be derived.

$$d = D \cdot t^n \tag{7.1}$$

where *D* is growth rate constant and *n* is the exponential factor.

When the exponential factor *n* is close to 1, the process is controlled by the reaction rate. It means that the diffusion occurs much more rapidly than the reaction itself, and the quantity of reaction ingredients needed for the reaction to continue are constantly supplied. If the growth rate is controlled by the volume diffusion, the factor *n* is close to 0.5 [110][111]. In such a case, the diffusion, proceeds more slowly than the reaction itself and the limiting factor is the rate at which the reaction ingredient is supplied. In the case of total carbides layer formation, the value of the exponential factor n is close to 0.4 for each annealing temperature annealing. This value of *n* indicates that volume diffusion is the predominant factor determining the growth kinetics.

Two stages of the growth of the total carbide thickness can be identified in Figure 7.7. A short initial period, during which promoted total tungsten carbide is visible, and a slower long term growth period can be seen. The transition between the short and long term period appears at a different time for each temperature. In the case of the lowest temperature, 1370 K, the transition occurs after 5 h, whereas for annealing at 1470 K and 1620 K the transition occurs after 2 h and 1 h, respectively. For all cases, based on the data for the thickness of the carbide layer illustrated in Figure 7.7 the growth rate constant D (m^2/s) has been determined and the Arrhenius plot illustrated in Figure 7.8 was created. The Arrhenius plot enabled to the activation energy for each period to be determined.

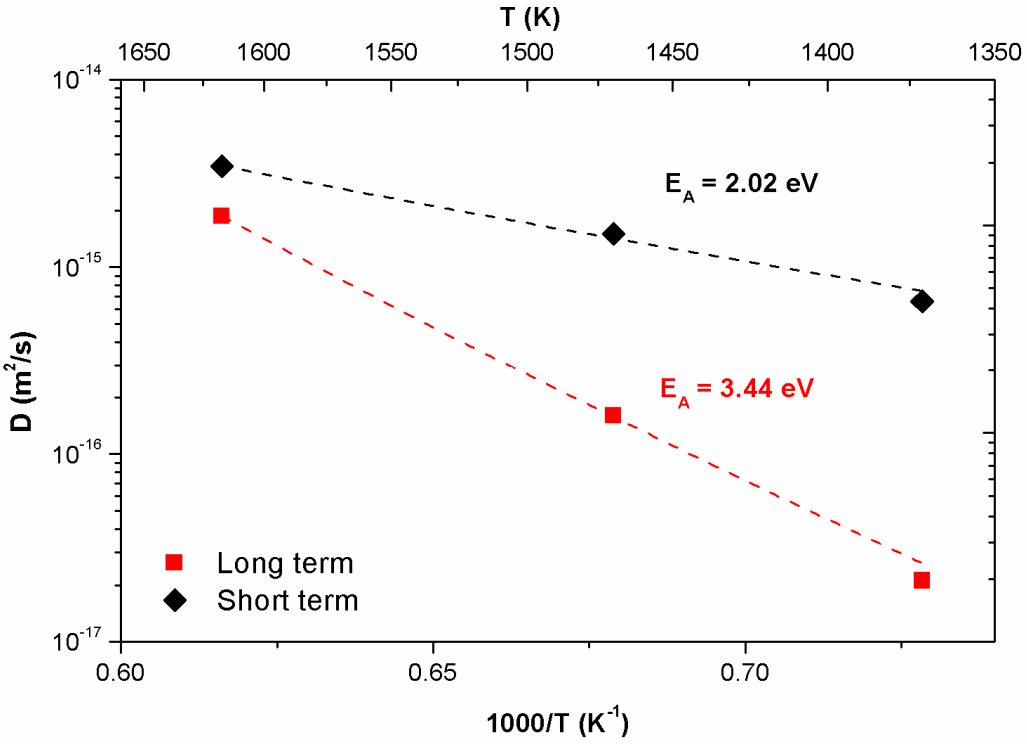

Figure 7.8. Arrhenius plot for carbon diffusion

The total tungsten carbide growth in the short term is characterized by a relatively low activation energy – 2.02 eV (195 kJ/mol). Such a low value of the activation energy in the early stage of tungsten carbide formation was unexpected and has not been reported in literature. There is still no full explanation for this phenomenon. One of the reasons for such a low activation energy could be the structure of the tungsten coating at the boundary with the molybdenum layer, as a result of process used to deposit the coating. The early stage of the deposition process might result in the formation of specific structure at the bottom of the coating, which promotes the carbon diffusion and thereby enhances the growth of the total tungsten carbide layer.

During the long term growth, the determined activation energy was about 3.44 eV (332 kJ/mol), which is in good agreement with data in the literature [54]. Figure 7.9 shows the comparison of the obtained long term growth rate of total tungsten carbide layer with the data given in the literature.

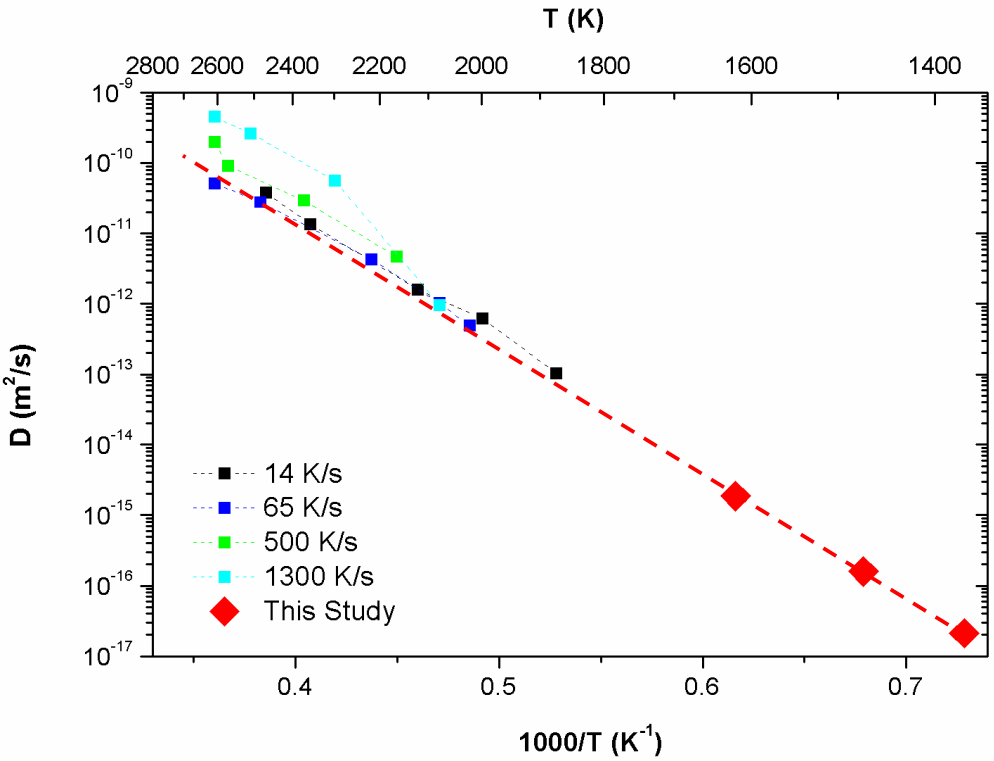

Figure 7.9. Comparison of obtained Arrhenius plot for carbon with literature data [54]

The reaction rate of tungsten carbide layer growth (D (m^2/s)) for different heating rates (from 14 K/s to 1300 K/s) is shown. In all cases, there is a very good agreement with the

results obtained in this research. Additionally, it was noted that carbon diffusion to the reaction interface is independent of the heating rate.

The determined data of the activation energies was verified by reproduction of the carbide thickness data using the Arrhenius equation (equation 7.2). This equation describes the dependence of the annealing temperature (T) and determined activation energies (E_A) for both long and short term of carbide growth on the rate of diffusion.

$$d = d_0 \exp(-E_A / RT) \tag{7.2}$$

where: d_0 – pre-exponential factor (m^2/s) and R – gas constant

In the recalculation, both the short and long term activation energies were used. For the calculation of the carbide thickness in the initial phase the short term activation energy was applied. The determined carbide growth rate, *d,* multiplied by the annealing time gave the produced thickness. To calculate the thickness of the carbide layer in the long term, the long term activation energy was used. The determined carbide growth rate for each temperature, multiplied by the time, t_l, the difference between the total annealing time and the short term period, gave the thickness produced in the long term The total thickness is the sum of the short term thickness and long term thickness.

Results for the data validation are presented in Figure 7.10, where a comparison between the measured total tungsten carbide thickness, the solid lines, and produced thickness data, dashed lines, are shown.

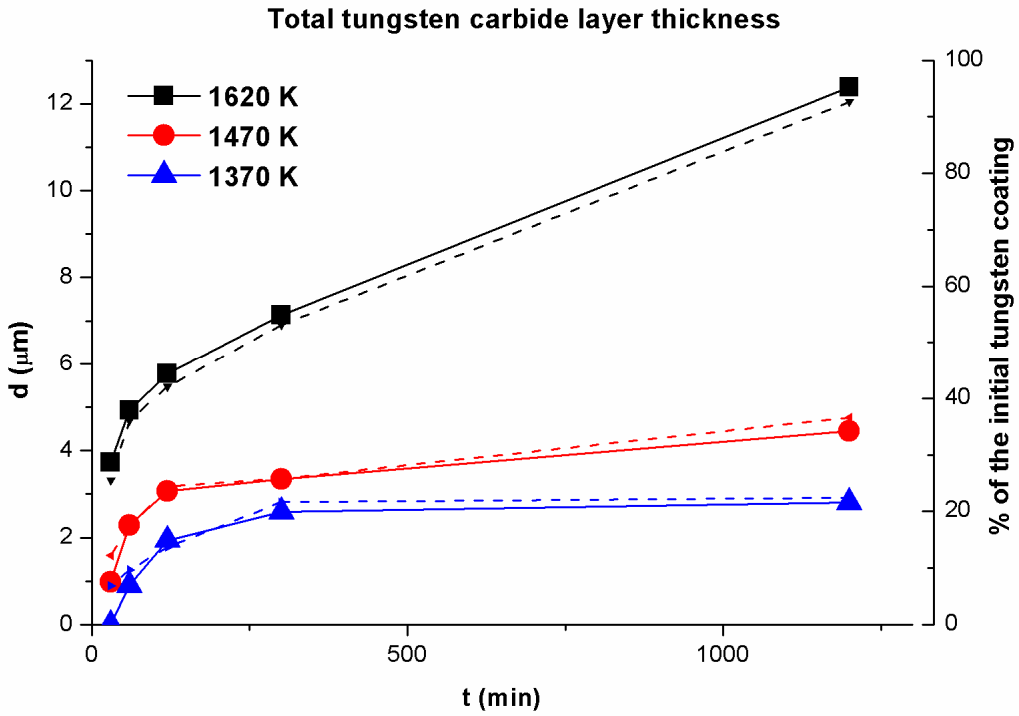

Figure 7.10. Total tungsten carbide thickness versus annealing time plotted for each temperature (solid lines) together with reproduced data based on obtained activation energies (dashed lines)

The very good agreement between the measured and reproduced data for each temperature should be noted. The good agreement with the measured data is considered to be promising considering the possibility of estimating the growth of the carbide layer when components are subjected to heating at different temperatures for various periods of time.

To determine the influence of tungsten carbides on the mechanical properties of CFC/Mo/W systems, the micro-scratch test was performed. Figure 7.11 illustrates the relationship between measured carbide's thickness and the critical force to cause failure of the coating.

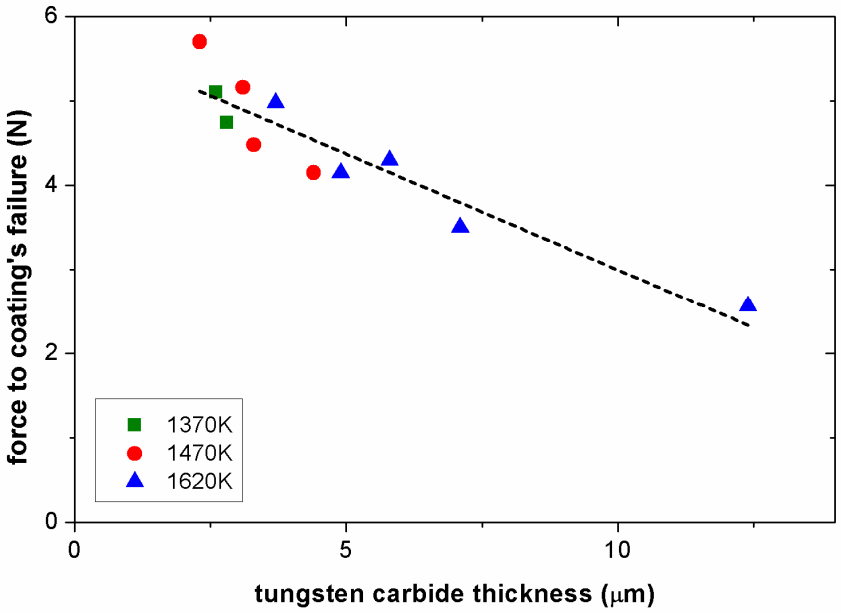

Figure 7.11 Total tungsten carbide thickness versus force to coatings failure in a micro-scratch test plotted with indication of every annealing temperature

For the samples with a tungsten carbide layer below 2 μm no coating delamination was observed, even at the maximum applied force of 6 N. However, on cross-section images, some cracks were visible but they did not cause any detachment of the coating form the CFC substrate. When the thickness of the carbide layer was above 2 μm, the coatings were locally detached from the CFC substrate. For example, on coatings with a carbide layer thickness of 2.3 μm, (1 h at 1470 K), and 2.6 μm (5 h at 1370 K) local delamination occurred at a force of 5.7 and 5.1 N, respectively. The critical force to cause failure of the coatings decreased to 4.1 N for a carbide layer thickness of 4.4 μm (20 h at 1470 K), and 4.9 μm (1 h at 1620 K). Further increase in the thickness of the carbide phase to 7.1 μm (5 h at 1620 K) and 12.4 μm (20 h at 1620 K), resulted in a further decrease of the critical force to cause coating failure to 3.5 N and 2.5 N, respectively.

More information about the mechanism of coatings degradation during the scratch-test can be obtained from Figure 7.12, where SEM images of the cross-sections of the Mo/W coatings on CFC substrates after annealing at different temperatures are shown. In each image the annealing conditions, the critical force to cause coating failure and the total tungsten carbide thickness are given.

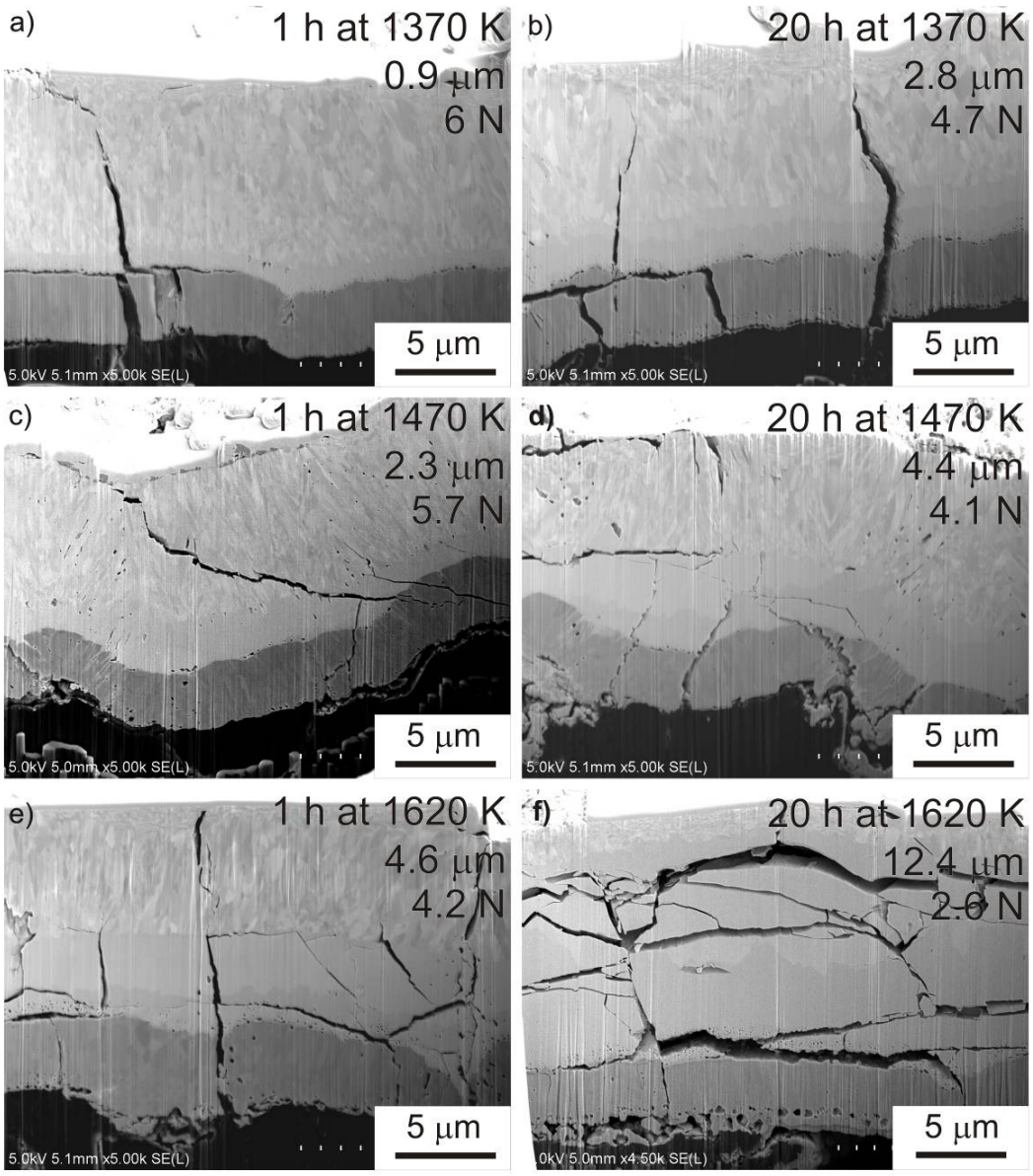

Figure 7.12 SEM cross-section image of Mo/W coatings on CFC substrate after the micro-scratch test, near the failure area. Inside each image annealing conditions, the critical force to coatings failure and total tungsten carbide thickness are provided.

In the case of samples where no delamination was observed, some cracks perpendicular to the surface can be seen in the coating. Pronounced cracking inside the carbide layer was observed in the samples with a total carbide thickness above 2 μm, which was greater in the samples annealed for longer periods or at a higher temperature. The thicker the carbide layer the greater degree cracking and the lower the critical force required to cause failure of the coating. The strong influence of annealing time and, therefore, the formation of the tungsten carbide layer on the coating's mechanical properties was confirmed.

It should be noted that the results obtained in the current research had a direct influence on the operational conditions of the JET fusion device. The operational temperature of the divertor element installed in the JET has been limited to 1470 K. The working temperature originally planned for the device was too high in the light of the rate of carbon diffusion and the consequent growth of the tungsten carbide. The intensified carbide growth rate could lead, together with the expected thermal shocks, to cracking of the coating and eventually to delamination, which would seriously affect the working conditions of the device.

7.2 The formation of re-deposited layers on a divertor

7.2.1 Model system – W doped amorphous C films

To gain an understanding of the formation conditions of a re-deposited layer during a fusion reactor operation, a set of tungsten doped carbon films were analyzed. The influence of the concentration of tungsten dopant and the annealing temperature on the sample's structural morphology and phase composition were investigated.

Amorphous carbon film doped with 9 at. % tungsten

Initially some general information about the phase composition of the film was obtained by XRD analysis. Figure 7.13 presents the XRD data of five samples containing 9 at. % of tungsten after annealing at various temperatures - 1450 K, 1800 K, 2200 K, 2500 K and 2800 K for one hour.

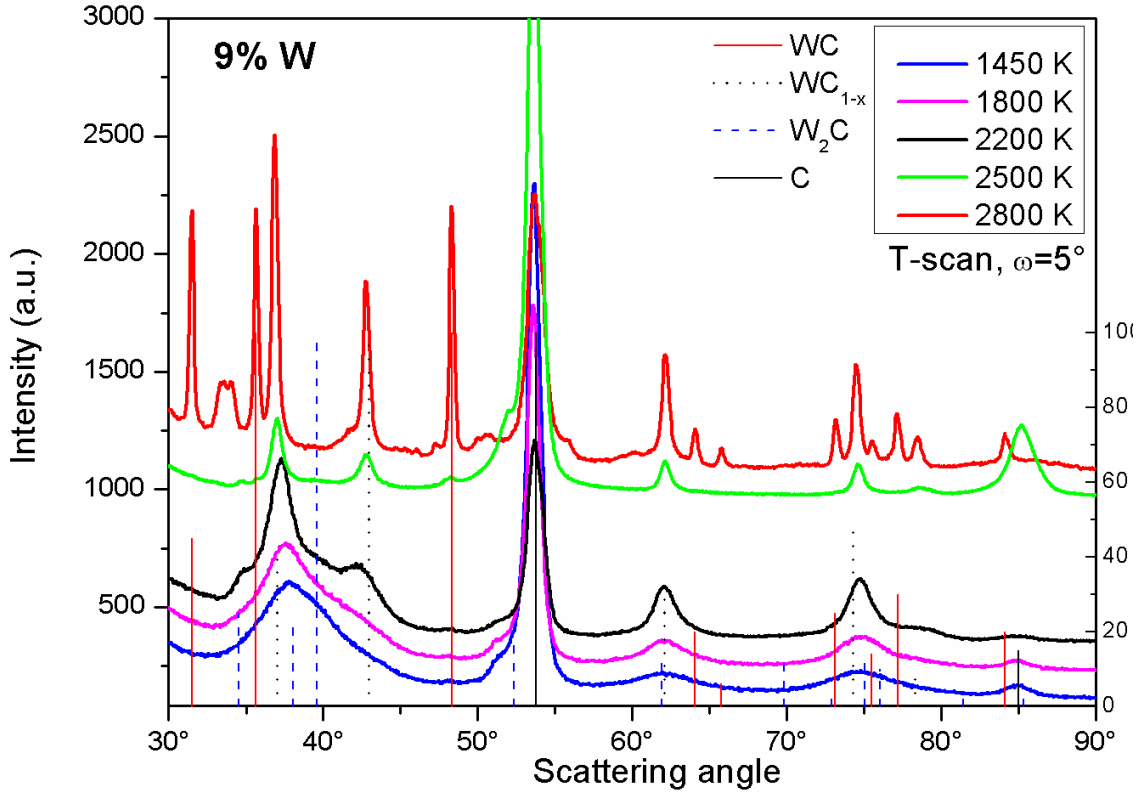

Figure 7.13. X-ray spectra of 9 at. % W doped films after annealing at different temperatures for one hour. Diffraction peaks for the carbide phases WC, W_2C, WC_{1-x} (PDF card 25-1047, 35-776, 20-1316) and for pure graphite (substrate) are indicated [107]

For the lower annealing temperatures – 1450 K and 1800 K - the XRD spectrum is characterized by broad diffraction peaks around 37°, 63° and 75°. They may be attributed to different phases - W_2C, WC_{1-x} and WC carbide crystallites, or to mixtures of the carbides. The presence of WC carbide phase, however, is considered unlikely since no diffraction peak was observed around 48°. Nevertheless, unequivocal phase identification is not possible. Additionally, the presence of such broad peaks indicates the existence of very small crystallites, most likely possessing a size of only a few nanometers.

After annealing at 2200 K the diffraction peaks become somewhat sharper compared to the peaks generated by annealing at the lower temperatures. Peaks, which starts to appear around 37° and 43° might indicate the presence of the WC_{1-x} carbide phase. However, the peak at 43° is shifted to the left and the peak around 75° is shifted to the right which may be the result of a small fraction of W_2C carbide being present.

Distinct peaks for WC_{1-x} phase appears at 37°, 43°, 62° and 74° for the sample annealed at 2500 K. Additionally, the left shoulder of the peak at 54° corresponding to graphite substrate might indicate the presence of W_2C carbide phase. WC phase does not exist in this sample, as no peak coming from that phase could be found.

For the sample annealed at the highest temperature of 2800 K the diffraction peaks are very sharp indicating an increase of the crystallite sizes compared to those occurring at the lower annealing temperatures. Clear evidence of the WC carbide is indicated by the diffraction peaks at 32°, 36°, 48°, 64°, 66°, 73°, 76°, 78° and 84°. The presence of the WC_{1-x} phase can be recognised by the clear diffraction peaks at 34°, 43° and 74°. Additionally, the peak at 33°, visible only in the sample annealed at 2800 K, corresponds to tungsten oxide WO_3.

More information about type, size and distribution of the carbide crystallites formed after annealing was provided by electron microscopy and nano-diffraction. The structure of the film doped with 9 at. % W and annealed at 1450 K is very homogenous as shown in Figure 7.14a and b. The high resolution images, Figure 7.14c and d reveal a structure of fine carbide crystallites with and average size of less than 5 nm. The crystallite size observed is in agreement with the broad diffraction peaks revealed in the XRD data. 17 of the 23 analysed diffraction patterns taken from individual particles confirmed the presence of cubic WC_{1-x} and 6 indicated hexagonal W_2C. Detailed information about the amount of identified tungsten carbide phase the samples is summarized in Table 7.1. Example diffractograms of each phase are given in Figure 7.14e and f. Based on these results, the cause of the broad XRD peaks can be now identified as the existence of a mixture of nanometer scale WC_{1-x} and W_2C crystallites. No trace of WC carbide phase was identified, which was confirmed by the XRD analysis.

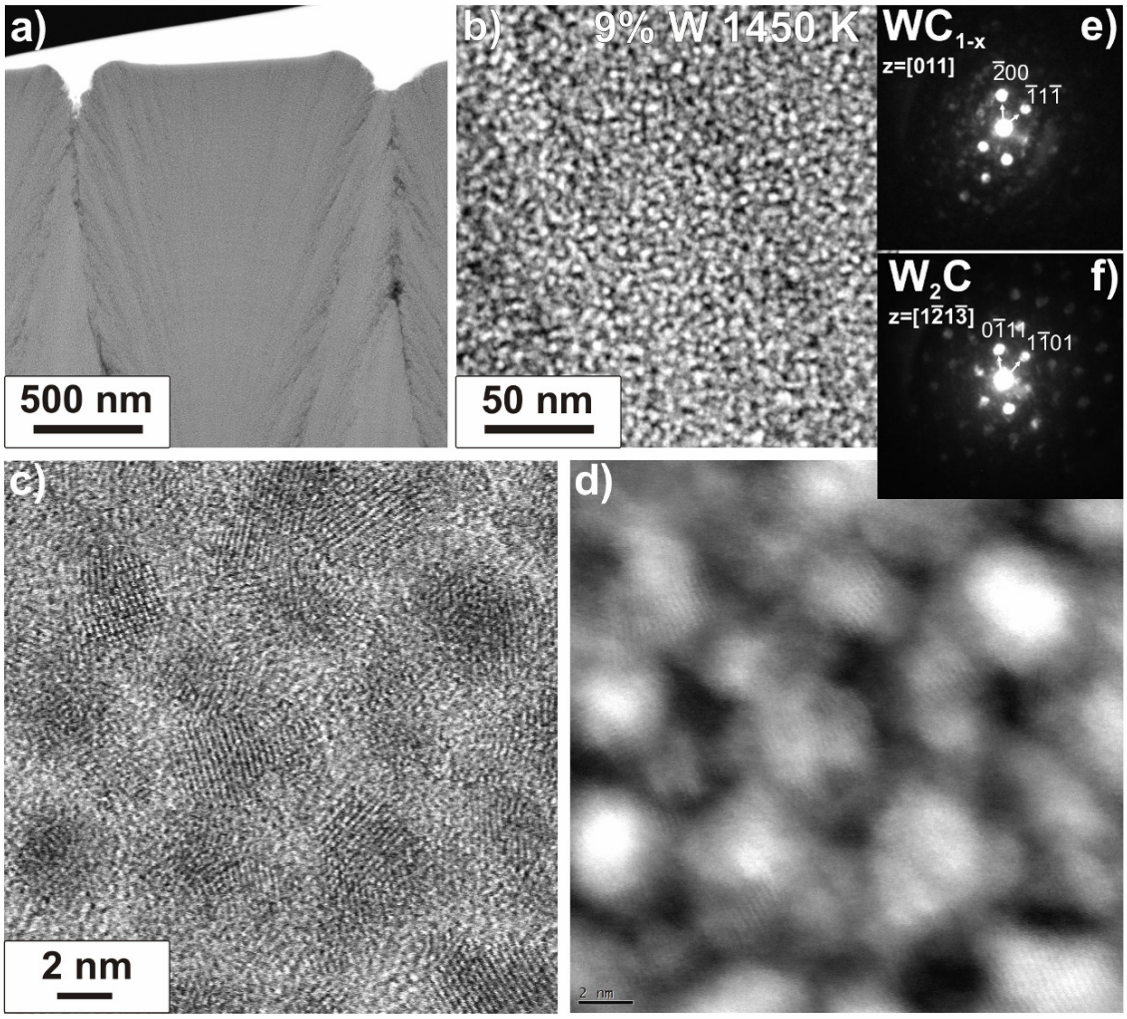

Figure 7.14. STEM images in Z-contrast (a, b, d) and in BF mode (c) together with typical electron diffractograms of WC_{1-x} (e) and W_2C (f) of 9% W film annealed at 1450 K

STEM observations show that the annealing of the 9 at. % W doped film at 2200 K led to the formation of a fine, homogeneous carbide structure, as illustrated in Figure 7.15a and b. The carbides, however ale slightly larger than those which occurred in the sample annealed at 1450 K. The average particle size was 6 ± 2 nm. Phase identification performed by a nano-diffraction technique reveal a similar carbide composition as that in the film annealed at the lower temperature. The predominant phase was WC_{1-x} carbide with the presence of some W_2C carbides. As in the sample annealed at 1450 K, the thermodynamically stable WC phase was not detected.

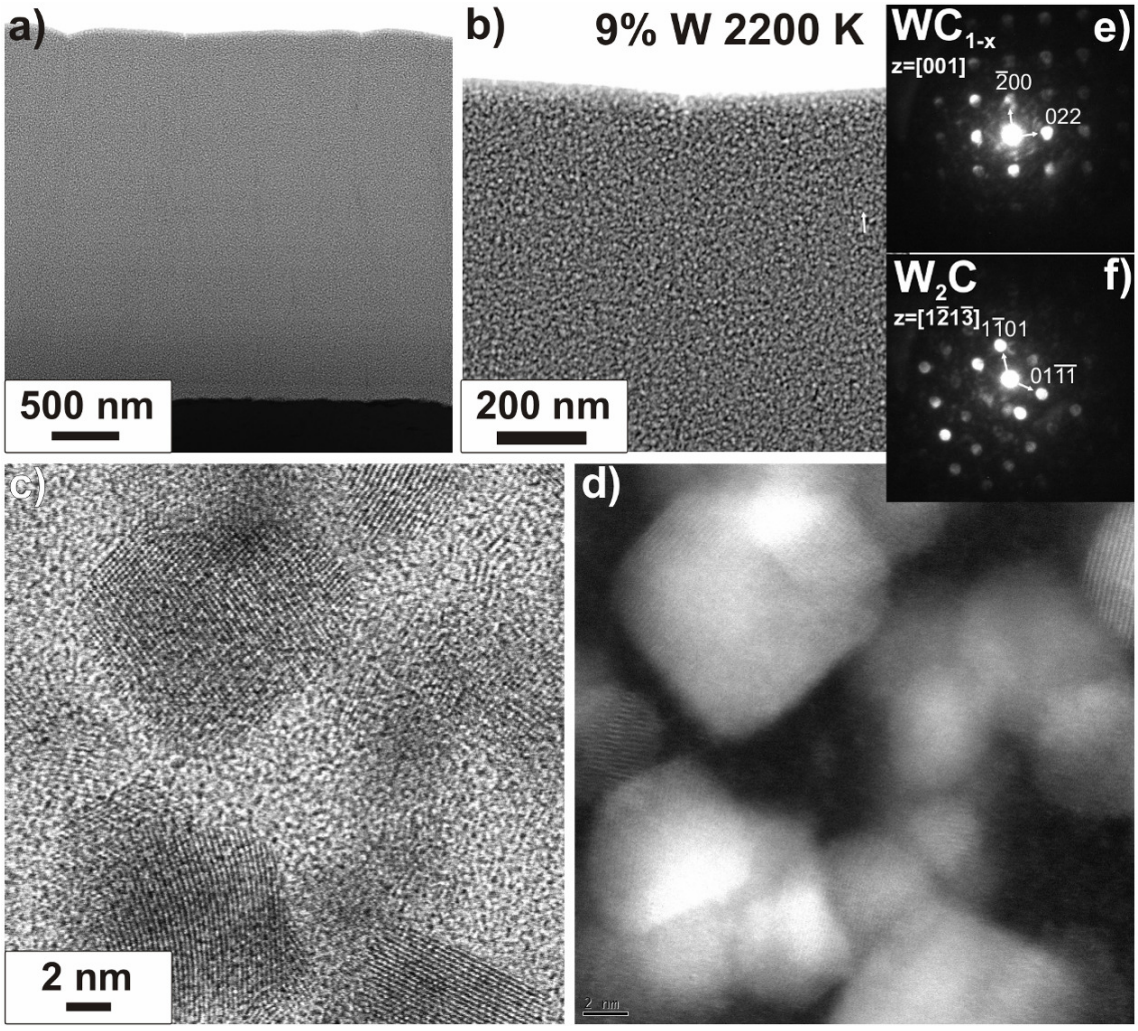

Figure 7.15 STEM images in Z-contrast (a, b, d) and in BF mode (c) together with typical electron diffractograms of WC_{1-x} (e) and W_2C (f) of 9% W film annealed at 2200 K

Figure 7.16a and b show the morphology of the sample doped with 9% W annealed at 2500 K. The carbide arrangement is homogeneous and the crystallite size, 13 ± 5 nm, is larger than that observed in the samples subjected to lower annealing temperature. The composition of the phase, however, was not significantly changed compared to that formed at the lower annealing temperature. There are two carbide phases present WC_{1-x} and W_2C with cubic with the WC_{1-x} being predominant. No diffraction peaks arising from the WC phase were detected.

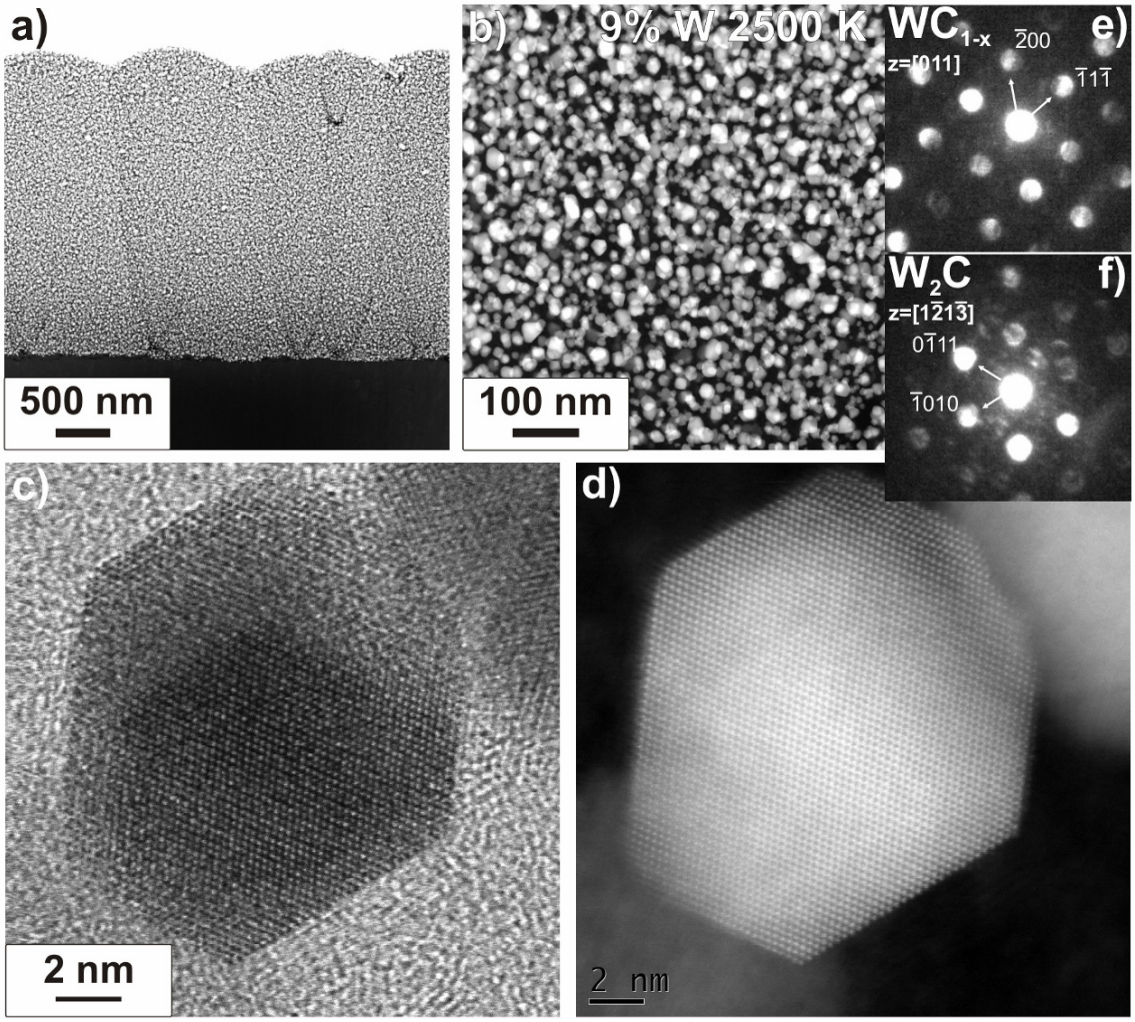

Figure 7.16. STEM images in Z-contrast (a, b, d) and in BF mode (c) together with typical electron diffractograms of WC_{1-x} (e) and W_2C (f) of 9% W film annealed at 2500 K

Significant structural transformation was observed in the sample annealed at 2800 K. As presented in Figure 7.17, a diversity of the size of the carbide can be observed. In addition to the carbides of size 33 ± 22 nm, a small number of larger carbide particles, with a size greater than 300 nm, were detected. Nano-diffraction analysis revealed that more than half of those analysed were WC_{1-x}. W_2C carbides were no longer present and hexagonal WC carbides had been formed. This is consistent with the XRD data, where relatively large WC diffraction peaks appear. Large carbides particles with a size of 350 ± 190 nm were identified as exclusively WC, see the right side of Figure 7.17a and b. However, WC carbides was also present in the form of small crystallites.

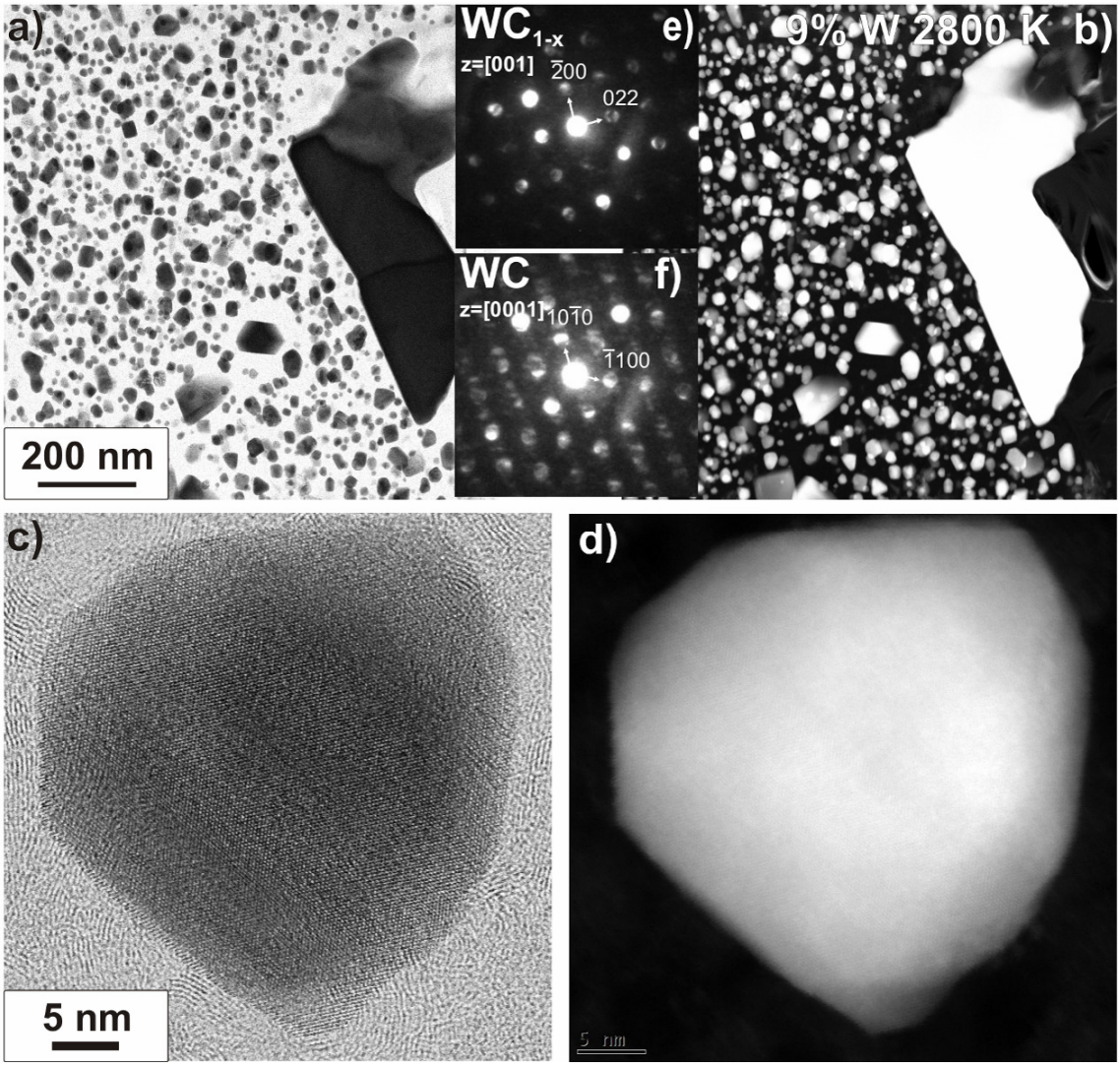

Figure 7.17. STEM images in BF mode (a, c) and in Z-contrast (b, d) together with typical electron diffractograms of WC_{1-x} (e) and WC (f) of 9% W film annealed at 2800 K

Amorphous carbon film doped with 18 at. % tungsten

The sample doped with 18% W and annealed at 1450 K exhibited much sharper diffraction peaks than were recorded by the sample with 9% W. Part of these peaks can be attributed to specific phases, but some part of the spectrum is equivocal. In the range from 30° to 50° identification of WC and W_2C or WC_{1-x} phases is possible. Nevertheless, the cause of the peaks around 63° and in the range 70-80° remain uncertain.

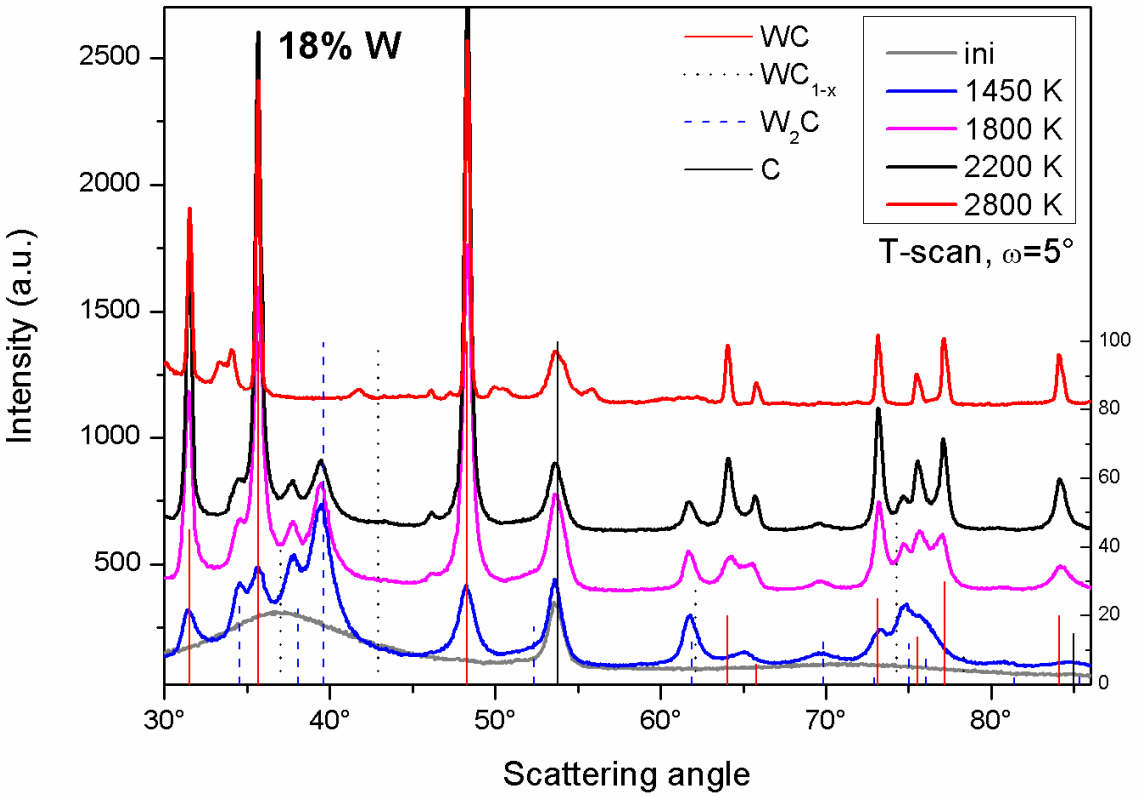

Figure 7.18. X-ray spectra of 18 at. % W doped films in as deposited state and after annealing at different temperatures for one hour. Diffraction peaks for the carbide phases WC, W_2C, WC_{1-x} (PDF card 25-1047, 35-776, 20-1316) and for pure graphite (substrate) are indicated [107]

The hhigher annealing temperature of 1800 K led to pronounced WC phase peaks, clearly visible around 65° and 75°. The peaks from W_2C or WC_{1-x} phases are still visible, but their intensity appeared to be reduced. Further reduction of the W_2C/WC_{1-x} peaks was evident after annealing at 2200 K. The diffraction peaks coming from the WC phase are more pronounced and much sharper. This is indicative of an increase in the amount of the carbide phase and larger sizes of the crystallites. However the most reliable conclusions can be made by considering the sample with 18% W annealed at 2800 K. Very narrow peaks on the XRD spectrum can be readily attributed to the formation of relatively large particles of the WC type

carbide. No other carbide phase could be identified, but tungsten oxide phase WO_3 was identified at 33°.

Carbide structure in the film doped with 18% W and annealed at 1450 K is shown in Figure 7.19a and b. The carbide particles are larger and more densely arranged compared to those in the 9% W film annealed at the same temperature. The calculated crystallite size averaged 9 ± 3 nm. At 1450 K all three types of carbides – WC_{1-x}, W_2C and WC – were present with the hexagonal W_2C being dominant. Of the 28 carbide particles analysed only 3 were identified as WC and 7 as WC_{1-x}. The predominant occurrence of the W_2C phase would appear to be consistent with the XRD data. The diffraction peaks at 37° and 40° arising from W_2C phase were the strongest.

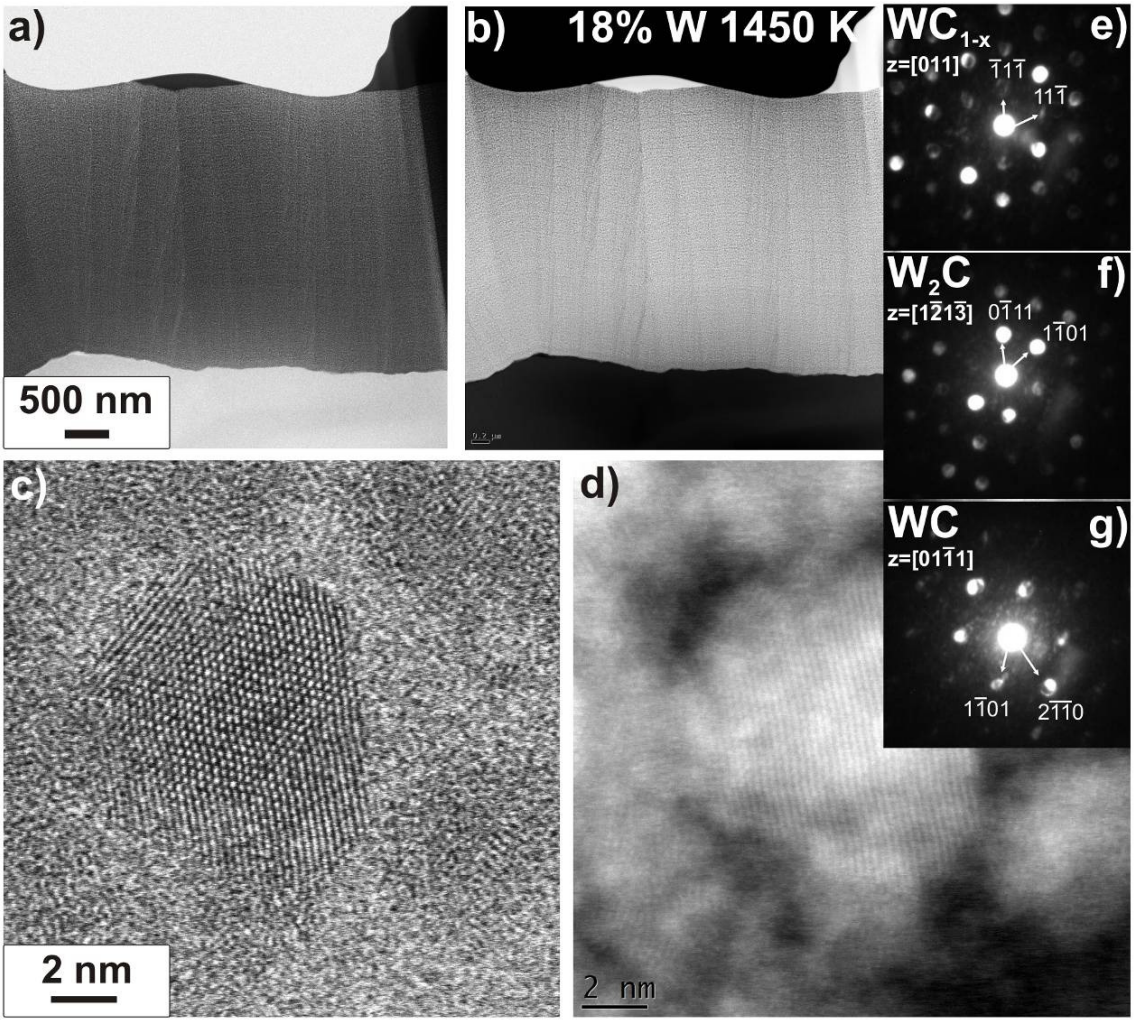

Figure 7.19. STEM images in BF mode (a, c) and in Z-contrast (b, d) together with typical electron diffractograms of WC_{1-x} (e), W_2C (f) and WC (g) of 18% W film annealed at 1450 K

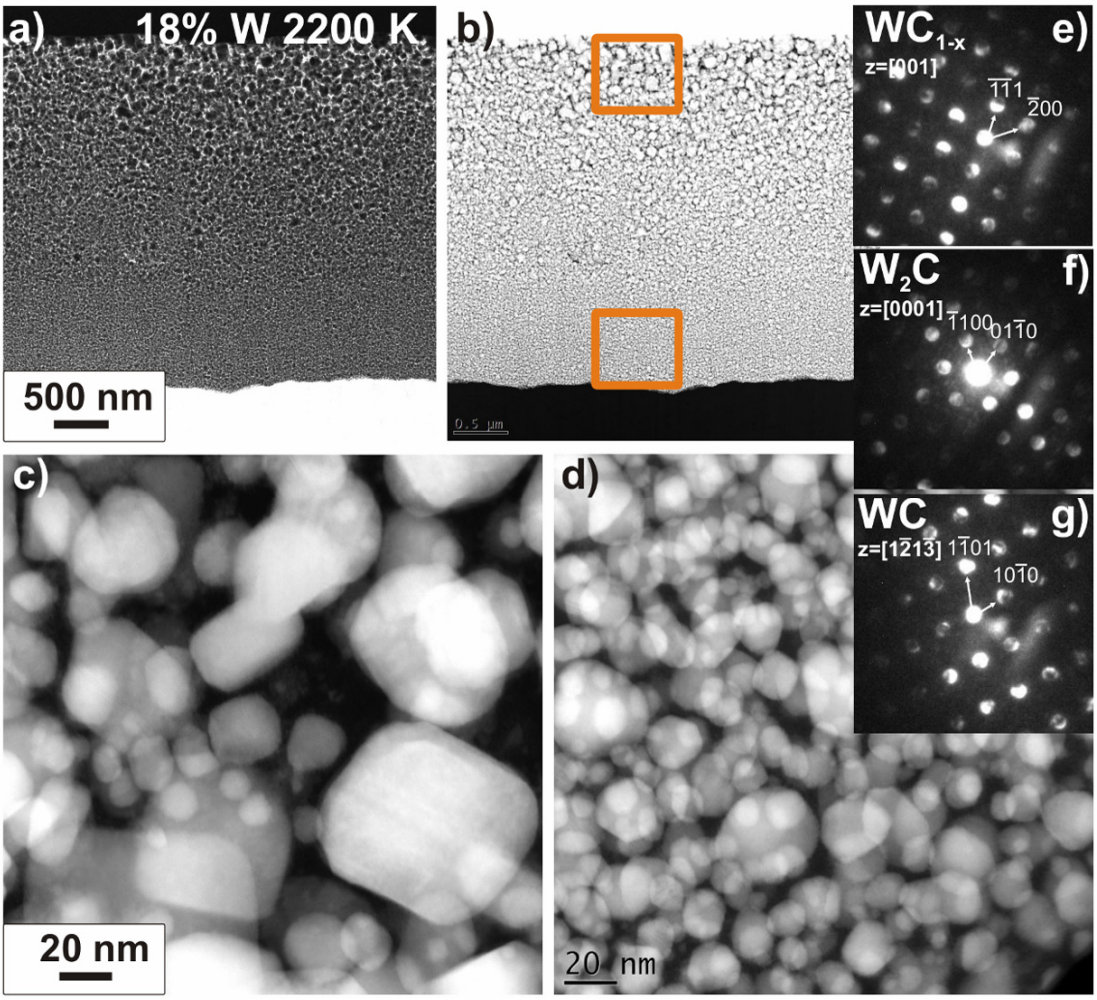

Figure 7.20. STEM images in BF mode (a, c) and in Z-contrast (b, d) together with typical electron diffractograms of WC_{1-x} (e), W_2C (f) and WC (g) of 18% W film annealed at 2200 K

In the sample annealed at 2200 K the size distribution of carbides particles was no longer homogeneous across the film, as illustrated in Figure 7.20a and b. At the bottom of the layer there were carbide particles with an average size of 12 ± 6 nm, but the particle size steadily increased towards the surface. Larger particles of size 22 ± 15 nm were present at the outer part (Figure 7.20d). The reason for the carbide size diversity could be related to the sample having a non-homogeneous composition rather that the effect of annealing temperature. According to RBS investigation the tungsten addition was not uniform and varied along the film thickness from 14% to 18% at the surface of the layer. The appropriate 18% of tungsten annealed at 2200 K sample is therefore only at the top surface of the film. The non uniform tungsten concentration was observed only in this sample. All other samples exhibited uniform tungsten concentration throughout the film thickness.

The tungsten carbide phases at the top and bottom part of the layer are different. At the top, where the tungsten concentration is close to 18%, all three phases are present with hexagonal WC carbide being predominant. Of the 24 particles analysed there are only 4 of W_2C and 4 of WC_{1-x}. At the bottom of the layer, where the initial tungsten concentration was close to 14%, the W_2C and WC_{1-x} phases were predominant. The number of W_2C and WC_{1-x} particles were similar. Minor trace of hexagonal WC phase were detected.

Annealing the sample with 18% W at a temperature of 2800 K led to the formation of some large carbide particles with an average size of 568 ± 356 nm, however, other particles with a size below 100 nm were present. The XRD phase identification revealed only the hexagonal WC phase. The undertaken nano-diffraction analysis, shown in Figure 7.21e, confirms that only the WC phase was present. In addition oxidation of carbide particles protruding from the surface was observed. An example of an oxidized tungsten particle is in the BF mode and Z contrast is shown in the circles in Figure 7.21a and b.

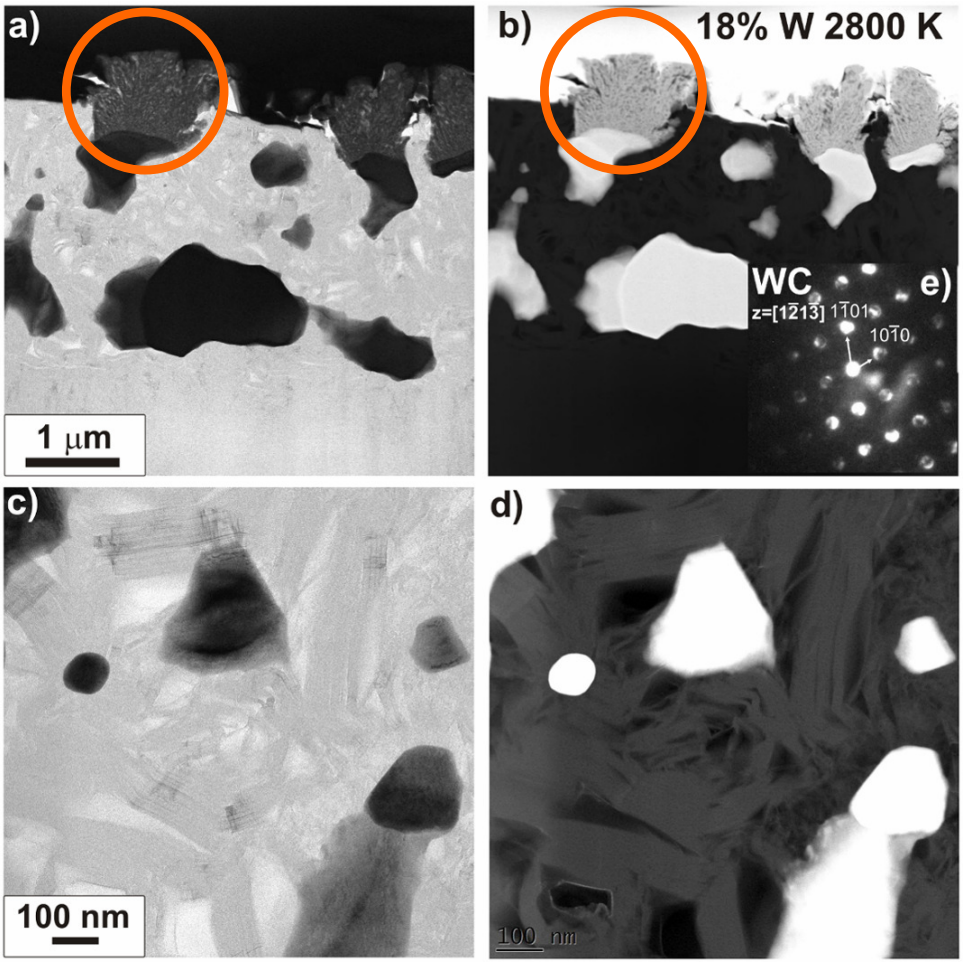

Figure 7.21. STEM images in BF mode (a, c) and in Z-contrast (b, d) together with typical electron diffractograms of WC (e) of 18% W film annealed at 2800 K

Amorphous carbon film doped with 22 at. % tungsten

Figure 7.22 illustrates the XRD data for the samples with 22% tungsten. After annealing at a temperature of 1100 K it was not possible to identify any particular phase, however, the very broad peaks around 37°, 63° and 74° indicate the presence of fine, nanometric sized crystallites. Firm conclusions were possible with regard to the to samples annealed at 1450 K and 1800 K. In both cases relatively narrow peaks of WC phase are visible. The crystallites size increased with the higher annealing temperature, as indicated by narrowing of the diffraction peaks, which are clearly evident at around 64° and 75°. It is apparent that the only the WC phase is formed in the sample as diffraction peaks which could be attributed to other phases are not present.

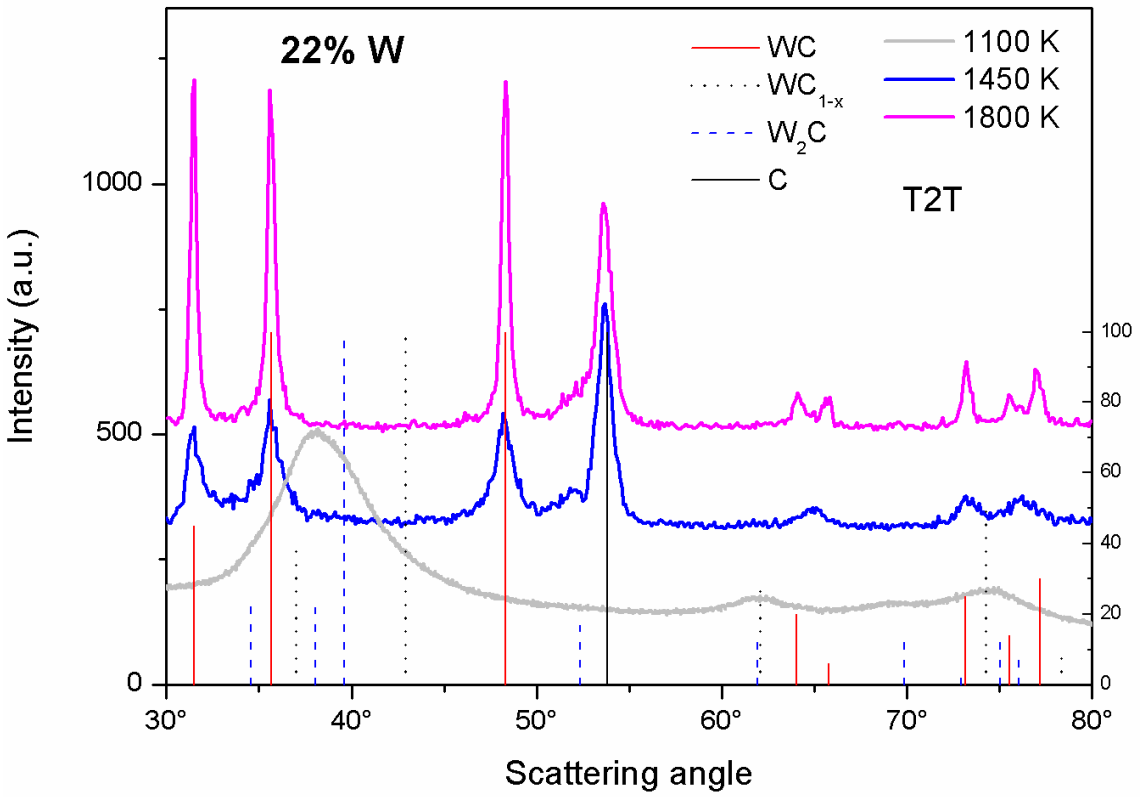

Figure 7.22. X-ray spectra of 22 at. % W doped films after annealing at different temperatures for one hour. Diffraction peaks for the carbide phases WC, W_2C, WC_{1-x} (PDF card 25-1047, 35-776, 20-1316) and for pure graphite (substrate) are indicated [99]

Annealing of the 22% tungsten sample at 1100 K leads formed very fine crystallites, which is consistent with data obtained by XRD. Carbide particles of a size below 5 nm are densely, and homogeneously distributed in the film, however, the XRD analysis did not enable positive phase identification of the carbide particles. The application of a nano-diffraction technique made it feasible to identify two tungsten carbide phases – cubic WC_{1-x} and hexagonal W_2C, as illustrated in the inserts in Figure 7.23b. The amount of each phase was approximately equal. Hexagonal monocarbide WC phase was not identified in this sample.

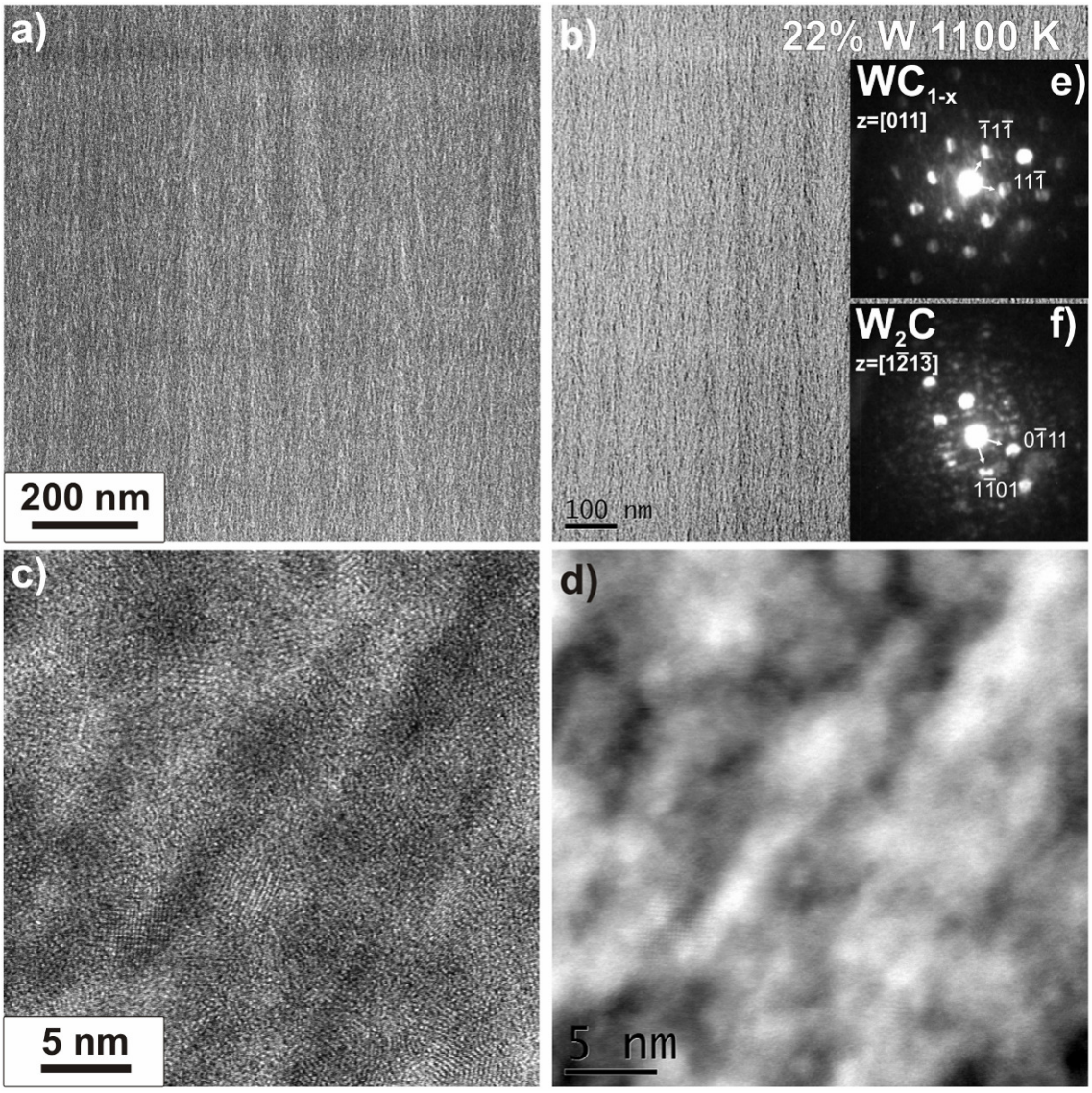

Figure 7.23. STEM images in BF mode (a, c) and in Z-contrast (b, d) together with typical electron diffractograms of WC_{1-x} (e) and W2C (f) of 22% W film annealed at 1100 K

An increase of the annealing temperature to 1450 K caused a noticeable increase in the size of the carbide particles as was anticipated from the results of the XRD. A significant change in the shape of carbides was detected. The carbide particles became elongated with a thickness of 10 nm and length of up to 100 nm and created a dense network, as shown in Figure 7.24c and d. When compared to samples with lower concentration of tungsten annealed at the same temperature a higher density and larger degree of carbide formation was observed. The nano-diffraction phase analysis of the carbide particles confirmed that only WC carbide was present. The absence of W_2C or WC_{1-x} phases in the sample was in good agreement with the results given by XRD.

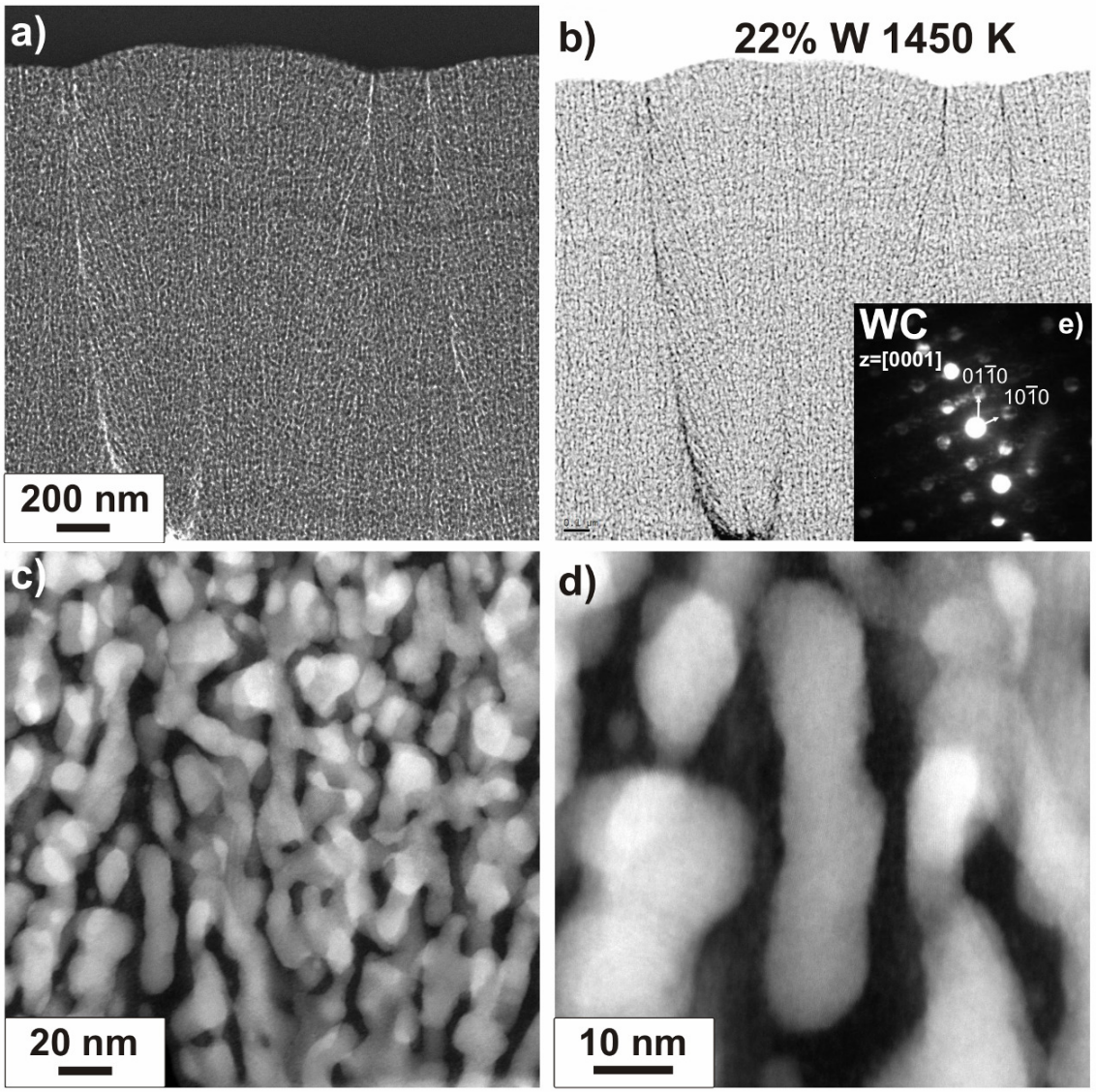

Figure 7.24. STEM images in BF mode (a, c) and in Z-contrast (b, d) together with typical electron diffractograms of WC (e) of 22% W film annealed at 1450 K

Multilayer system

In addition to the samples with a single, homogeneous tungsten concentration, one sample with a variable tungsten content was produced and annealed at 2200 K. The structure and arrangement of the carbide particles formed is illustrated in Figure 7.25a and b. Sublayers with various tungsten concentration are also indicated.

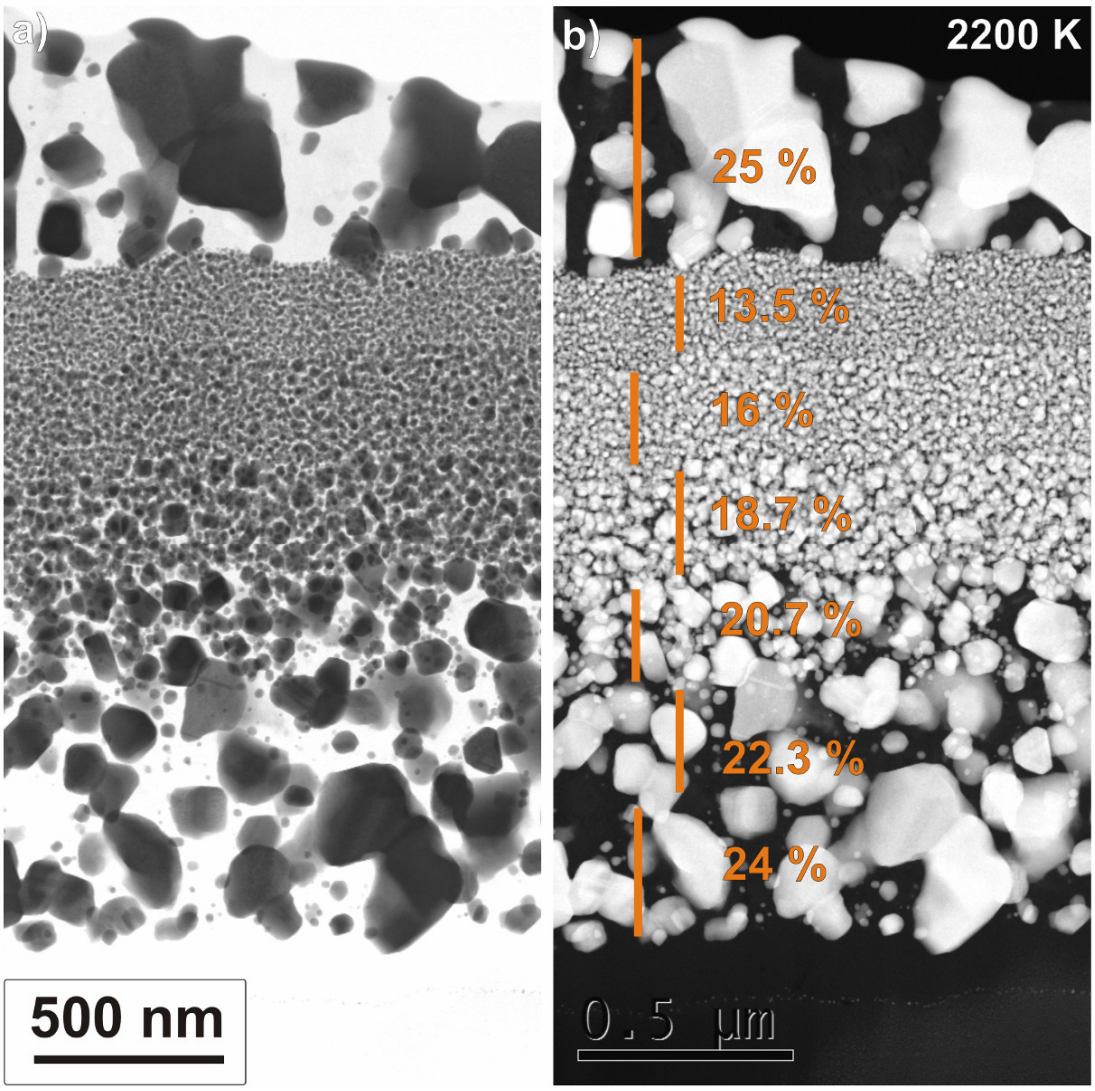

Figure 7.25. STEM images in BF mode (a) and in Z-contrast (b) of a multilayer sample annealed at 2200K. Different tungsten concentration in each sublayer is marked

Most of the sublayers after annealing can be quite easily distinguished due to specific carbide arrangement and size. Only the interface between the sublayers with 22.3% and 24% of tungsten was blurred because of the large, overlapping sublayer carbides. In the case of the multilayer sample only the local phase identification was performed by nano-diffraction.

The top sublayer contained the highest tungsten concentration of 25% W. The average size of carbide particles formed after annealing at 2200 K was 97 ± 70 nm. Phase identification by nano-diffraction confirmed the existence of only hexagonal WC in the sublayer. This was expected from the results of the sample doped with 22% tungsten and annealed at 1450 K and 1800 K.

The next three sublayers containing 13.5%, 16% and 18.7% of tungsten, respectively, were visibly distinct. As the tungsten concentration was increased, the average carbide size increased to 11 ± 4 nm (13.5% W), 13 ± 5 nm (16% W) and 15 ± 8 nm (18.7% W). The phase composition of the tungsten carbide particles also changed with the tungsten concentration. In the samples with 13.5% and 16% of tungsten, the principal carbide phase was W_2C identified in 14 out of 23 and 15 out of 24 particles, respectively. The other phases – WC_{1-x} and WC – were also present, however they were in the minority. The increase of the tungsten concentration to 18.7% resulted in changes of the phase composition. The predominant phase was WC carbide identified in 12 of 25 analyzed particles the remainder being lesser numbers of WC_{1-x} and W_2C particles.

A further increase in the tungsten concentration from 18.7% to 20.7% brought about a threefold increase in the average carbide size to 46 ± 27 nm. The particles consisted of W_2C and WC carbides in almost equal numbers. However, it was observed that the WC particles were larger than the W_2C relatively small particles meaning that the volume fraction of WC phase was larger than that of W_2C.

Two of the bottom sublayers (with 22.3% and 24% of tungsten) were analysed together as if a single layer since the carbide particles often overlapped in each of the initially deposited sublayers. Therefore, it was quite difficult to identify the exact interface between the sublayers. The average size of carbide particles in these two sublayers was 76 ± 45 nm with WC being the only phase present .

Discussion

The influence of tungsten concentration and annealing temperature on the composition of the carbide phases and the average crystallite sizes is summarized in Table 7.1 and Table 7.2. It is evident that, for a constant tungsten concentration, the size of the carbide particles increases with an increases in the annealing temperature, the tungsten atoms become more mobile which increases the degree of diffusion and therefore the formation of larger carbide particles.

Table 7.1 Amount of identified tungsten carbide phase together with average size of carbide particles

	WC_{1-x}	W_2C	WC	Average carbide size [nm]
9% W 1450K	17	6	-	< 5
9% W 2200 K	11	9	-	6 ± 2
9% W 2500 K	15	7	-	13 ± 5
9% W 2800 K	13	-	9	33 ± 22 350 ± 190 - (large WC exclusively)
14% W 2200 K (18% W 2200 K bottom)	12	14	2	12 ± 6
18% W 1450 K	7	18	3	9 ± 3
18% W 2200 K	4	4	16	22 ± 15
18% W 2800 K	-	-	17	568 ± 356
22% W 1100 K	10	12		< 5
22% W 1450 K	-	-	24	

Table 7.2 Amount of identified tungsten carbide phase together with average size of carbide particles

Multilayer	WC_{1-x}	W_2C	WC	Average carbide size [nm]
25% W 2200 K	-	-	18	97 ± 70
13.5% W 2200 K	6	14	3	11 ± 4
16% W 2200 K	4	15	5	13 ± 5
18.7% W 2200 K	5	8	12	15 ± 8
20.7 %W 2200 K	1	15	17	46 ± 27
22.3 – 24 % 2200 K	1	-	14	76 ± 45

It was determined, that the largest particles were identified as being the WC phase. It was also apparent that the size of the carbide particles increased with an increase in the dopant concentration at a constant annealing temperature.

The greater the concentration of tungsten, the larger and more densely arranged are the carbide particles. These phenomena were clearly observed in the multilayer sample, where the increase in carbide size is relatively slow for a tungsten concentration up to 18.7%. The size did not exceed 20 nm. At greater concentrations the crystallites grow much more rapidly. A change in tungsten concentration of only 2% resulted in a three fold increase in the size of the carbide particles. Additionally, the higher tungsten concentration enabled larger carbide particles to be formed during annealing at the same temperature.

It was also possible to determine the effect of tungsten concentration and annealing temperature on the phase composition of the particles formed in the heating process. In all cases, the first phases formed during the annealing were the two metastable carbides WC_{1-x} and W_2C. The thermodynamically stable monocarbide WC was very much the minority constituent, or did not exist at all at the lower annealing temperature. However, an increase in the annealing temperature brought about the transformation of the metastable carbides into thermodynamically stable WC phase. The transformation, however, did not occur under the same conditions. Firstly, the W_2C phase transforms into WC, with the transformation temperature being lower for a higher tungsten concentration. For the sample with a tungsten content of 9% the $W_2C \rightarrow WC$ transformation occurred between 2500 – 2800 K. The transformation temperature decreased to around 2200 K of an 18% W content and to below the 22% W content.

The transformation of WC_{1-x} carbide into WC takes place at a higher temperature than the $W_2C \rightarrow WC$ transformation, but it also was dependent on the tungsten concentration. In the literature [112], two types of transformations are identified:

- direct $WC_{1-x} \rightarrow WC$,
- indirect $WC_{1-x} \rightarrow W_2C \rightarrow WC$

The evidence of the research support the idea that direct transformation takes place, as an increase in the amount of W_2C phase was never observed with a corresponding decrease in the amount of the WC_{1-x} phase. For a sample with 9% of tungsten the $WC_{1-x} \rightarrow WC$ transformation must occur above 2800 K, and was not observed in the present study. For tungsten concentration of 18 and 22%, the transformation temperature decreased to above 2200 K and above 1100 K, respectively.

Summarizing this part of the findings, it may be concluded that the type and size of tungsten carbide particles is strongly dependent on both, the relative concentration of tungsten and the annealing temperature. Therefore, in a real divertor different structural changes in a re-deposited layer can be expected which will depend on the particular operating conditions, specifically the local tungsten concentration and the working temperatures. However, the presented research results could make an important contribution to the identification of local conditions, the temperature and tungsten concentration, which influence the formation of the re-deposited layers.

7.2.2 Re-deposited layer from ASDEX Upgrade divertor tile

An overview of the inner structure of the re-deposited layer grown on the ASDEX Upgrade divertor tile is illustrated in Figure 7.26. The layer was approximately 1 μm thick and consisted of two distinct sublayers, of roughly equally thickness. The lower layer, bright in the bright field (BF) mode, and darker in the Z-contrast mode consisted of low-Z elements, mainly carbon. The bottom part of the layer was deposited at the beginning of the operational campaign. The upper part consisted of both low-Z and high-Z elements, mainly carbon and tungsten and was formed later in the divertor's operational life.

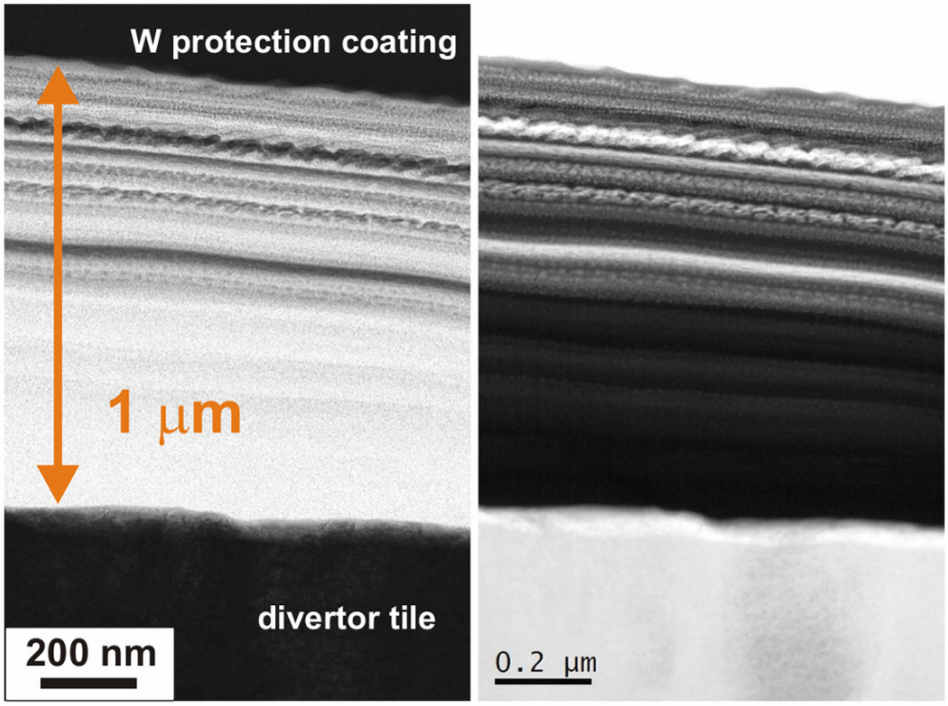

Figure 7.26. BF and Z-contrast STEM image of the re-deposited layer grown in ASDEX Upgrade during 2007 campaign

The tungsten rich area revealed a specific, stratified structure. The thickness of a particular sublayer varied in a range from below 10 to 50 nm. Each sublayer rich in tungsten has a different morphology: dotted, striped or chained, as illustrated in Figure 7.27. The very clear inhomogeneity of the stratified structure with distinct boundaries between the sublayers is evident.

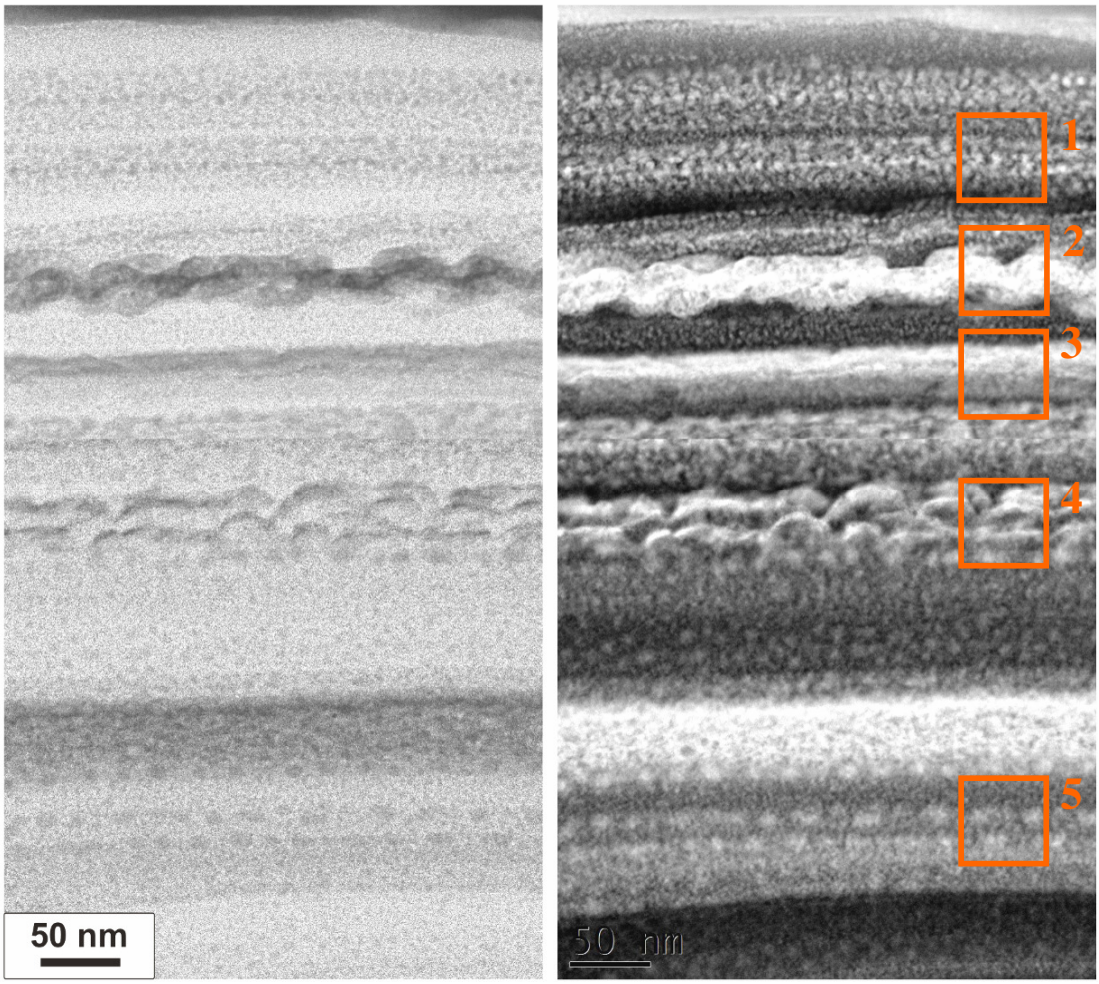

Figure 7.27. BF and Z-contrast STEM image of the upper (tungsten reach) part of the re-deposited layer; a specific, stratified structure is visible

On the upper part of the re-deposited layer five regions were selected for detailed investigation. In each of the selected regions, the structure of the formed carbides was significantly different suggesting that different conditions were involved in their creation. It is possible to identify regions with a higher local tungsten concentration – like region 2 and 5. The re-deposition of tungsten must have been greater during the operational period when they were formed. However, there are regions inside the re-deposited layer, where the amount of

tungsten was much lower, region 1 and 4. The amount of deposited tungsten can be estimated on the basis of the carbide phase composition of model samples described in Section 7.2.1.

Figure 7.28 and Figure 7.29 present high resolution images of each of the selected regions. It should be noted, that each region, consisted of densely arranged nanostructured crystallites. Carbides with a size below 5 nm are observed. The carbide arrangement was, however, different in each separate region. The most dense carbide arrangement is observed in region 2. Such a dense arrangement must correspond to the sublayer possessing the highest tungsten concentration.

Regions 3, 4 and 5 seem to have a similar carbide arrangement. Carbides in region 3 and 5 have formed a uniform sublayer, whereas in region 4 they are distributed in the form of stripes. The less dense arrangement of carbides in region 2, must correspond to a lower tungsten concentration. The lowest density of tungsten carbides was present in region 1, which should be related to the lowest tungsten concentration of the analysed areas. Based on the carbide arrangements, conclusions about the tungsten concentration may be drawn, however, for more precise evidence nano-diffraction phase analysis was undertaken.

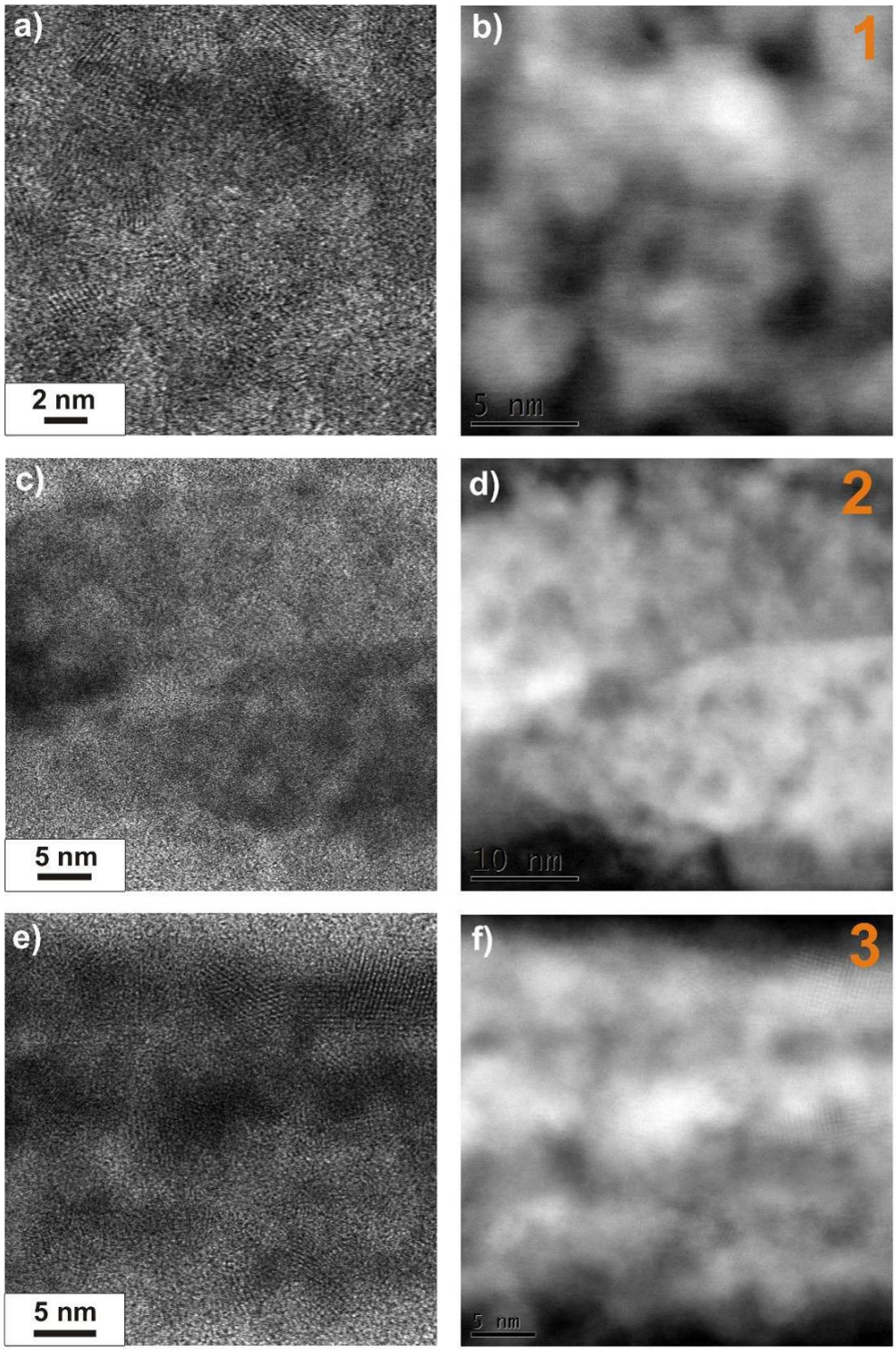

Figure 7.28 BF and Z-contrast STEM images of areas marked in Figure 7.27

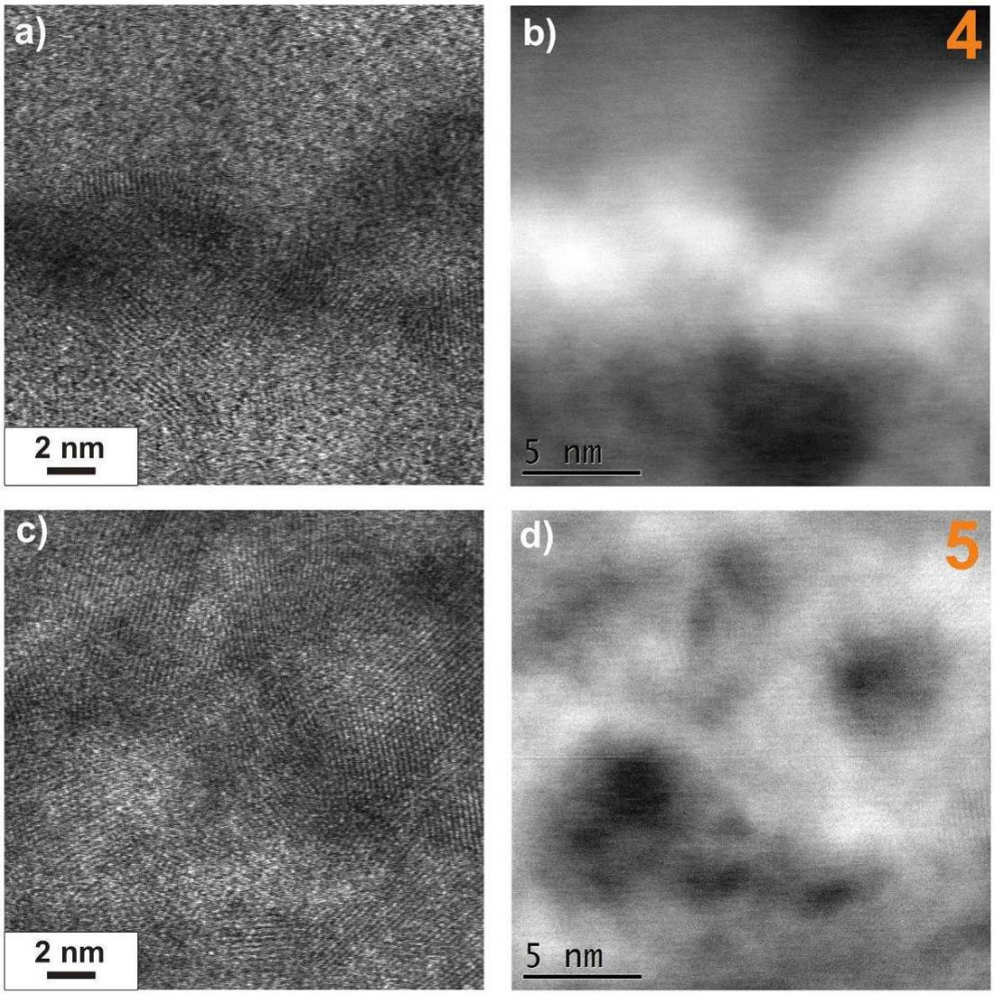

Figure 7.29 BF and Z-contrast STEM images of areas marked in Figure 7.27

The results of the nano-diffraction analysis are given in Table 7.3.

Table 7.3 Amount of identified tungsten carbide phase together with average size of carbide particles

Re-deposited layer from ASDEX Upgrade 2007	WC_{1-x}	W_2C	WC	Average carbide size [nm]
Region 1	13	2	-	< 5
Region 2	-	-	-	-
Region 3	6	14	-	< 5
Region 4	16	16	-	< 5
Region 5	10	6	-	< 5

The carbide particles were so densely arranged in region 2, that unequivocal carbide identification was not possible. In the other regions, both metastable carbides WC_{1-x} and W_2C were shown to be present. The WC phase was not found. Nevertheless, it was possible to establish that different proportions of the carbides present. The highest amount of WC_{1-x} was detected in region 1 (13 of the 15 analysed particles). In regions 4 and 5, the amount of WC_{1-x} and W_2C were comparable. The greatest amount of W_2C crystallites was found in region 3 (14 of the 20 analysed particles).

If comparisons are made with the model system, discussed in Section 7.2.1, it is possible to make estimates of the tungsten concentration and the working temperature. Region 1, with highest WC_{1-x} content, is similar to the model sample with 9% of tungsten annealed at 1450 K. However, as the carbide particles are more densely arranged, it is most likely that the tungsten concentration in region 1 is slightly higher and operational temperature somewhat lower.

Higher tungsten concentrations must have been present in regions 3, 4 and 5, where a greater number of W_2C carbide particles are present. When comparing high resolution images with the model system samples, the carbide arrangement in those regions is similar to the 22% tungsten sample annealed at 1100 K. The phase composition, however, fits only to regions 4 and 5. The phase composition in region 3 seems to fit the 18% tungsten sample, but annealed at a temperature below 1450 K, but most likely above 1100 K. Region 2 must have had the highest tungsten concentration, above 22%, but a phase analysis was not possible.

It can be concluded, that different sublayers tungsten concentrations which varied from above 9% to above 22% and most likely all were formed at in the temperature range 1150 – 1350 K.

Finally, it should be noted, that model system discussed in Section 7.2.1 was positively verified with regard to analysed re-deposited layer from ASDEX Upgrade. Moreover, the model system can be a very useful reference when considering different re-deposited layers formed under different conditions. The broad range of temperature was applied to enable the information to be utilized when considering the ITER reactor in which higher working temperatures are expected.

8 Conclusion

In the study, various aspects of the structural degradation of divertor components have been investigated. The experiments undertaken concerned structural changes, either due to carbon diffusion from carbon substrate to the tungsten coating, or the re-deposition of tungsten and carbon. The results have shown that divertor systems based on tungsten and carbon are not stable and undergo significant changes at the high operational temperatures required. In particular it has been found that:

1. The CFC/Mo/W divertor coating system transforms into a carbide containing system CFC/Mo_2C/WC/W_2C/W during operation at high temperatures. This transformation results in degradation of the thermo-mechanical properties of the coating.
2. The growth of the tungsten carbide layer is controlled by the diffusion of carbon from the substrate. The activation energy of the diffusion process was determined as 2.02 eV (195 kJ/mol) and 3.44 eV (322 kJ/mol) in the short and long term, respectively.
3. The operational temperature of the divertor with a CFC/Mo/W coating system installed at JET has been restricted to below 1470 K because of the rapid formation of carbide at higher temperatures.

4. The formation of nanometric tungsten carbides in the re-deposited layer after one campaign in ASDEX Upgrade has been confirmed. Tungsten carbides WC_{1-x} and W_2C with different relative proportions and sizes below 5 nm were identified.
5. Based on the investigation of the model tungsten doped carbon layers, the most likely tungsten concentration, from above 9% to above 22% and formation temperature in the range of 1150 – 1350 K of the re-deposited layer have been proposed.

The results obtained in the present study allowed the degradation mechanisms in carbon/tungsten divertor systems to be ascertained. Based on the kinetics of the growth rate of tungsten carbide the safe working period for a divertor with a Mo/W coating produced by the CMSII technique can be determined. Additionally, the model system of re-deposited layer has been proposed and positively verified with regard to re-deposited layer formed in ASDEX Upgrade divertor during the 2007 campaign.

9 References

[1] International Energy Agency (IEA); *World Energy Outlook* (2010)

[2] International Energy Agency (IEA); *Key World Energy Statistics* (2011)

[3] U. Samm, *TEXTOR: a pioneering device for new concepts in plasma–wall interaction, exhaust, and confinement*, Fusion Science and Technology 47 (2005) 73–75

[4] J. Pamela, J. Ongena, D. Borba, R. Buttery, G. Counsell, R. Felton, E. Joffrin, P. Lomas, A. Murari, J.-M. Noterdaeme, G. Piazza, V. Riccardo, R. Pitts, S. Rosanvallon, D. Stork, K.-D. Zastrow, Collaborators to the JET-EFDA workprogramme; *Overview of recent JET results in preparation for ITER operation: Interplay between technical and scientific progress*; Fusion Engineering and Design 74 (2005) 17–30

[5] R. Neu, V. Bobkov, R. Dux, A. Kallenbach, Th. Putterich, H. Greuner, O. Gruber, A. Herrmann, Ch. Hopf, K. Krieger, C.F. Maggi, H. Maier, M. Mayer, V. Rohde, K. Schmid, W. Suttrop, ASDEX Upgrade Team; *Final steps to an all tungsten divertor tokamak*; Journal of Nuclear Materials 363–365 (2007) 52–59

[6] T. Yamamoto , The JT-60 Team; *Technological development and progress of plasma performance on the JT-60U*; Fusion Engineering and Design 66-68 (2003) 39-48

[7] DIII-D Team, T.C. Simonen; *Results of DIII-D operation with new enabling Technologies*; Fusion Engineering and Design 39–40 (1998) 83–90

[8] J. Pamela; *Ten years of operation and developments on Tore Supra*; Fusion Engineering and Design 46 (1999) 313–322

[9] N. Holtkamp; *The status of the ITER design*; Fusion Engineering and Design 84 (2009) 98–105

[10] IPP Summer University for Plasma Physics (2007) – Conference Materials

[11] http://www.jet.efda.org/focus-on/limiters-and-divertors/

[12] J. Roth, E. Tsitrone, A. Loarze; *Plasma–wall interaction: Important ion induced surface processes and strategy of the EU Task Force*; Nuclear Instruments and Methods in Physics Research B 258 (2007) 253–263

[13] ITER Technical Basis, International Atomic Energy Agency (2002) Vienna

[14] C. H. Skinner, G. Federici; *Is carbon a realistic choice for ITER's divertor?*; Physica Scripta T124 (2006) 18–22

[15] P. Norajitra; *Divertor Development for a Future Fusion Power Plant (Volume 1)*; KIT Scientific Publishing (2011) 978-3-86644-738-7

[16] P. Starke, U. Fantz, M. Balden; *Investigations of chemical erosion of carbon materials in hydrogen and deuterium low pressure plasmas*; Journal of Nuclear Materials 337–339 (2005) 1005–1009

[17] G. Federici, J.N. Brooks, D.P. Coster, G. Janeschitz, A. Kukuskhin, A. Loarte, H.D. Pacher, J. Stober, C.H. Wu; *Assessment of erosion and tritiumcodeposition in ITER-FEAT;* Journal of Nuclear Materials 290–293 (2001) 260–265

[18] J. P. Bonal, C.H. Wu, *Neutron irradiation effects on the thermal conductivity and dimensional stability of carbon fiber composites at divertor conditions*, Journal of Nuclear Materials 228 (1996) 155-161

[19] R. A. Causey, T. J. Venhaus; *The use of tungsten in fusion reactors: a review of the hydrogen retention and migration properties*; Physica Scripta T94 (2001)

[20] V. Philipps; *Tungsten as material for plasma-facing components in fusion devices*; Journal of Nuclear Materials 415 (2011) 1-8

[21] S. Higashijima, S. Sakurai, S. Suzuki, K. Yokoyama, Y. Kashiwa, K. Masaki, Y.K. Shibama, M. Takechi, K. Shibanuma, A. Sakasai, M. Matsukawa, M. Kikuchi; *Mock-up test results of monoblock-type CFC divertor armor for JT-60SA*; Fusion Engineering and Design 84 (2009) 949–952

[22] Ph. Magaud, P. Monier-Garbet, J.M. Trave`re, A. Grosman; *Actively cooled plasma facing components in Tore Supra: From material and design to operation*; Journal of Nuclear Materials 362 (2007) 174–180

[23] J.H. You, Y.Y. Yang; *Behavior of stress singularities near the free edge of CFC/TZM bond interface under transient high heat flux loading*; Fusion Engineering and Design 38 (3) (1998) 331–342

[24] R.A. Pitts, S. Carpentier, F. Escourbiac, T. Hirai, V. Komarov, A.S. Kukushkin, S. Lisgo, A. Loarte, M. Merola, R. Mitteau, A.R. Raffray, M. Shimada, P.C. Stangeby; *Physics basis and design of the ITER plasma-facing components*; Journal of Nuclear Materials 415 (2011) S957–S964

[25] R. Neu, V. Bobkov, R. Dux, A. Kallenbach, Th. Pütterich, H. Greuner, O. Gruber, A. Herrmann, Ch. Hopf, K. Krieger, C.F. Maggi, H. Maier, M. Mayer, V. Rohde, K. Schmid, W. Suttrop, ASDEX Upgrade Team; *Final steps to an all tungsten divertor tokamak*; Journal of Nuclear Materials 363-365 (2007) 52-59

[26] R. Neu, Ch. Hopf, A. Kallenbach, T. Pütterich, R. Dux, H. Greuner, O. Gruber, A. Herrmann, K. Krieger, H. Maier, V. Rohde, ASDEX Upgrade Team; *Operational*

conditions in a W-clad tokamak; Journal of Nuclear Materials 367-370 Part B (2007) 1497-1502

[27] H. Maier, ASDEX Upgrade Team; *Tungsten erosion in the baffle and outboard regions of the ITER-like ASDEX Upgrade divertor*; Journal of Nuclear Materials 335 (2004) 515–519

[28] R. Neu, , R. Dux, A. Geier, O. Gruber, A. Kallenbach, K. Krieger, H. Maier, R. Pugno, V. Rohde, S. Schweizer, ASDEX Upgrade Team; *Tungsten as plasma-facing material in ASDEX Upgrade*; Fusion Engineering and Design 65 (3) (2003) 367–374

[29] R. Neu, V. Bobkov, R. Dux, J. C. Fuchs, O. Gruber, A. Herrmann, A. Kallenbach, H. Maier, M. Mayer, T. Pütterich, V. Rohde, A. C. C. Sips, J. Stober, K. Sugiyama and ASDE Upgrade Team; *Ten years of W programme in ASDEX Upgrade—challenges and conclusions*; Physica Scripta T138 (2009) 014038

[30] A Herrmann, H Greuner, J C Fuchs, P de Marné, R Neu and ASDEX Upgrade Team; *Experiences with tungsten coatings in high heat flux tests and under plasma load in ASDEX Upgrade*; Physica Scripta T138 (2009) 014059

[31] V. Philipps, Ph. Mertens, G. F. Matthews, H. Maier, JET-EFDA contributors; *Overview of the JET ITER-like Wall Project*; Fusion Engineering and Design 85 7-9 (2010) 1581-1586

[32] H. Maier, T. Hirai, M. Rubel, R. Neu, Ph. Mertens, H. Greuner, Ch. Hopf, G.F. Matthews, O. Neubauer, G. Piazza, E. Gauthier, J. Likonen, R. Mitteau, G. Maddaluno, B. Riccardi, V. Philipps, C. Ruset, C.P. Lungu, I. Uytdenhouwen and JET EFDA contributors; Tungsten and beryllium armour development for the JET ITER-like wall project; Nuclear Fusion 47 (3) (2007) doi:10.1088/0029-5515/47/3/009

[33] G. Piazza, G.F. Matthews, J. Pamela, H. Altmann, J.P. Coad, T. Hirai, A. Lioure, H. Maier, Ph. Mertens, V. Philipps, V. Riccardo, M. Rubel, E. Villedieu, Collaborators of the JET ITER-like Project; *R&D on tungsten plasma facing components for the JET ITER-like wall Project*; Journal of Nuclear Materials 367–370 (2007) 1438–1443

[34] H. Maier, R. Neu, H. Greuner, Ch. Hopf, G.F. Matthews, G. Piazza, T. Hirai, G. Counsell, X. Courtois, R. Mitteau, E. Gauthier, J. Likonen, G. Maddaluno, V. Philipps, B. Riccardi, C. Ruset, EFDA-JET Team; *Tungsten coatings for the JET ITER-like wall Project*; Journal of Nuclear Materials 363–365 (2007) 1246–1250

[35] C. Ruset, E. Grigore, H. Maier, R. Neu, H. Greuner, M. Mayer, G. Matthews; *Development of W coatings for fusion applications*; Fusion Engineering and Design 86 (2011) 1677–1680

[36] H. Maier, **M. Rasinski**, E. Grigore, C. Ruset, H. Greuner, B. Böswirth, G.F. Matthews, M. Balden, S. Lindig, JET-EFDA; *Performance of W coatings on CFC with respect to carbide formation*; Journal of Nuclear Materials 415 (2011) S310–S312

[37] H. Maier, **M. Rasinski**, E. Grigore, C. Ruset, H. Greuner, B. Böswirth, G.F. Matthews, M. Balden, S. Lindig, JET EFDA contributors; *Performance of W Coatings on CFC with Respect to Carbide Formation*, poster P3-82 19th Conference on Plasma Surface Interactions in Controlled Fusion Devices, 2010, San Diego

[38] I.-J. Shona, B.-R. Kim, J.-M. Doh, J.-K. Yoon, K.-D. Woo,; *Properties and rapid consolidation of ultra-hard tungsten carbide*; Journal of Alloys and Compounds 489 (2010) L4–L8

[39] A. A. Rempel, R. Würschum, H.-E. Schaefer; *Atomic defects in hexagonal tungsten carbide studied by positron annihilation*; Physical Review B (Condensed Matter and Materials Physics) 61 9 (2000) 5945-5948

[40] A. S. Kurlov, A. I. Gusev, Tungsten Carbies and W-C Phase Diagram; Inorganic Materials 42 (2) (2006) 121-127

[41] R. V. Sara; *Phase Equilibria in the System Tungsten—Carbon*; Journal of the American Ceramic Society 48 5 (1965) 251–257

[42] A. S. Kurlov, A. I. Gusev; *Neutron and x-ray diffraction study and symmetry analysis of phase transformation in lower tungsten carbide W_2C*; Physical Review B 76 (2007) 174115

[43] A. S. Kurlov, A. I. Gusev; *Phase equilibria in the W-C system and tungsten carbides*; Russian Chemical Reviews 75 (7) (2006) 617-636

[44] D. V. Suetin, I. R. Shein, A. L. Ivanovskii; *Tungsten carbides and nitrides and ternary systems based on them: the electronic structure, chemical bonding and properties*; Russian Chemical Reviews 79 7 (2010) 611- 634

[45] M. D. Demetriou, N. M. Ghoniem, A. S. Lavine; *Computation of Metastable Phases in Tungsten-Carbon System*; Journal of Phase Equilibria 23 4 (2002) 305- 309

[46] Y. Suda, T. Nakazono, K. Ebihara, K. Baba, R. Hatada; *Properties of WC films synthesized by pulsed YAG laser deposition*; Materials Chemistry and Physics 54 (1998) 177-180

[47] S. Sharafat, A. Kobayashi, S. Chen, N. M. Ghoniem; *Production of high-density Ni-bonded tungsten carbide coatings using an axially fed DC-plasmatron*; Surface and Coatings Technology 130 (2000) 164-172

[48] M. D. Demetriou, N. M. Ghoniem, A. S. Lavine; *Kinetic modelling of phase selection during non-equilibrium solicitation of a tungsten-carbon system*; Acta Materialia 50 (2002) 1421-1432

[49] J. Luthin, Ch. Linsmeier; *Carbon films and carbide formation on tungsten*; Surface Science 454-456 (2000) 78-82

[50] D. Hildebrandt, P. Wienhold, W. Schneider; *Mixed-material coating formation on tungsten surfaces during plasma exposure in TEXTOR-94*; Journal of Nuclear Materials 290-293 (2001) 89-93

[51] J. J. Yeh, R. L. Pfeffer, M. W. Cole, M. Ohring, J. E. Yehoda, *Reaction between tungsten and molybdenum thin films and polycrystalline diamond substrate*, Diamond and Related Materials 5 (1996) 1195-1203

[52] W. P. Leroy, C. Detavernier, R. L. Van Meirhaeghe, C. Lavoie; *Thin film solid-state reactions forming carbides as contact materials for carbon-containing semiconductors*; Journal of Applied Physic 101 (2007) 053714

[53] K. M. Reddy, T. N. Rao, J. Jordan; *Stability of nanostructured W-C phase during carburization of WO_3*; Materials Chemistry and Physics 128 (2011) 121-126

[54] S. L. Kharatyan, H. A. Chatilyan, L. H. Arakelyan, *Kinetics of tungsten carbidization under non-isothermal conditions*; Materials Research Bulletin 43 (2008) 897-906

[55] M. Balden, B. T. Cieciwa, I. Quntana, E. de Juan Pardo, F. Koch, M. Sikora, B. Dubiel; *Metal-doped carbon films obtained by magnetron sputtering*; Surface and Coatings Technology 200 (2005) 413-417

[56] M. A. Abad, M. A. Munoz-Marquez, S. El Mrabet, A. Justro, J. C. Sanchez-Lopez; *Tailored synthesis of nanostructured WC/a-C coatings by dual magnetron sputtering*; Surface and Coatings Technology 204 (2010) 3490-3500

[57] N. Radic, B. Grzeta, O. Milat, J. Ivkov, M. Stubicar; *Tungsten-carbon films prepared by reactive sputtering from argon-benzene discharges*; Thin Solid Films 320 (1998) 192-197

[58] C. Rebholz , J. M. Schneider, A. Leyland, A. Matthews; *Wear behaviour of carbon-containing tungsten coatings prepared by reactive magnetron sputtering*; Surface and Coatings Technology 112 (1999) 85–90

[59] Y. Pauleau, Ph. Gouy-Pailler, S. Païdassi; *Structure and mechanical properties of hard W—C coatings deposited by reactive magnetron sputtering*; Surface and Coatings Technology 54–55 1 (1992) 324-328

[60] S. El Mrabet, M. D. Abad, C. Lopez-Cartes, D. Martinez-Martinez, J. C. Sanchez-Lopez; *Thermal evolution of WC/C nanostrustured coatins by raman and in situ XRD analysis*; Plasma Processes and Polymers 6 (2009) 444-449

[61] A.-Y. Wang, K.-R. Lee, J.-P. Ahn, J. H. Han; *Structure and mechanical properties of W incorporated diamond-like carbon films prepared by a hybrid ion beam deposition technique*, Carbon 44 (2006) 1826-1832

[62] A. Czyzniewski, *Deposition and some properties of nanocrystalline WC and nanocomposite WC/a-C:H coatings*; Thin Solid Films 433 (2003) 180-185

[63] K. Abdelauahdi, C. Sant, F. Miserque, P. Aubert, Y. Zheng, C. Legrand-Buscema, J. Perriere, *Influence of CH4 partial pressure on the microstructure of sputtered-deposited tungsten carbide thin films*; Journal of Physics: Condense Matter 18 (2006) 1913-1925

[64] C. Adelhelm, M. Balden, **M. Rasinski**, S. Lindig, T. Plocinski, E. Welter, M. Sikora; *Investigation of metal distribution and carbide crystallite formation in metal-doped carbon films (a-C:Me, Me = Ti, V, Zr, W) with low metal content*; Surface & Coatings Technology 205 (2011) 4335–4342

[65] G. F. Matthews; *Material migration in divertor tokamaks*; Journal of Nuclear Materials 337-339 (2005) 1-9

[66] http://www-fusion-magnetique.cea.fr/

[67] J. Roth; *Chemical erosion of carbon based materials in fusion devices*; Journal of Nuclear Materials 266-269 (1999) 51-57

[68] E. Vietzke, K. Flaskamp, V. Philipps, G. Esser, P. Wienhold, J. Winter; *Chemical erosion of amorphous hydrogenated carbon films by atomic and energetic hydrogen*; Journal of Nuclear Materials 145-147 (1987) 443

[69] J.W. Davis, A.A. Haasz; *Impurity release from low-Z materials under light particle bombardment*; Journal of Nuclear Materials 241-243 (1997) 37-51

[70] A. Loarte, G. Saibena, R. Sartory, V. Riccardo, P. Andrew; *Transient heat loads in current fusion experiments, extrapolation to ITER and consequences for its operation*; Physica Scripta T128 (2007), pp. 222–228

[71] J. Roth, E. Tsitrone, A. Loarte, Th. Loarer, G. Counsell, R. Neu, V. Philipps, S. Brezinsek, M. Lehnen, P. Coad, Ch. Grisolia, K. Schmid, K. Krieger, A. Kallenbach, B. Lipschultz, R. Doerner, R. Causey, V. Alimov, W. Shu, O. Ogorodnikova, A. Kirschner, G. Federici, A. Kukushkin, EFDA PWI Task Force, ITER PWI Team, Fusion for Energy, ITPA SOL/DIV; *Recent analysis of key plasma wall interactions issues for ITER*; Journal of Nuclear Materials 390–391 (2009) 1–9

[72] I.E. Garkusha, V.A. Makhlaj, V.V. Chebotarev, I. Landman, V.I. Tereshin, N.N. Aksenov, A.N. Bandura; *Experimental study of plasma energy transfer and material erosion under ELM-like heat loads*; Journal of Nuclear Materials 390–391 (2009) 814–817

[73] D.G. Whyte, T.C. Jernigan, D.A. Humphreys, A.W. Hyatt, C.J. Lasnier, P.B. Parks, T.E. Evans, P.L. Taylor, A.G. Kellman, D.S. Gray, E.M. Hollmann; *Disruption mitigation with high-pressure noble gas injection*; Journal of Nuclear Materials 313–316 (2003) 1239–1246

[74] M. Mayer, M. Andrzejczuk, R. Dux, E. Fortuna-Zaleśna, A. Hakola, S. Koivuranta, K. Krieger, K.J. Kurzydłowski, J. Likonen, G. Matern, R. Neu, G. Ramos, **M. Rasinski**, V. Rohde, K. Sugiyama, A. Wiltner, W. Zieliński and ASDEX-Upgrade team; *Tungsten erosion and redeposition in the all-tungsten divertor of ASDEX Upgrade*; Physica Scripta T138 (2009) 014039

[75] M. Mayer, V. Rohde, J. Likonen, E. Vainonen-Ahlgren, K. Krieger, X. Gong, J. Chen, ASDEX Upgrade Team; *Carbon erosion and deposition on the ASDEX Upgrade divertor tiles*; Journal of Nuclear Materials 337–339 (2005) 119–123

[76] J.P. Coad, P. Andrew, S.K. Erents, D.E. Hole, J. Likonen, M. Mayer, R. Pitts, M. Rubel, J.D. Strachan, E. Vainonen-Ahlgren, A. Widdowson, JET-EFDA Contributors; *Erosion and deposition in the JET MkII-SRP divertor*; Journal of Nuclear Materials 363–365 (2007) 287–293

[77] J. Likonen, J.P. Coad, E. Vainonen-Ahlgren, T. Renvall, D.E. Hole, M. Rubel, A. Widdowson, JET-EFDA Contributors; *Structural studies of deposited layers on JET MkII-SRP inner divertor tiles*; Journal of Nuclear Materials 363–365 (2007) 190–195

[78] Y. Gotoh, T. Tanabe, Y. Ishimoto, K. Masaki, T. Arai, H. Kubo, K. Tsuzuki, N. Miya; *Long-term erosion and re-deposition of carbon in the divertor region of JT-60U*; Journal of Nuclear Materials 357 (2006) 138–146

[79] M. Mayer, V. Rohde, G. Ramos, E. Vainonen-Ahlgren, J. Likonen, J. L. Chen, ASDEX Upgrade team; *Erosion of tungsten and carbon markers in the outer divertor of ASDEX-Upgrade*; Physica Scripta T128 (2007) 106–110

[80] Y. Ueda, M. Fukumoto, M. Nishikawa, T. Tanabe, N. Miya, T. Arai, K. Masaki, Y. Ishimoto, K. Tsuzuki, N. Asakura; *Surface studies of tungsten erosion and deposition in JT-60U*; Journal of Nuclear Materials 363–365 (2007) 66–71

[81] M. Mayer, J. Likonen, J. P. Coad, H. Maier, M. Balden, S. Lindig, E. Vainonen-Ahlgren, V. Philipps, JET-EFDA Contributors; *Tungsten erosion in the outer divertor of JET*; Journal of Nuclear Materials 363-365 (2007) 101-106

[82] D. G. Whyte, J.P. Coad, P. Franzen, H. Maier; *Similarities in divertor erosion/redeposition and deuterium retention patterns between the tokamaks ASDEX Upgrade, DIII-D and JET*; Nuclear Fusion 39 (1999) 1025

[83] Y. Gotoh, J. Yagyu, K. Masaki, K. Kizu, A. Kaminaga, K. Kodama, T. Arai, T. Tanabe, N. Miya; *Analyses of erosion and re-deposition layers on graphite tiles used in the W-shaped divertor region of JT-60U*; Journal of Nuclear Materials 313–316 (2003) 370–376

[84] T. Tanabe, K. Masaki, K. Sugiyama, M. Yoshida; *An overview of recent erosion/deposition and hydrogen retention studies in JT-60U*; Physica Scripta T138 (2009) 014006

[85] M. Psoda, M. Rubel, G. Sergienko, P. Sundelin, A. Pospieszczyk; *Material mixing on plasma-facing components: Compound formation*; Journal of Nuclear Materials 386–388 (2009) 740–743

[86] M. Balden, C. Adelhelm, E. de Juan Pardo, J. Roth; *Chemical erosion by deuterium impact on carbon films doped with nanometer-sized carbide crystallites*; Journal of Nuclear Materials 363‑365 (2007) 1173‑1178

[87] M. Balden , E. de Juan Pardo, I. Quintana, B. Cieciwa, J. Roth; *Deuterium-induced chemical erosion of carbon-metal layers*; Journal of Nuclear Materials 337‑339 (2005) 980‑984

[88] P.A. Sauter, M. Baden; *Temperature dependence of the erosion behavior of deuterium beam expose tungsten-doped carbon films (a-C:W)*; Journal of Nuclear Materials 415 (2011) S117–S120

[89] V.Kh. Alimov, W.M. Shu, J. Roth, S. Lindig, M. Balden, K. Isobe, T. Yamanishi; *Temperature dependence of surface topography and deuterium retention in tungsten exposed to low-energy, high-flux D plasma*; Journal of Nuclear Materials 417 (2011) 572–575

[90] N. Yoshida, H. Iwakiri, K. Tokunaga, T. Baba; *Impact of low energy helium irradiation on plasma facing metals*; Journal of Nuclear Materials 337–339 (2005) 946–950

[91] K. Tokunaga, S. Tamura, N. Yoshida, K. Ezato, M. Taniguchi, K. Sato, S. Suzuki, M. Akiba; *Synergistic effects of high heat loading and helium irradiation of tungsten*; Journal of Nuclear Materials 329–333 (2004) 757–760

[92] H. Greuner, H. Maier, M. Balden, B. Boeswirth, Ch. Linsmeier; *Investigation of W components exposed to high thermal and high H/He fluxes*; Journal of Nuclear Materials 417 (2011) 495–498

[93] V. Kh. Alimov, W. M. Shu, J. Roth, S. Lindig, M. Balden, K. Isobe, T. Yamanishi; *Temperature dependence of surface topography and deuterium retention in tungsten exposed to low-energy, high-flux D plasma*; Journal of Nuclear Materials 417 (2011) 572–575

[94] M. Balden, S. Lindig, A. Manhard, J.-H. Sou; *D_2 gas-filled blisters on deuterium-bombarded tungsten*; Journal of Nuclear Materials 414 (2011) 69–72

[95] Y. Ueda, M. Fukumoto, J. Yoshida, Y. Ohtsuka, R. Akiyoshi, H. Iwakiri, N. Yoshida; *Simultaneous irradiation effects of hydrogen and helium ions on tungsten*; Journal of Nuclear Materials 386–388 (2009) 725–728

[96] S. Kajita, N. Yoshida, R. Yoshihara, N. Ohno, M. Yamagiwa; *TEM observation of the growth process of helium nanobubbles on tungsten: Nanostructure formation mechanizm*; Journal of Nuclear Materials 418 (2011) 152–158

[97] V. Kh. Alimov, W. M. Shu, J. Roth, K. Sugiyama, S. Lindig, M. Balden, K. Isobe, T. Yamanishi; *Surface morphology and deuterium retention in tungsten exposed to low-energy, high flux pure and helium-seeded deuterium plasmas*; Physica Scripta T138 (2009) 014048

[98] H. Bolt, V. Barabash, W. Krauss, J. Linke, R. Neu, S. Suzuki, N. Yoshida, ASDEX Upgrade Team; *Materials for the plasma-facing components of fusion reactors*; Journal of Nuclear Materials 329–333 (2004) 66–73

[99] J. W. Davis, V. R. Barabash, A. Makhankov, L. Plochl, K. T. Slattery; *Assessment of tungsten for use in the ITER plasma facing components*; Journal of Nuclear Materials 258-263 (1998) 308-312

[100] V. Barabash, G. Federici, J. Linke, C. H. Wu; *Material/plasma surface interaction issues following neutron damage*; Journal of Nuclear Materials 313-316 (2003) 42-51

[101] V. Barabash, G. Federici, M. Rodig, L. L. Snead, C. H. Wu; *Neutron irradiation effects on plasma facing components*; Journal of Nuclear Materials 283-287 (2000) 138-146

[102] B. I. Khripunov, A. N. Brukhanov, O. K. Chugunov, V. M. Gureev, V. S. Koidan, S. N. Kornienko, B. V. Kuteev, S. T. Latushkin, A. M. Muksunov, V. B. Petrov, A. I. Ryazanov, E. V. Semenov, V. P. Smirnov, V. G. Stolyarova, V. N. Unezhev; *Evidence of radiation damage impact on material erosion in plasma environment*; Journal of Nuclear Materials 390–391 (2009) 921–924

[103] ITER Material assessment report (2001) G 74 MA 10 01-07-11W 0.2.

[104] I. Uytdenhouwen, M. Decre´ton, T. Hirai, J. Linke, G. Pintsuk, G. Van Oost; *Influence of recrystallization on thermal shock resistance of various tungsten grades*; Journal of Nuclear Materials 363–365 (2007) 1099–1103

[105] T. Hirai, G. Pintsuk, J. Linke, M. Batilliot; *Cracking failure study of ITER-reference tungsten grade under single pulse thermal shock loads at elevated temperatures*; Journal of Nuclear Materials 390–391 (2009) 751–754

[106] C. Ruset, E. Grigore, I. Munteanu, H. Maier, H. Greuner, C. Hopf, V. Phylipps, G. Matthews, JET-EFDA Contributors, *Industrial scale 10_mWcoating of CFC tiles for ITER-likeWall Project at JET*; Fusion Engineering and Design 84 (2009) 1662–1665

[107] Joint Committee for Powder Diffraction Studies – International Centre for Diffraction Data (JCPDS ICDD), Powder Diffraction File™, Release 2000

[108] M. Birkholz, *Thin Film Analysis by X-ray Scattering*, Wiley-VCH, Weinheim, 2006

[109] T.B. Massalski (Ed), Binary Phase Diagrams, TMS, 1992

[110] Y. L. Corcoran, A. H. King, N. de Lanerolle, B. Kim; *Grain boundary diffusion and growth of titanium silicide layers on silicon;* Journal of Electronic Materials 19 (1990) 1177-1183

[111] Y. Tanaka, M. Kajihara, Y. Watanabe; *Growth behavior of compound layers during reactive diffusion between solid Cu and liquid Al;* Materials Science and Engineering: A 445–446 (2007) 355-363

[112] M.-H. Lin; *Synthesis of nanophase tungsten carbide by electrical discharge machining*; Ceramics International 31 (2005) 1109–1115